INFORMATION TO USERS

This manuscript has been reproduced from the microfilm master. UMI films the text directly from the original or copy submitted. Thus, some thesis and dissertation copies are in typewriter face, while others may be from any type of computer printer.

The quality of this reproduction is dependent upon the quality of the copy submitted. Broken or indistinct print, colored or poor quality illustrations and photographs, print bleedthrough, substandard margins, and improper alignment can adversely affect reproduction.

In the unlikely event that the author did not send UMI a complete manuscript and there are missing pages, these will be noted. Also, if unauthorized copyright material had to be removed, a note will indicate the deletion.

Oversize materials (e.g., maps, drawings, charts) are reproduced by sectioning the original, beginning at the upper left-hand corner and continuing from left to right in equal sections with small overlaps. Each original is also photographed in one exposure and is included in reduced form at the back of the book.

Photographs included in the original manuscript have been reproduced xerographically in this copy. Higher quality 6" x 9" black and white photographic prints are available for any photographs or illustrations appearing in this copy for an additional charge. Contact UMI directly to order.

UMI

A Bell & Howell Information Company
300 North Zeeb Road, Ann Arbor MI 48106-1346 USA
313/761-4700 800/521-0600

Static conformal fields in stereotactic radiosurgery

by

Daniel Bourque
Medical Physics Unit
McGill University, Montreal
August, 1997

A thesis submitted to the Faculty of Graduate Studies and Research
in partial fulfillment of the requirements for the degree of
Master of Science in Medical Radiation Physics

Abstract

During the past ten years, radiosurgery has moved from an obscure radiation treatment modality practiced in only a few specialized centers in the world, to a mainstream radiotherapeutic technique practiced in most major radiotherapy centers. Currently, the main thrust of development in radiosurgery is aimed at conformal dose delivery to irregular intracranial targets. This thesis deals with theoretical and practical aspects of the use of static, non-coplanar, conformal fields in radiosurgery.

For a typical radiosurgical case involving an irregular target, a comparison was made between treatment plans using the dynamic technique with one and two isocenters and a treatment plan using 7 fixed, non-coplanar, irregularly shaped beams. The static conformal fields plan achieved a target-dose conformation similar to the 2-isocenter dynamic plan, treating 2 to 3 times less healthy tissue to intermediate and high doses than did the 1-isocenter dynamic plan, while delivering a much more uniform dose to the target volume.

A comparison was also made between treatment plans using a varying number of static conformal fields. While the degree of tissue sparing and target-dose homogeneity were both shown to increase with the number of static fields, this increase was found to become smaller and smaller as the number of fields was successively raised from 5 to 7, from 7 to 9 and, ultimately, from 9 to 11. A conclusion is reached that a number of fields between 7 and 9 represents a reasonable compromise between the degree of tissue sparing and target-dose homogeneity achieved, and the ease with which the radiosurgical procedure is planned and delivered.

Résumé

Depuis l'introduction de la radiochirurgie à base d'accélérateurs linéaires il y a un peu plus de dix ans, la radiochirurgie est devenue un mode de traitement à radiation couramment utilisé, et est maintenant pratiquée dans la plupart des grands centres de radiothérapie. Les plus récents développements en radiochirurgie ont pour but d'améliorer la conformité entre la dose et le volume cible. Cette thèse traite des aspects théoriques et pratiques de l'utilisation de faisceaux de radiation statiques, non coplanaires, de formes irrégulières en radiochirurgie stéréotaxique.

Pour un cas typique impliquant une cible de forme irrégulière, une comparaison a été faite entre traitements radiochirurgiques utilisant la technique dynamique avec un et deux isocentres, et un traitement utilisant 7 faisceaux statiques, non coplanaires, de formes irrégulières. Le traitement à faisceaux statiques a atteint un degré de conformité dose-volume cible similaire à celui du traitement dynamique à deux isocentres, irradiant de 2 à 3 fois moins de tissue sain à hautes doses et à doses intermédiaires que le traitement dynamique à un isocentre, tout en améliorant, de façon significative, l'homogénéité de la dose à l'intérieur du volume-cible.

Une comparaison entre traitements radiochirurgiques utilisant un nombre différent de faisceaux de radiation statiques a également été faite. Bien que la conformité entre la dose et le volume cible augmente avec le nombre de faisceaux statiques, cette augmentation devient de plus en plus petite lorsque le nombre de faisceaux est porté successivement de 5 à 7, de 7 à 9 et, ultimement, de 9 à 11. Nous en venons à la conclusion qu'un nombre de faisceaux entre 7 et 9 représente un compromis raisonnable entre, d'une part, le degré de conformité dose-volume cible atteint et, d'autre part, l'aisance avec laquelle le traitement radiochirurgique pourra être planifié, préparé et livré.

Acknowledgements

I would like to thank, first and foremost, my supervisor, Dr. Ervin B. Podgorsak for his guidance and support throughout the duration of this research project. The freedom I was given to work independantly, as well as his readiness to offer assistance whenever it was needed, were very much appreciated.

I wish to thank Michel Morin and Socrates Aboulahef for the construction of the stereotactic head phantom and for the help they provided in constructing the custom radiosurgical collimator inserts.

I would like to extend my gratitude to the staff and students of the Medical Physics department at the Montreal General Hospital, who were very generous with their time and have always been eager to help. In particular, I am grateful to Dr. Conrado Pla for his help with the McGill Planning System and Dr. Gino B. Fallone for the use of his computing equipment. I would also like to thank fellow students François Deblois and Dimitri Hristov, for sharing their computer programming expertise, and Arthur Curtin-Savard for allowing me to ask so many questions (and, in most cases, for answering them).

I would also like to thank the Natural Sciences and Engineering Research Council of Canada (NSERC); their financial assistance during the course of this two year program was much appreciated.

Table of contents

Chapter 3

Experimental apparatus and techniques

Chapter 4

Treatment planning for small irregular fields

Chapter 5

Static conformal fields in radiosurgery

Chapter 6

Conclusions

Chapter 1

Introduction

1.1 Introduction

Stereotactic radiosurgery is a brain irradiation technique in which narrow beams of ionizing radiation are focused onto a small, stereotactically localized target. This technique is particularly useful in the treatment of deep-seated lesions in the brain, those that are inaccessible to conventional surgical techniques. Stereotactic radiosurgery is also performed on patients with poor general health, thus sparing them the trauma and complications involved with open surgery. Although radiosurgery is mostly used in the treatment of arterio-venous malformations (AVMs), certain intracranial tumors (acoustic neurinomas, pituitary adenomas, pineal tumours, craniopharyngiomas) and functional disorders (epilepsy, Parkinson's disease, intractable pain, trigeminal neuralgia) are also treated.

The aim of radiosurgery is to achieve a very high concentration of dose (typically a few thousand cGy) inside the target volume, while minimizing the dose to the surrounding healthy brain tissue. Thus, the requirements in terms of target localization and dose delivery to the target are very stringent. For accurate target localization, one needs a fixed external coordinate system

which can represent every point within the brain. This external frame of reference is provided by the stereotactic frame, which is rigidly attached to the patient's skull. The location of the target volume with respect to the stereotactic frame is accurately determined (±1 mm) using modern imaging techniques such as computed tomography (CT), magnetic resonance imaging (MRI) and digital subtraction angiography (DSA). The stereotactic frame is further used for accurate positioning of the patient on the treatment machine and for patient immobilization during the treatment. Thus, the stereotactic frame is essential not only for target localization, but also for patient setup on the treatment machine and subsequent dose delivery. The dose to the target volume must be delivered with an overall spatial accuracy of ±1 mm and a numerical accuracy of ±5 %.[1] Over the years, several radiosurgical techniques have been developed which meet these requirements. In all of these techniques, concentration of the dose inside the target volume is achieved by stereotactically focusing a number of narrow, well collimated beams of radiation (photons or heavy charged particles) onto the target.

1.2 History of radiosurgery

Stereotactic radiosurgery was introduced in 1951 by the Swedish neurosurgeon Lars Leksell who used a number of intersecting radiation beams to produce necrosis in small, well defined volumes within the brain.[2] Initially using X rays in the orthovoltage range (200 kV_p), Leksell soon understood the need to use higher energy radiation; because of their relatively low effective energy, the 200 kV_p X rays penetrated tissue poorly and therefore did not produce the desired dose concentration inside the target volume and the sharp dose falloff outside the target volume. Thus, Leksell proceeded to investigate the use of other sources of radiation for radiosurgery. In 1958, Larsson and Leksell[3] used 185 MeV protons from a cyclotron for the brain irradiation of certain animals. Proton beam radiosurgery was further developed and applied

clinically by Lawrence *et al.* [4] and Kjellberg *et al.* [5] More recently, the use of high energy helium ions has been reported,[6] and heavier ions such as neon and carbon are being investigated.[7] Due to their physical properties, heavy charged particle beams offer unique advantages for radiosurgery. These include their Bragg ionization peak, their finite range, and their relative lack of lateral scatter in tissue[8]. They also offer certain radiobiological advantages such as an increased relative biological effectiveness (RBE) and a smaller oxygen enhancement ratio (OER).[9] Because it relies on cyclotrons or synchrocyclotrons as a source of radiation, however, heavy charged particle beam radiosurgery is a very complex and costly technique. This is why it is presently used clinically in only a few centers worldwide.

Leksell abandoned the use of heavy charged particles for radiosurgery and proceeded to use cobalt-60 gamma rays. In 1968, he developed the first dedicated radiosurgery therapy unit[10] which used 179 ^{60}Co sources to produce 179 radiation beams that converged toward a common focal spot. This led to the development of the commercially available Gamma unit,[11] the description of which can easily be found in the literature.[12,13] The contemporary Gamma unit contains 201 ^{60}Co sources, each with a nominal activity of approximately 30 Ci, distributed evenly over a hemispherical sector of 160° x 60°. Each of the 201 beams are collimated so that they intersect at a common focal spot, which is located at a distance of 403 mm from the sources. While primary collimation is produced within the source core, final collimation is achieved with one of four interchangeable collimator helmets. These helmets contain 201 tungsten collimators with circular apertures that produce 4, 8, 14 or 18 mm diameter fields at the focus. Because the radiation sources and the patient remain stationary during the entire treatment, the Gamma unit has the advantage of delivering the dose with a very high spatial accuracy. The Gamma unit, however, suffers from several drawbacks, including a high cost, a short life span (^{60}Co has a half-life of only 5.26 years) and a dedicated use to radiosurgery

alone. Furthermore, its possibilities in terms of conformal radiosurgery are very limited.

Over the years, thousands of patients have been successfully treated with the Gamma unit, thus proving the clinical usefulness of radiosurgery. Nevertheless, radiosurgery did not immediately catch on as a widespread radiation treatment modality, mainly because of the high cost of the Gamma unit and the difficulties involved with accurate target localization. In 1974, Larsson *et al.* [14] considered the possibility of using isocentric linear accelerators (linacs) as radiation sources for radiosurgery. Isocentric linacs are already available in most cancer radiotherapy clinics and can be modified to perform radiosurgery relatively easily and with little expense. This, combined with the development of new and more accurate imaging modalities (CT, MRI, DSA), created a new and unprecedented interest in radiosurgery among the radiotherapy community. Since 1984, when the first clinical trials of linac-based radiosurgery were reported, the number of centers performing linac-based radiosurgery increased dramatically and quickly surpassed the number of centers with Gamma units.

1.3 Linac-based radiosurgery

When linac-based radiosurgery was first introduced in the mid 80s, there were concerns regarding the mechanical stability of isocentric linear accelerators. As opposed to treatments with the Gamma unit, which uses 201 stationary beams, linac-based radiosurgical techniques involve rotations of both the gantry and the treatment couch (or treatment chair). Ideally, the axes of rotation of the gantry, the collimator and the couch would intersect at a common fixed point, called the isocenter. In practice, however, these axes of rotation (for any arbitrary combination of angles) do not intersect at a common point, but rather within a sphere. For a linac to be used for radiosurgery, its isocenter must be located within a sphere of radius smaller than 1 mm. This isocenter

accuracy of ±1 mm, which is achievable in most modern linacs, is of the same order as the accuracy with which a target can be localized using modern imaging techniques.

In addition to having a high degree of mechanical stability, certain basic equipment requirements must be met before the linac can be used for radiosurgery. In order to define the small, circular beams that are used in radiosurgery, the linac must be equipped with an extra set of circular collimators. To ensure patient safety, the treatment couch should be supplied with special brakes to prevent any longitudinal or lateral movement during the treatment, along with interlocked readouts to continuously monitor its angular and height positions. Lastly, the stereotactic frame is immobilized during the treatment with special brackets that attach to the couch, or with a special floor stand.

Conventional linac-based radiosurgical techniques fall into three categories: multiple non-coplanar converging arcs, dynamic stereotactic radiosurgery, and conical rotation. All three of these techniques involve rotations of both the gantry and the treatment couch or treatment chair. In order to describe these techniques, one must choose a convention with regards to the gantry and couch angles. The convention that has been adopted for the present work is illustrated in FIGURE 1-1, with θ and ϕ representing the gantry the couch angles, respectively.

In the *multiple non-coplanar converging arcs* technique, the dose to the target is delivered through a series of non-coplanar arcs. A single arc is performed during the rotation of the linac gantry with the treatment chair or couch in a stationary position (i.e., at a fixed angular position). In order to avoid parallel opposed beams, which degrade the dose fall-off within the plane of gantry rotation, arc angles of less than 180° are generally used. The multiple

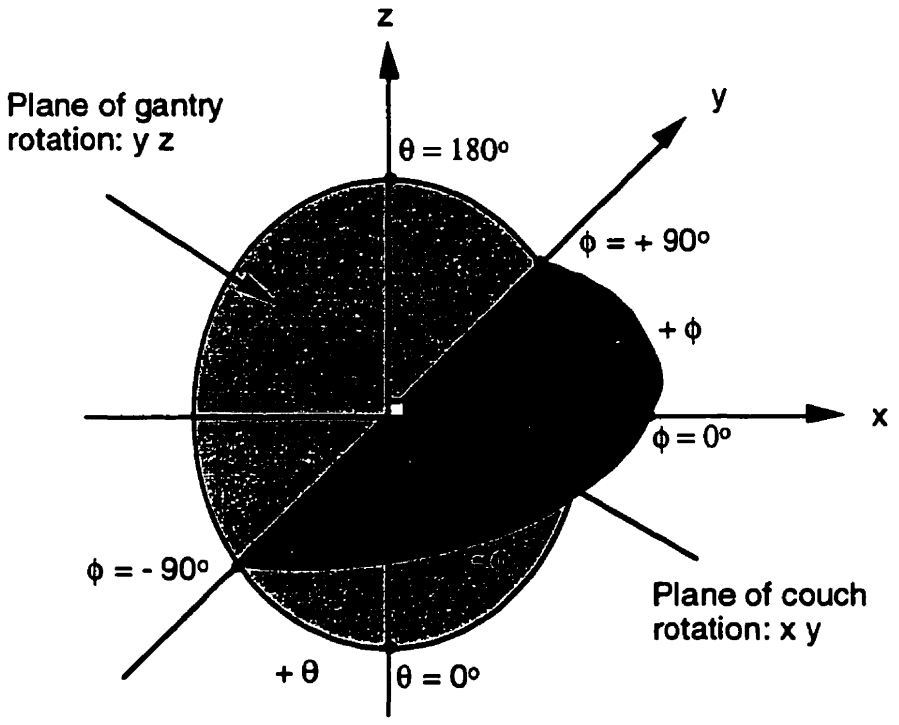

FIGURE 1-1 *Definition of the gantry (θ) and couch (ϕ) angles during linac-based radiosurgical procedures. In dynamic stereotactic radiosurgery, the gantry rotates in the yz plane from θ = 30° to θ = 330°, while simultaneously the couch rotates in the xy plane from ϕ = 75° to ϕ = -75°.*

arcs technique was first used in 1984 by Betti and Derechinsky,[15] who used several 140° arcs to treat patients sitting in a specially designed treatment chair. This technique was further developed and used clinically by Colombo *et al.* [16] in Vicenza and Hartmann *et al.* [17] in Heidelberg. The Heidelberg group used eleven 140° arcs to treat patients in a supine position on the treatment couch. Because of the high number of arcs evenly spaced over the entire upper hemisphere of the patient's head, the Heidelberg technique achieved excellent dose fall-offs outside the target volume. In 1988, Lutz *et al.* [18] in Boston have demonstrated that a reasonable dose fall-off outside the target volume could be achieved with as few as 4 arcs.

The *dynamic radiosurgery* technique was developed by Podgorsak et al. at McGill University in Montreal in 1987.[19,20] The main feature of this technique

is the simultaneous rotation of both the gantry and the treatment couch during the radiosurgical treatment. The gantry rotates through 300°, from $\theta = 30°$ to $\theta = 330°$, while the couch rotates through 150°, from $\phi = 75°$ to $\phi = -75°$. As a result, parallel-opposed beams are continuously avoided, even though the gantry rotates almost a full circle. The resulting beam entry trace on the patient's head, which totally lies in the upper hemisphere, is similar to the seam pattern found on a baseball.

In 1990, McGinley *et al.* [21] introduced the *conical rotation* technique, in which the gantry remains stationary at different angular positions while the patient rotates (through 360°) on a special treatment chair. The resulting beam entry pattern on the patient's head is made of conical circles, the number of which corresponds to the number of different gantry angular positions. For a typical treatment, three different gantry angles are used: θ=100°, θ=120° and θ=145°.

1.4 Conformal radiosurgical techniques

Irradiation of a single isocenter using conventional radiosurgical techniques results in spherical isodose surfaces. Thus, exact target-dose conformation is only obtained in the idealized situation of a spherical target. Clinical targets, however, are generally not spherical; most of them are irregularly shaped to some degree. Therefore, irradiating a target to a single isocenter with conventional radiosurgical techniques may cause a significant amount of healthy tissue to be exposed to high radiation doses. Hence, the importance of conforming the shape of the isodose surfaces to the shape of the target.

By far the most common technique for shaping radiosurgical dose distributions is by irradiating the target with several isocenters.[22,23] This multiple

isocenter technique combines several single radiosurgical treatments, each having a different center of convergence of the radiation beams (different isocenter). Even though good target-dose conformation can be achieved with this technique, multiple isocenter treatments typically result in overdosed volumes within the target, because of the overlap in the spherical dose distributions from each isocenter. This results in large dose inhomogeneities within the target volume, where the maximum dose can easily be up to twice as high as the prescription dose (i.e., up to 100% or more in target-dose inhomogeneities). While the exact effects of dose inhomogeneities are still unclear, they have been associated with radiosurgical complications.[24]

Several groups using the multiple arcs technique have developed methods of producing dose distributions for elongated targets using a single isocenter, by varying one or more of the following: number of arcs, arc planes, arc length, arc weights, and field apertures.[25,26] Similarly, attempts have been made to produce ellipsoidal isodose surfaces with the Gamma unit by selectively blocking a number of the 201 beams.[27] While the lower isodose surfaces were found to be elliptical, these isodose shaping techniques have had very little effect on the higher isodose surfaces. Furthermore, because of the large number of variables involved (number of arcs, arc planes, arc lengths, arc weights, field apertures, ...), these methods result in more lengthy and complicated treatment planning and treatment delivery procedures.

Ideal conformal radiosurgical techniques would allow for the shaping of the higher level isodose surfaces in order to deliver as uniform a dose as possible to the target volume, while concurrently minimizing the amount of healthy tissue irradiated to high doses. This can be accomplished using conformational field shaping techniques, in which the shape of the radiation beam is no longer circular, but rather conforms (to some degree) to the cross-sectional shape of the target. Dynamic field shaping, in which the shape of the radiation beam continuously changes during the treatment, would be expected

to give the best results. In 1991, Leavitt *et al.* [28] described a special collimation system which is capable of defining, for each arc increment, a polygonal field whose shape conforms to the projection of the target. Dynamic field shaping using micro-multileaf collimators has also been reported.[29] While the dosimetric advantages of dynamic field shaping are quite evident, it remains a technically demanding approach and presents almost insurmountable challenges regarding the verification of the treatment procedure. Other groups have considered using a single irregularly shaped field for an entire treatment arc, without modifying the shape of the field during the arc.[30,31,32] The use of elliptical fields[33] and variable-length rectangular fields[34] to produce, respectively, ellipsoidal and cylindrical dose distributions has also been reported. Although they have not all been implemented clinically, these techniques have shown that conformation of the high level isodose surfaces (such as the 80% or 90% surfaces) is possible by using fields whose shapes conform more closely to the projections of the target.

1.5 Radiosurgery with static conformal fields

A simpler alternative to dynamic field shaping is to irradiate the irregularly shaped target with a number of static, non-coplanar, conformal beams. In 1993, Bourland and McCollough[35] compared a single isocenter four arc plan with several static conformal fields plans by performing computer simulations using spherical and hemispherical targets in an idealized spherical phantom. They showed that for the non-spherical target (hemispherical target), the static conformal fields techniques significantly reduced the volume of healthy tissue irradiated to high doses.

Also in 1993, Laing *et al.* [36] introduced different theoretical ellipsoidal targets into the head CT images of a previously treated patient and compared treatment plans using four 120° arcs with plans using 3, 4 and 6 static conformally blocked fields. The static conformal beams were shown to treat a

lesser amount of healthy tissue at intermediate and high doses than the arc technique. Furthermore, this tissue sparing effect was found to increase with the size and the degree of irregularity of the target.

Marks *et al.* [37] have reported using a number of fixed coplanar or non-coplanar conformal fields (between 4 and 8) to treat certain intracranial lesions. In order to obtain highly uniform dose distributions, wedge filters (chosen by vector analysis of dose gradients) were added to the fields. For both an idealized spherical target and an irregular target, comparisons were made between the healthy tissue dose volume histograms obtained using different static field irradiation geometries. Moreover, it was shown that similar dose fall-offs at the edge of the target volume can be achieved using fixed shaped beams and using non-coplanar arcs whose weights are adjusted to take into account the irregular shape of the target.

Finally, Hamilton *et al.* [38] compared treatment plans using 4, 8 and 12 fixed, non-coplanar, conformal fields with a plan using four 140° arcs, for a previously treated radiosurgical case involving an irregular target. It was shown that the amount of healthy tissue irradiated to high and intermediate doses was significantly reduced for the 8 and 12 field plans, compared to the four arc plan. Furthermore, as the number of static conformal fields increased, the dose inside the target volume was found to become more and more uniform.

1.6 Thesis organization

The goal of this thesis is to evaluate the dosimetric advantages of using static conformal fields for radiosurgery of irregular targets by comparing treatment plans using static conformal fields with plans using the dynamic radiosurgery technique. The organization of this thesis is presented in the remainder of this section.

Chapter 2 presents the fundamental concepts inherent to radiation dosimetry. Basic radiotherapy quantities such as absorbed dose, exposure and kerma are defined. Also defined are the basic dosimetric functions (*PDD, OAR, TMR,* ...) used in calculating dose distributions. Also included is a description of the various processes through which photons and electrons interact with matter in order to produce absorbed dose.

Chapter 3 gives a description of the experimental apparatus and techniques that were used for this thesis. A brief overview of medical linear accelerators is first given, with an emphasis on the type of linear accelerator that is used for radiosurgery here at McGill University. A description of the various dosimetry techniques that were used to measure the dose, along with the different phantoms in which this dose was measured is also given. Finally, the methods used for the fabrication of the custom-made radiosurgical collimators are presented.

Chapter 4 deals with the treatment planning systems that were used for this thesis. In addition to a brief description of the McGill radiosurgical planning system, a thorough discussion of the *CADPLAN* 3-D External Beam Treatment Planning System is given, along with the modifications that were required in order for it to accurately calculate the dose distributions produced by small irregular fields.

Chapter 5 presents the results of the comparison between the dynamic technique and the static conformal fields technique for radiosurgery of a typical, irregular, intracranial target. In order to evaluate the effect of varying the number of fields, a comparison between treatment plans using a different number of fixed, non-coplanar, irregularly shaped fields is also presented.

Chapter 6 summarizes the overall results and gives recommendations for possible future work related to this thesis.

1.7 References

[1] American Association of Physicists in Medicine, **Stereotactic Radiosurgery**, AAPM report no. 54, 1995.

[2] L. Leksell, **The stereotaxis method and radiosurgery of the brain**, Acta Chir. Scan. **102**: 316-319 (1951).

[3] B. Larsson, L. Leksell, B. Rexed, P. Sourander, W. Mair and B. Anderson, **The high energy proton beam as a neurosurgical tool**, Nature **182**:1222-1223 (1958).

[4] J.H. Lawrence, C.A. Tobias, J.L. Born, C. Wang and J.A. Linfoot, **Heavy-particle irradiation in neoplastic and neurologic disease**, J. Neurosurg. **19**: 717-722 (1962).

[5] R.N. Kjellberg, A. Sintani, A.G. Frantz and B. Kliman, **Proton beam therapy in acromegaly**, N. Engl. J. Med. **278**: 689-695 (1968).

[6] J.I. Fabrikant, J.T. Lyman and Y. Hosobuchi, **Stereotactic heavy-ion Bragg peak radiosurgery for intra-cranial vascular disorders: method for treatment of deep arteriovenous malformations**, Brit. J. Radiol. **57**: 479-490 (1984).

[7] J.T. Lyman and J. Howard, **Dosimetry and instrumentation for helium and heavy ions**, Int. J. Radiat. Oncol. Biol. Phys. **3**: 81-86 (1977).

[8] K.A. Frankel, R.P. Levy, J.I. Fabrikant and M.H. Philips, **Heavy-charged particle radiosurgery: rationale and method**, Stereotactic Radiosurgery, McGraw-Hill, 1993.

[9] Hall E.J., **Radiobiology for the radiologist**, 3rd Ed., J.B. Lippincott Company, Philadelphia, 1988.

[10] L. Leksell, **Cerebral radiosurgery I Gamma thalamotomy in two cases of intractable pain**, Acta Chir. Scan. **134**: 385-395 (1968).

[11] Leksell Gamma unit, Elekta Instrument AB, Stockholm, Sweden.

[12] L. Walton, C.K. Bomford and D. Ramsden, **The Sheffield stereotactic radiosurgery unit: physical characteristics and principles of operation**, Brit. J. Radiol. **60**: 897-906 (1987).

[13] A. Wu, G. Lindner, A.H. Maitz, A.M. Kalend, L.D. Lunsford, J.C. Flickinger and W.D. Bloomer, **Physics of Gamma knife approach on convergent beams in stereotactic radiosurgery**, Int. J. Radiat. Oncol. Biol. Phys. **18**: 941-949 (1990).

[14] B. Larsson, K. Liden and B. Sarby, **Irradiation of small structures through the intact skull**, Acta Radiol. TPB **13**: 513-534 (1974).

[15] O.O. Betti and V.E. Derechinsky, **Hyperselective encephalic irradiation with linear accelerators**, Acta Neurochir. Suppl. **33**: 385-390 (1984).

[16] F. Colombo, A. Benedetti, F. Pozza, R.C. Avanzo, C. Marchetti. C. Chierego and A. Zanardo, **External stereotactic irradiation by linear accelerator**, Neurosurg. **16**: 154-160 (1985).

[17] G.H. Hartmann, W. Schlegel, V. Sturm, B. Kober, O. Pastyr and W.J. Lopez, **Cerebral radiation surgery using moving field irradiation at a linear accelerator facility**, Int. J. Radiat. Oncol. Biol. Phys. **11**: 1185-1192 (1985).

[18] W. Lutz, K.R. Winston and N. Maleki, **A system for stereotactic radiosurgery with a linear accelerator**, Int. J. Radiat. Oncol. Biol. Phys. **14**: 373-381 (1988).

[19] E.B. Podgorsak, A. Olivier, M. Pla, J. Hazel, A. de Lotbiniere and B. Pike, **Physical aspects of dynamic stereotactic radiosurgery**, Appl. Neurophysiol. **50**: 263-268 (1987).

[20] E.B. Podgorsak, A. Olivier, M. Pla, P.Y. Lefebvre and J. Hazel, **Dynamic stereotactic radiosurgery**, Int. J. Radiat. Oncol. Biol. Phys. **14**: 115-126 (1988).

[21] P.H. McGinley, E.K. Butker, I.R. Crocker and J.C. Landry, **A patient rotator for stereotactic radiosurgery, Phys.** Med. Biol. **35**: 649-657 (1990).

[22] J.C. Flickinger, L.D. Lunsford, A. Wu, A.H. Maitz, and A.M. Kalend, **Treatment planning for Gamma knife radiosurgery with multiple isocenters**, Int. J. Radiat. Oncol. Biol. Phys. **18**: 1495-1501 (1990).

[23] R. Ramani, P.F. O'Brien, P. Davey, M.L. Schwartz, C.S. Young, A.W. Lightstone and D.L.D. Mason, **Implementation of multiple isocentre treatment for dynamic radiosurgery**, Brit. J. Radiol. **68**: 731-735 (1995).

[24] L.A. Nedzi, H. Kooy, E. Alexander III, R.S. Gelman and J.S. Loeffler, **Variables associated with the development of complications from radiosurgery of intracranial tumors**, Int. J. Radiat. Oncol. Biol. Phys. **21**: 591-599 (1991).

[25] M.C. Plazas, D. Lefkopoulos and M. Schlienger, **The influence of arc weights on the dose distribution for single target radiosurgery**, Med. Phys. **20**: 1485-1490 (1993).

[26] G. Luxton and G.J. Jozsef, **Single isocenter treatment planning for homogeneous dose delivery to nonspherical targets in multiarc linear accelerator radiosurgery**, Int. J. Radiat. Oncol. Biol. Phys. **31**: 635-643 (1995).

[27] J.C. Flickinger, A.M. Maitz, A.Kalend, L.D. Lunsford and A. Wu, **Treatment volume shaping with selective beam blocking using the Leksell Gamma unit**, Int. J. Radiat. Oncol. Biol. Phys. **19**: 783-789 (1990).

[28] D.D. Leavitt, F.A. Gibbs, M.P. Heilbrun, J.H. Moeller and G.A. Takach Jr., **Dynamic field shaping to optimize stereotactic radiosurgery**, Int. J. Radiat. Oncol. Biol. Phys. **21**: 1247-1255 (1991).

[29] L.A. Nedzi, H.M. Kooy, E. Alexander, G.K. Svensson and J.S. Loeffler, **Dynamic field shaping for stereotactic radiosurgery: a modeling study**, Int. J. Radiat. Oncol. Biol. Phys. **25**: 859-869 (1993).

[30] C. Serago, A. Lewin, P. Houdek, A. Abitol, S. Gonzales-Arias, V. Pisciotti and J. Schwade, **Improved linac dose distributions for radiosurgery with irregularly shaped fields** (Abstr.), Int. J. Radiat. Oncol. Biol. Phys. **19**: 134 (1990).

[31] W. Schlegel, O. Pastyr, T. Bortfeld, G. Becker, L. Schad, G. Gademann and W.J. Lorenz, **Computer systems and mechanical tools for**

stereotactically guided conformation therapy with linear accelerators, Int. J. Radiat. Oncol. Biol. Phys. **24**: 781-787 (1992).

[32] P.H. McGinley, E.K. Butker, I.R. Crocker and R. Aiken, **An adjustable collimator for stereotactic radiosurgery**, Phys. Med. Biol. **37**: 413-419 (1992).

[33] C.F. Serago, A.A. Lewin, P.V. Houdek, S. Gonzalez-Arias, A.A. Abitbol, V.A. Marcial-Vega, V. Pisciotti and J.G. Schwade, **Improved linac dose distributions for radiosurgery with elliptically shaped fields**, Int. J. Radiat. Oncol. Biol. Phys. **21**: 1321-1325 (1991).

[34] K.E. Sixel, E.B. Podgorsak and L. Souhami, **Cylindrical dose distributions in pseudodynamic rotation radiosurgery: an experimental study**, Med. Phys. **20**: 163-170 (1993).

[35] J.D. Bourland and K.P. McCollough, **Static field conformal stereotactic radiosurgery: physicsl techniques**, Int. J. Radiat. Oncol. Biol. Phys. **28**: 471-479 (1993).

[36] R.W. Laing, R.E. Bentley, A.E. Nahum, A.P. Warrington and M. Brada, **Stereotactic radiotherapy of irregular targets: a comparison between static conformal beams and non-coplanar arcs**, Radiother. Oncol **28**: 241-246 (1993).

[37] L.B. Marks, G.W. Sherouse, S. Das, G.C. Bentel, D.P. Spencer and D. Turner, **Conformal radiation therapy with fixed shaped coplanar or noncoplanar radiation beam bouquets: a possible alternative to radiosurgery**, Int. J. Radiat. Oncol. Biol. Phys. **33**: 1209-1219 (1995).

[38] R.J. Hamilton, F.T. Kuchnir, P.Sweeney, S.J. Rubin, M. Dujovny, C.A. Pelizzari and G.T.Y. Chen, **Comparison of static conformal field with multiple noncoplanar arc techniques for stereotactic radiosurgery or stereotactic radiotherapy**, Int. J. Radiat. Oncol. Biol. Phys. **33**: 1221-1228 (1995).

Chapter 2

Basic principles of radiation dosimetry

2.1 Absorbed dose in matter

2.1.1 Definition of dose

The most important quantity in radiotherapy is the absorbed dose D, which is given by:

$$D = \frac{dE_{ab}}{dm}, \qquad (2\text{-}1)$$

where dE_{ab} is the energy absorbed due to ionizing radiation by a mass dm of matter. The SI unit for dose is the gray (Gy) and it is equal to 1 J/kg. The older

unit of rad represents the absorption of 100 ergs of energy by 1 g of absorbing material:

$$1 \text{ rad} = 100 \text{ ergs/g} = 10^{-2} \text{ J/kg} = 1 \text{ cGy} . \qquad (2\text{-}2)$$

In photon beam radiotherapy, dose delivery is the result of a two step process. In the first step, electrons are ejected from atoms of the absorbing medium as a result of various interaction processes between photons and matter. In the second step, these high energy electrons produce ionization and excitation of atoms along their paths, thus transferring their kinetic energy to the medium.

2.1.2 Photon interaction coefficients

For the photon energies encountered in radiotherapy, the four main types of interactions between photons and matter are: coherent scattering, the photoelectric effect, Compton scattering, and pair production. The probability that each of these interactions will occur for a particular photon energy and a particular absorbing material is reflected in its corresponding attenuation coefficient. The linear attenuation coefficient μ (in units of m^{-1}) relates the number of photons dN undergoing an interaction in a thickness dx of absorber, with the number of photons N incident on this absorber:

$$dN = -\mu \cdot N \cdot dx . \qquad (2\text{-}3)$$

The solution to this differential equation is:

$$N(x) = N_o \cdot e^{-\mu x} , \qquad (2\text{-}4)$$

where $N(x)$ is the number of photons that have <u>not</u> undergone an interaction in a thickness x of absorber, and N_o is the number of photons incident on the absorber. This relationship is valid for a monoenergetic beam of photons in a narrow beam geometry.

Attenuation coefficients can be represented in several forms, the most basic form being the linear attenuation coefficient μ . In order to eliminate its dependence on the density of the material, the linear attenuation coefficient is often divided by the density ρ of the absorber. The resulting coefficient, μ/ρ , is called the mass attenuation coefficient and has the units of m^2/kg. The linear attenuation coefficient μ can also be divided by the number of atoms or the number of electrons per unit volume, to give the atomic attenuation coefficient ${}_a\mu$ (in m^2/atom) and the electronic attenuation coefficient ${}_e\mu$ (in m^2/electron), respectively. These three coefficients are related through:

$$ {}_a\mu = \frac{A}{N_A Z} \cdot \frac{\mu}{\rho} \quad \text{and} \qquad (2\text{-}5) $$

$$ {}_a\mu = \frac{A}{N_A} \frac{\mu}{\rho} = Z \cdot {}_e\mu \,, \qquad (2\text{-}6) $$

where A is the mass number of the absorbing medium and N_A is the Avogadro number (6.023×10^{23} atoms/g-atom). Because Z/A ranges between 0.4 and 0.5 for every element (with the exception of hydrogen, for which Z/A is equal to 1), the electronic attenuation coefficient and the mass attenuation coefficient have approximately the same Z dependence (eq. 2-5). The Z dependence of the atomic attenuation coefficient, however, is one order greater than for the electronic attenuation coefficient (eq. 2-6).

Coefficients describing the energy transferred to the medium and the energy absorbed by the medium as a result of an interaction with a photon have also been defined. These coefficients, termed energy transfer coefficient (μ_{tr}) and energy absorption coefficient (μ_{ab}), are given by:

$$ \mu_{tr} = \mu\left(\frac{\overline{E}_{tr}}{h\nu}\right) \qquad \text{and} \qquad \mu_{ab} = \mu\left(\frac{\overline{E}_{ab}}{h\nu}\right). \qquad (2\text{-}7) $$

Here, $\overline{E}_{tr}$ and $\overline{E}_{ab}$ are, respectively, the average energy transferred and the average energy absorbed per interaction, while $h\nu$ is the energy of the incident photon. These two coefficients are related through:

$$\mu_{ab} = \mu_{tr}(1-g)\ , \qquad (2\text{-}8)$$

where g is the fraction of the energy transferred to electrons that is radiated away through the process of bremsstrahlung.

Each of the four major types of photon interactions with matter is represented by its own mass attenuation coefficient. A sum of these individual coefficients gives the total mass attenuation coefficient μ/ρ :

$$\frac{\mu}{\rho} = \frac{\sigma_{coh}}{\rho} + \frac{\tau}{\rho} + \frac{\sigma_c}{\rho} + \frac{\kappa}{\rho}\ , \qquad (2\text{-}9)$$

where σ_{coh}/ρ, τ/ρ, σ_c/ρ, *and* κ/ρ are the mass attenuation coefficients for coherent scattering, photoelectric effect, Compton scattering and pair production, respectively.

2.1.3 Interactions of photons with matter

As mentioned previously, mainly four types of interactions can occur in the photon energy range used in radiotherapy: coherent scattering, photo-electric effect, Compton scattering and pair production.

Coherent scattering (or Rayleigh scattering) is an interaction between a photon and an atom; it is a scattering process in which the photon loses no energy and is usually redirected (scattered) through a small angle. Since there is no energy transferred to the medium, coherent scattering does not contribute to the absorbed dose and is therefore of little interest in radiotherapy.

The photoelectric effect is an interaction between a photon and an atom, in which one of the orbital electrons is ejected from the atom. In the interaction, the photon is totally absorbed, its initial energy $h\nu$ being transferred to both the ejected electron and the recoil atom. Thus, the kinetic energy of the electron is given by:

$$KE_{el} = h\nu - E_b - KE_{recoil} , \qquad (2\text{-}10)$$

where KE_{el} is the kinetic energy of the ejected electron,

$h\nu$ is the energy of the incident photon,

E_b is the binding energy of the electron, and

KE_{recoil} is the kinetic energy given to the recoil atom.

Because the rest mass of the electron is very small compared to that of the recoil atom, KE_{recoil} is nearly zero and is therefore usually neglected. The vacancy that was created in the atomic shell is quickly filled by an electron from an outer shell, with the emission of characteristic X rays or Auger electrons.

The probability of photoelectric absorption depends on the energy $h\nu$ of the incident photon and on the atomic number Z of the medium in which the interaction takes place. In a general fashion, the photoelectric mass attenuation coefficient τ/ρ varies inversely with the cube of the photon energy, except at the absorption edges, where there is a sharp rise in τ/ρ . These absorption edges correspond to the binding energies of the various atomic shells (K shell, L shell, ...) and reflect the fact that the electrons from these shells start participating in the photoelectric process. The photoelectric mass attenuation coefficient also varies approximately with the cube of the atomic number,[1] so that:

$$\frac{\tau}{\rho} \propto \left(\frac{Z}{h\nu}\right)^3 . \qquad (2\text{-}11)$$

For photon energies greater than the binding energy of the K shell, the probability of photoelectric absorption decreases dramatically with energy, while Compton interactions become more and more important. Compton interactions take place between a photon and an essentially free electron. The term free electron means that the energy of the incident photon is much greater than the binding energy of the electron. In this interaction, a photon of energy $h\nu$, upon colliding with a free electron, is scattered with an energy $h\nu'$ at an angle θ relative to its initial direction. A portion of the photon's energy is given to the electron, which departs at an angle ϕ and kinetic energy T. Similarly to the photoelectric effect, vacancies created in the atomic shell are filled with higher shell electrons, followed by the emission of either characteristic radiation or Auger electrons. By the conservation of energy and momentum, it can be shown[2] that the following relationships hold for the Compton effect:

$$h\nu' = h\nu \frac{1}{1+\alpha(1-\cos\theta)},$$

$$T = h\nu \frac{\alpha(1-\cos\theta)}{1+\alpha(1-\cos\theta)}, \text{ and} \qquad (2\text{-}12)$$

$$\operatorname{cotg}\phi = (1+\alpha)\cdot tg\left(\frac{\theta}{2}\right),$$

where $$\alpha = \frac{h\nu}{m_o c^2}. \qquad (2\text{-}13)$$

Cross sections for the Compton process have been derived by Klein and Nishina, who assumed unbound and stationary electrons. These cross sections were found to decrease with increasing photon energy. Furthermore, since the binding energy of the electron was assumed to be zero, the Klein-Nishina cross section per electron ${}_e\sigma$ is independent of the atomic number Z. Thus, the Compton mass attenuation coefficient σ/ρ is also approximately independent of Z, while the atomic attenuation coefficient ${}_a\sigma$ varies with Z^1. Klein-Nishina differential cross sections also indicate that as the energy of the incident

photons increases, the angles through which the electrons are scattered become smaller and smaller (i.e., the electrons are emitted mainly in the forward direction).

Pair production is a process in which a photon, upon interacting with the Coulomb field of an atomic nucleus, gives up all its energy to create an electron and a positron. While the nucleus participates in the conservation of momentum, the kinetic energy that it receives is very close to zero (because of its large mass compared to that of an electron). Therefore, a minimum photon energy of $2\ m_o c^2$ (or 1.022 MeV) is required for this process to occur. If the photon energy is greater than 1.022 MeV, the excess energy is shared, in an arbitrary fashion, as kinetic energy between both the positron and the electron.

Sometimes, pair production occurs in the Coulomb field of an atomic electron. In order to preserve momentum, the atomic electron acquires a significant amount of kinetic energy and is ejected from the atom. Thus, three particles are ejected from the site of interaction (the atomic electron, the created electron, and the positron), hence the name *triplet production*. The threshold energy for triplet production is $4\ m_o c^2$ (2.044 MeV). The relative importance of triplet production is fairly small compared to pair production (on the order of a few percent). Therefore, a single attenuation coefficient, called the pair production attenuation coefficient and denoted by κ, is usually used to describe both processes.

Above the threshold value of 1.022 MeV, the probability for pair production increases rapidly with photon energy. Furthermore, since the effect occurs in the Coulomb field of the nucleus, its probability also increases with the atomic number of the medium. Thus, pair production cross-sections vary with Z^2 per atom, Z per electron, and approximately Z per gram.

In all of the interaction processes discussed above (with the exception of coherent scattering), a certain amount of energy is transferred from the incident photons to the electrons of the absorbing medium. These high energy electrons will, in turn, expend all or part of their kinetic energy in the medium in order to produce absorbed dose. Thus, photoelectric effect, Compton scattering and pair production all contribute to the absorbed dose in the medium. The relative importance of each of these three types of interactions depends on the energy $h\nu$ of the incident photons and on the atomic number Z of the absorbing medium. For photon energies such as those found in radiotherapy, and for low Z media such as water (Z = 7.51) or tissue (Z = 7.64), the Compton effect is by far the most dominant type of interaction. Thus, while both the photoelectric effect and pair production contribute to the absorbed dose in tissue, dose delivery in radiation therapy is mainly due to Compton interactions.

2.1.4 Interactions of electrons with matter

As a result of the interactions between photons and matter, high energy electrons are set in motion in the medium. Because of their Coulomb field, these electrons will interact with practically every atom they pass, whether it be with the atomic electrons or with the atomic nuclei. Therefore, these electrons gradually lose kinetic energy as they travel through the medium. This kinetic energy will either be absorbed by the medium (thereby contributing to the absorbed dose) or radiated away in the form of bremsstrahlung radiation. Thus, interactions between electrons and matter can be classified as either *collisional* or *radiative* .

Collisional interactions include both *soft* and *hard* collisions. *Soft* collisions occur when a high energy electron interacts with atoms from a distance. Because of the long range of the electrostatic force, the electron's Coulomb field interacts with these atoms, exciting and ionizing them as it goes

by. Even though only a small amount of energy is transferred to each atom (only a few eV), these interactions are so numerous that they account for approximately half of the energy absorbed by the medium.[1] In some cases, the high energy electron will suffer a collision with an atomic electron, ejecting it with sufficiently high kinetic energy for it to produce excitation and ionization of atoms along a path of its own. This ejected electron is called a delta (δ) ray, and is the result of what is called a *hard* collision. In both soft and hard collisions, the energy lost by the high speed electron is absorbed in the medium, thereby contributing to the absorbed dose.

A *radiative* interaction is the result of an inelastic collision between an electron and a nucleus. When passing in the vicinity of a nucleus, the electron interacts with the Coulomb nuclear field and suffers a sudden deceleration. As a result, the electron loses all or part of its kinetic energy, which is carried away as electromagnetic radiation by a photon, as described by the Larmor relationship. These photons are usually energetic enough to escape the medium. Therefore, they do not expend their energy in the medium and they do not contribute to the absorbed dose at that point.

The rate at which high energy electrons lose kinetic energy as they travel through a medium is given by the total mass stopping power S_{tot} of the medium, and is typically given in units of MeV cm^2/g. The total mass stopping power S_{tot} is broken down to account for losses due to collisional interactions and losses due to radiative interactions:

$$S_{tot} = S_{col} + S_{rad} , \qquad (2\text{-}14)$$

where S_{col} and S_{rad} are the mass collisional stopping power and the mass radiative stopping power, respectively. The ratio of the radiative stopping power to the collisional stopping power varies with the atomic number Z of the medium and the kinetic energy T of the electron:[1]

$$\frac{S_{rad}}{S_{col}} \propto ZT \,. \qquad (2\text{-}15)$$

Thus, as the kinetic energy of the electron and the atomic number of the medium increase, losses due to radiative interactions become more and more important.

Having described the various processes through which photons and electrons interact with matter in order to produce absorbed dose, we are now in a position to present the basic dosimetric functions that are used in calculating dose distributions. Before doing this, however, it will prove useful to define two additional radiotherapy quantities, kerma and exposure, which are also used to describe the interactions of photons with matter.

2.2 Kerma

Kerma, which is an acronym for kinetic energy released in the medium, describes the initial energy transfer process, the one in which high energy electrons are set in motion via interactions with photons. Kerma is given by:

$$K = \frac{dE_{tr}}{dm} \,, \qquad (2\text{-}16)$$

where dE_{tr} is the sum of the kinetic energies of all of the electrons that where liberated in a volume element of mass dm . It is often convenient to express kerma in terms of the energy fluence ψ and the mass energy transfer coefficient μ_{tr}/ρ . For a polyenergetic photon beam, kerma is given by:

$$K = \psi\left(\frac{\bar{\mu}_{tr}}{\rho}\right), \qquad (2\text{-}17)$$

where $(\bar{\mu}_{tr}/\rho)$ is the weighted average of the mass energy transfer coefficients over the spectrum of photon energies.

Since electrons lose their energy through either collisional or radiative interactions, the total energy transferred E_{tr} can be subdivided into two parts: the part E_{col} that is to be absorbed in the medium (and produce dose) through collisional interactions, and the part E_{rad} that is to be carried away by photons through radiative interactions:

$$E_{tr} = E_{col} + E_{rad} \,. \qquad (2\text{-}18)$$

Thus, kerma can be given by:

$$K = K_{col} + K_{rad} \,, \qquad (2\text{-}19)$$

where $K_{col} = \frac{dE_{col}}{dm}$ is the collisional kerma, and (2-20)

$K_{rad} = \frac{dE_{rad}}{dm}$ is the radiative kerma. (2-21)

Collisional kerma is the part of kerma that is of interest in radiation dosimetry since it is the one responsible for the absorbed dose. Similarly to equation 2-17, K_{col} can be expressed in terms of the energy fluence ψ and the average mass energy absorption coefficient $(\overline{\mu}_{ab}/\rho)$:

$$K_{col} = \psi\left(\frac{\overline{\mu}_{ab}}{\rho}\right). \qquad (2\text{-}22)$$

Because high energy electrons do not deposit their energy at their site of origin but rather along their paths as they travel through the medium, kerma and absorbed dose do not occur at the same location. Therefore, one cannot relate the absorbed dose to the energy fluence of a photon beam (as was done for kerma) unless a state of electronic equilibrium or transient electronic equilibrium exists. Electronic equilibrium in a volume V occurs when, for each electron of a given energy leaving V, there is an electron with the same energy entering V. If this is the case, the absorbed dose D is equal to the collisional kerma K_{col}:

$$D = K_{col} . \qquad (2\text{-}23)$$

Transient electronic equilibrium, on the other hand, exists when the absorbed dose is proportional to the collisional kerma. This is illustrated in FIGURE 2-1, where kerma, collisional kerma, and absorbed dose are plotted as a function of depth in medium, when a beam of photons is perpendicularly incident on this medium. Both kerma and collisional kerma are maximum at the surface of the material and decrease exponentially with depth because of photon attenuation. Absorbed dose, however, first increases with depth. As discussed in the section on Compton interactions, electrons in the medium are mainly emitted in the forward direction (in the direction of the incident photons). Therefore, high energy electrons produced at the surface of the medium deposit their energy as they travel deeper in the material. Thus, the initial increase in dose with depth is simply due to the increase in the number of electrons set in motion (i.e., increase in the number of electron tracks). Dose will reach its maximum value at a depth approximately equal to the range of secondary electrons in the medium, after which it will start to decrease due to the attenuation of photons. At a depth equal to the maximum range (r_{max}) of secondary electrons in the medium, transient electronic equilibrium sets in, and the dose becomes proportional to the collisional kerma. The dose is then given by:

$$D = \beta \cdot K_{col} , \qquad (2\text{-}24)$$

where β is a constant of proportionality. Because the dose is produced by electrons that were liberated at a lower depth, where the photon fluence and the collisional kerma are greater, β is slightly larger than unity and D is slightly greater than K_{col}. In practice, however, because of its value very close to unity, β is usually neglected.[2] The depth at which the dose reaches its maximum value is called the depth of dose maximum (d_{max}) and the region between the surface of the material and d_{max} is called the build-up region.

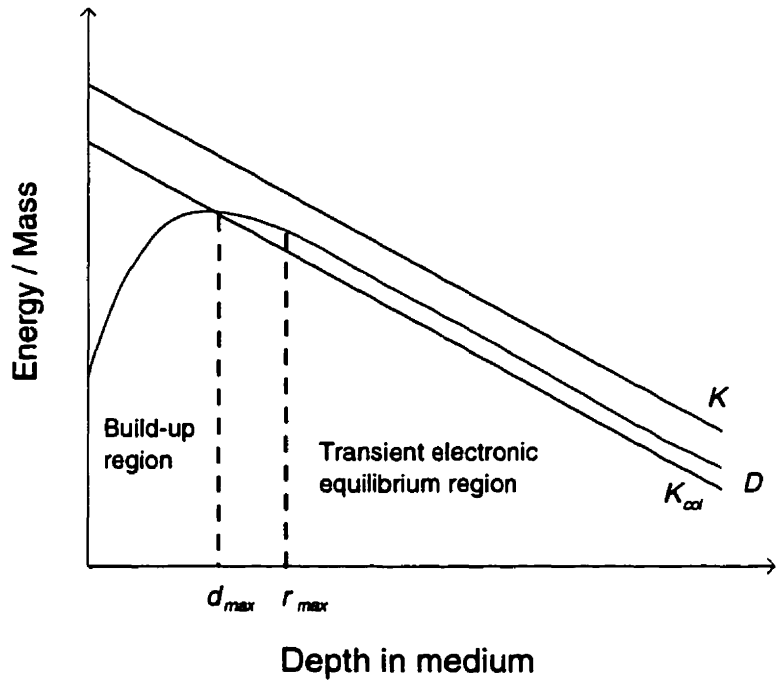

FIGURE 2-1 *Kerma K, collisional kerma K_{col}, and absorbed dose D as a function of depth when a photon beam is perpendicularly incident on absorbing medium.*

2.3 Exposure

Exposure is a quantity that measures the ionization produced in air by photons. It is given by:

$$X = \frac{dQ}{dm}, \qquad (2\text{-}25)$$

where dQ is "the absolute value of the total charge of the ions of one sign produced in air when all the electrons (negatrons and positrons) liberated by photons in air of mass dm are completely stopped in air".[3] Although its SI unit is the coulomb per kilogram (C/kg), exposure is often measured in Roentgens (R), one Roentgen being equal to 2.58×10^{-4} C/kg of air.

The only method for directly measuring the exposure is provided by the standard air chamber. Standard air chambers (also called free-air ionization

chambers) are found in national standards laboratories and are mainly used in the calibration of secondary ionization chambers designated for clinical use. Because the standard air chamber must operate under the condition of electronic equilibrium, exposure cannot be accurately measured for photon energies greater than approximately 3 MeV. Above this energy, the large range of the secondary electrons liberated in air would necessitate very large chambers, thereby introducing such complications as photon attenuation, photon scatter, and a reduction in ion collection efficiency.[4]

Exposure can also be defined with respect to the energy fluence of a photon beam:[3]

$$X = \psi \left(\frac{\bar{\mu}_{ab}}{\rho} \right)_{air} \left(\frac{e}{\bar{W}} \right)_{air} \qquad (2\text{-}26)$$

$$= K_{c_{air}} \left(\frac{e}{\bar{W}} \right)_{air}, \qquad (2\text{-}27)$$

where $K_{c_{air}}$ is the collisional kerma in air and $(\bar{W}/e)_{air}$ is the average energy required to produce an ion pair in air. For dry air, $(\bar{W}/e)_{air}$ is equal to 33.97 eV/ion pair (i.e., 33.97 J/C). Thus, the air collisional kerma can be written as:

$$K_{c_{air}} = X \left(\frac{\bar{W}}{e} \right)_{air} . \qquad (2\text{-}28)$$

If the exposure is given in units of Roentgens (R), the collisional kerma in air becomes:

$$K_{c_{air}} = X(R) \cdot \left(2.58 \times 10^{-4} \frac{C/kg}{R} \right) \cdot \left(33.97 \frac{J}{C} \right) = X(R) \cdot 0.00876 \frac{J/kg}{R} . \qquad (2\text{-}29)$$

In some situations, one is interested in relating the dose to a small mass of medium in air ($D_{\Delta m}$) to the exposure X in air. If we introduce a small mass of

medium Δm into the beam, the collisional kerma $K_{c_{\Delta m}}$ to this small mass of medium is given by (from eq. 2-22):

$$K_{c_{\Delta m}} = \psi_{med} \cdot \left(\frac{\overline{\mu}_{ab}}{\rho} \right)_{med} . \qquad (2\text{-}30)$$

If the mass of medium is so small that it does not perturb the energy fluence of the photon beam, $\psi_{med} = \psi_{air}$ and

$$K_{c_{\Delta m}} = K_{c_{air}} \left(\frac{\overline{\mu}_{ab}}{\rho} \right)_{air}^{med} = X(R) \cdot 0.00876\ (Gy / R) \cdot \left(\frac{\overline{\mu}_{ab}}{\rho} \right)_{air}^{med} , \qquad (2\text{-}31)$$

where $(\overline{\mu}_{ab}/\rho)_{air}^{med}$ is the ratio of the mean mass energy absorption coefficient of the medium to that of air. In order to obtain the absorbed dose, just enough material is added to the small mass of medium so that electronic equilibrium is achieved. Absorbed dose then becomes equal to the collisional kerma and:

$$D_{\Delta m} = X(R) \cdot 0.00876(Gy / R) \cdot \left(\frac{\overline{\mu}_{ab}}{\rho} \right)_{air}^{med} \cdot k(r_{med}) \qquad (2\text{-}32)$$

$$= X(R) \cdot f_{med} \cdot k(r_{med}) , \qquad (2\text{-}33)$$

where $k(r_{med})$ is a factor that accounts for the difference in photon attenuation between air and the phantom material of radius r.

2.4 *Dosimetric functions*

Prior to irradiating a patient, the dose that any given point within the irradiated volume will receive must be accurately known. Such a three dimensional description of the dose within the patient is called a dose distribution. Because it is rarely possible to measure them directly in patients, dose distributions must be calculated. Several dosimetric functions have

therefore been developed which allow for the calculation of the absorbed dose at any given point, thereby enabling us to predict dose distributions within the patient before commencing the treatment. These dosimetric functions will be defined and discussed in the remainder of this chapter.

2.4.1 Percentage depth dose

One of the most basic functions used in radiation dosimetry is the percentage depth dose (*PDD*). The percentage depth dose relates the dose D_Q at any depth d in the medium, to the dose D_P at a reference depth d_r along the beam central axis (FIGURE 2-2):

$$PDD(d,A,SSD,E) = \frac{D_Q}{D_P} \cdot 100 \ , \qquad (2\text{-}34)$$

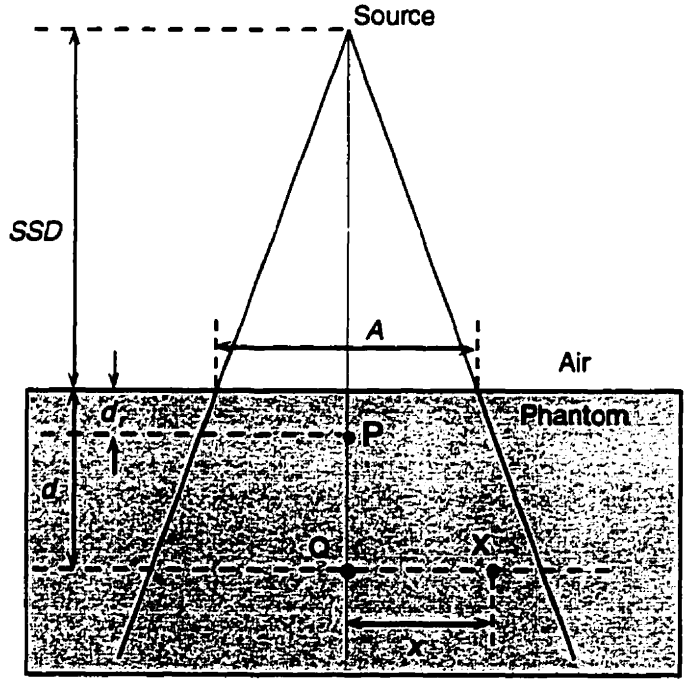

FIGURE 2-2 *Schematic representation of the geometrical parameters involved in the definition of percentage depth dose (PDD) and off-axis ratio (OAR).*

where d is the depth of point Q in the phantom, A is the size of the radiation field at the surface of the phantom, E is the energy of the photon beam and SSD is the source-surface distance. For convenience, the depth of dose maximum d_{max} is generally taken as the reference depth. Apart from its obvious dependence on depth (which was discussed in section 2.2), the percentage depth dose also depends on the field size A, the source-surface distance SSD, and the energy E of the photon beam. A method for converting percentage depth doses from one SSD to another will be derived in section 2.4.4.

2.4.2 Off-axis ratio

While the percentage depth dose is used to relate the dose to points located at different depths along the beam central axis, the off-axis ratio (OAR) is used to relate the dose to points located at the same depth but at different off-axis positions. The off-axis ratio is given by (FIGURE 2-2):

$$OAR(d,x,A) = \frac{D_X}{D_Q}, \qquad (2\text{-}35)$$

where d is the depth in phantom of points Q and X, A is the radiation field size, and x is the distance (along a line perpendicular to the beam central axis) between the beam central axis and point X.

Off-axis ratios at a given depth can be obtained from the measured beam profile simply by normalizing the profile to a value of 1 on the beam central axis. A typical OAR curve is shown in FIGURE 2-3. This curve was obtained from the measured beam profile of a 5x5 cm^2 10 MV photon beam at a depth of 10 cm in water, at the nominal SSD of 100 cm. Ideally, OAR curves would resemble a step function, with a value of 1 in the open part of the field and a value of 0 in the blocked part of the field. This, however, is not the case, as can be seen in FIGURE 2-3; at the edge of the radiation field, the OAR curve follows a steep but finite gradient. The term penumbra is given to this high dose gradient

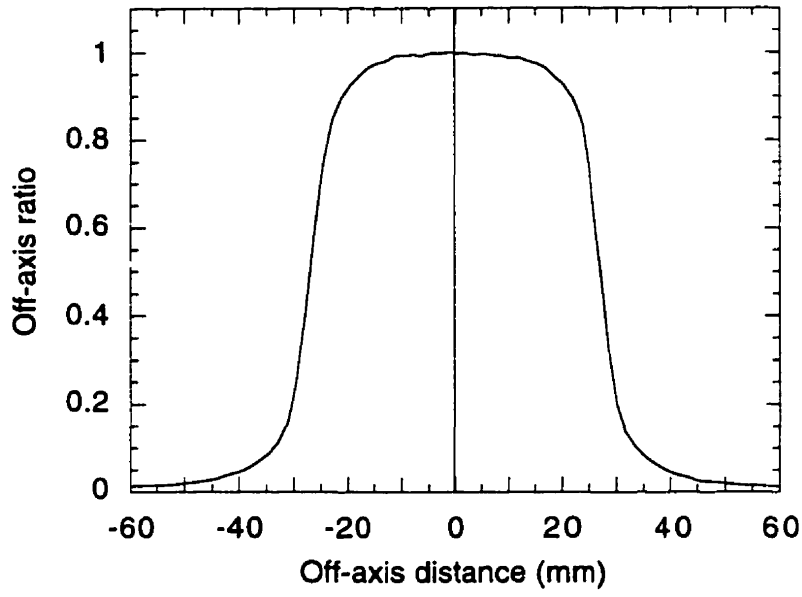

FIGURE 2-3 *Off-axis ratio (OAR) curve for a 5x5 cm² 10 MV photon beam at a depth of 10 cm in water at the nominal SSD of 100 cm. The vertical solid line in the middle of the graph represents the central axis of the radiation beam.*

region.[5] In order to account for the different causes of penumbra, penumbra is categorized into two parts: geometrical and physical penumbra. The geometrical penumbra arises from the fact that the radiation source is not a point source, while the physical penumbra is a result of scattered radiation within the phantom.

2.4.3 SAD setup

Most radiotherapy treatment machines are isocentrically mounted; the gantry (and therefore the radiation source) moves in a circle around the gantry axis of rotation. The intersection between the axis of rotation of the gantry and the central axis of the radiation beam is called the isocenter, while the distance

between the radiation source and the isocenter is called the source-axis distance *SAD*. In the SAD setup (or isocentric setup), the patient is positioned so that the center of the target to be irradiated coincides with the isocenter of the treatment machine. Several coplanar or non-coplanar beams are then used to irradiate the target. Since each beam can have a different source-surface distance and a different surface field size (depending on the depth of the target inside the patient), the use of *PDDs* for the calculation of dose distributions becomes difficult and cumbersome. It is therefore convenient to define new quantities to calculate the depth dose along the beam central axis, which are independent of *SSD* and surface field size.

2.4.4 Tissue-air ratio and peak scatter factor

The tissue-air ratio (*TAR*) is defined as the dose D_Q at a particular point in the phantom, divided by the dose $D_{Q_{\Delta m}}$ to a small mass of medium in air at the same point relative to the radiation source (FIGURE 2-4):

$$TAR(d, A_Q, E) = \frac{D_Q}{D_{Q_{\Delta m}}}, \qquad (2\text{-}36)$$

where d is the depth of point Q in phantom, A_Q is the field size projected at depth d, and E is the energy of the radiation beam. One of the great advantages of the *TAR* is that it is essentially independent of the distance from the source. This is because the scatter contribution to the dose at point Q is approximately independent of the divergence of the beam; it depends only on the depth d below the surface of the phantom and on the field size A_Q at that particular depth.[2] Thus, for a given photon energy, the *TAR* depends only on d and A_Q.

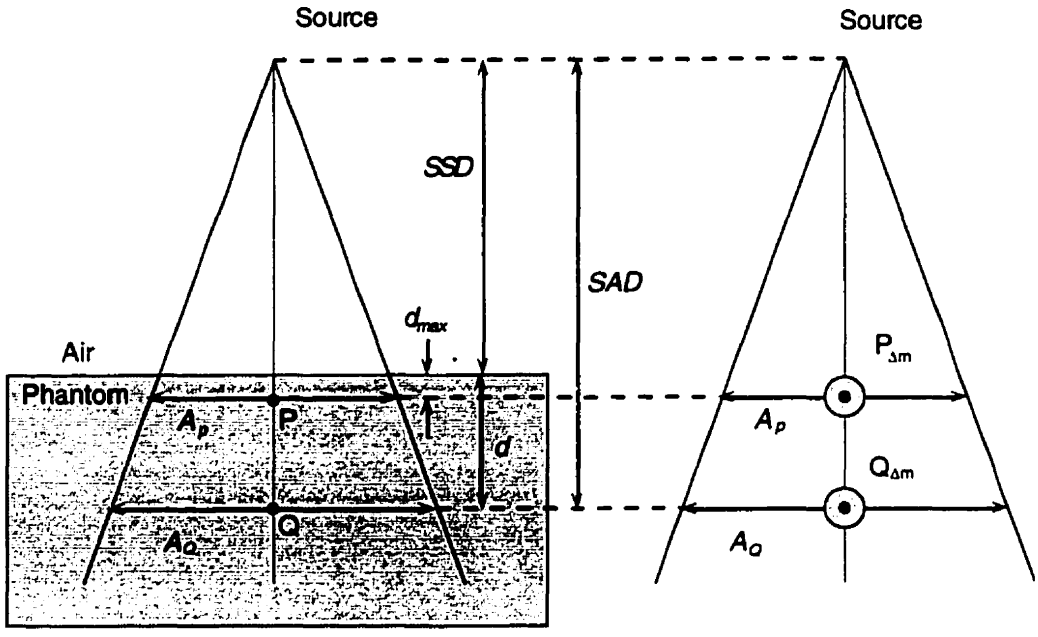

FIGURE 2-4 *Schematic representation of the geometrical parameters involved in the definition of tissue-air ratio (TAR) and peak scatter factor (PSF).*

The peak scatter factor (also called the backscatter factor) is the tissue-air ratio for the special case where the depth d is equal to the depth of dose maximum d_{max}. It is given by:

$$PSF(A_P, E) = TAR(d_{\max}, A_P, E) = \frac{D_P}{D_{P_{\Delta m}}} . \qquad (2\text{-}37)$$

The peak scatter factor measures the increase in dose at d_{max} due to scattered radiation in the phantom. Traditionally, it was used for photon beams in the orthovoltage range (150 to 500 kV).[4] For these beams, d_{max} is nearly zero and the increase in dose at the surface is due to backscatter from within the phantom, hence the name *backscatter factor*.

It is possible to express *PDDs* in terms of *TARs* and *PSFs*. From eq. 2-34 and 2-37,

$$PDD(d,A,SSD,E) = 100 \cdot \frac{D_Q}{D_P} = 100 \frac{D_Q}{D_{P_{\Delta m}} \cdot PSF(A_P,E)} . \qquad (2\text{-}38)$$

From eq. 2-36 and the inverse square law,

$$TAR(d,A_Q,E) = \frac{D_Q}{D_{Q_{\Delta m}}} = \frac{D_Q}{D_{P_{\Delta m}} \cdot \left(\frac{SSD + d_{\max}}{SSD + d}\right)^2} . \qquad (2\text{-}39)$$

By isolating $D_Q / D_{P_{\Delta m}}$ in both expressions, and by solving for *PDD(d,A,SSD,E)* , we obtain:

$$PDD(d,A,SSD,E) = 100 \cdot \frac{TAR(d,A_Q,E)}{PSF(A_P,E)} \cdot \left(\frac{SSD + d_{\max}}{SSD + d}\right)^2 . \qquad (2\text{-}40)$$

From this expression, we can derive a method of converting percentage depth dose from one *SSD* to another. Suppose we have two beam geometries that have the same surface field size *A* , but different source-surface distances f_1 and f_2 (FIGURE 2-5). Let A_{Q1} and A_{Q2} be the field sizes projected at depth *d* for the source-surface distances f_1 and f_2 , respectively. From equation 2-40,

$$PDD(d,A,f_1,E) = 100 \cdot \frac{TAR(d,A_{Q_1},E)}{PSF(A_P,E)} \cdot \left(\frac{f_1 + d_{\max}}{f_1 + d}\right)^2 \text{ and} \qquad (2\text{-}41)$$

$$PDD(d,A,f_2,E) = 100 \cdot \frac{TAR(d,A_{Q_2},E)}{PSF(A_P,E)} \cdot \left(\frac{f_2 + d_{\max}}{f_2 + d}\right)^2 . \qquad (2\text{-}42)$$

Therefore,

$$PDD(d,A,f_2,E) = PDD(d,A,f_1,E) \cdot \frac{TAR(d,A_{Q_2},E)}{TAR(d,A_{Q_1},E)} \cdot \left[\frac{(f_2 + d_{\max}/f_2 + d)^2}{(f_1 + d_{\max}/f_1 + d)^2}\right] \qquad (2\text{-}43)$$

The term in brackets is called the Mayneord factor. Thus, in order to account for a change in *SSD* , the percentage depth doses must be multiplied by the Mayneord factor and by the ratio of *TARs* for field sizes A_{Q1} and A_{Q2} .

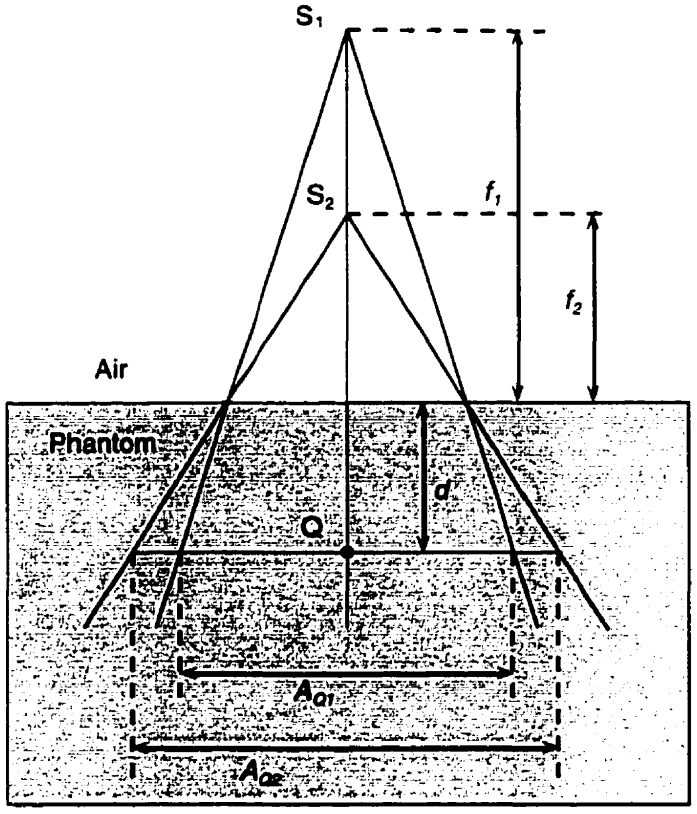

FIGURE 2-5 *Schematic representation of two different irradiation geometries having the same surface field size A, but different source-surface distances (f_1 and f_2).*

2.4.5 Tissue-phantom ratio and tissue-maximum ratio

For high energy photon beams, the dose to a small mass of medium in air $D_{\Delta m}$ is not easily measured. As the energy of the photon beam increases, so does the range of the secondary electrons and, consequently, the size of the build-up cap required by the dosimeter to provide electronic equilibrium. For very high photon energies, the size of the build-up cap might become too large for it to be used with small fields. Therefore, a new quantity has been defined, the tissue-phantom ratio (*TPR*), which does not require dose measurements in air. The tissue-phantom ratio is defined as the ratio of the dose at a particular depth d in phantom, to the dose at a point located at the same distance from the source, but at a fixed reference depth d_r below the surface (FIGURE 2-6):

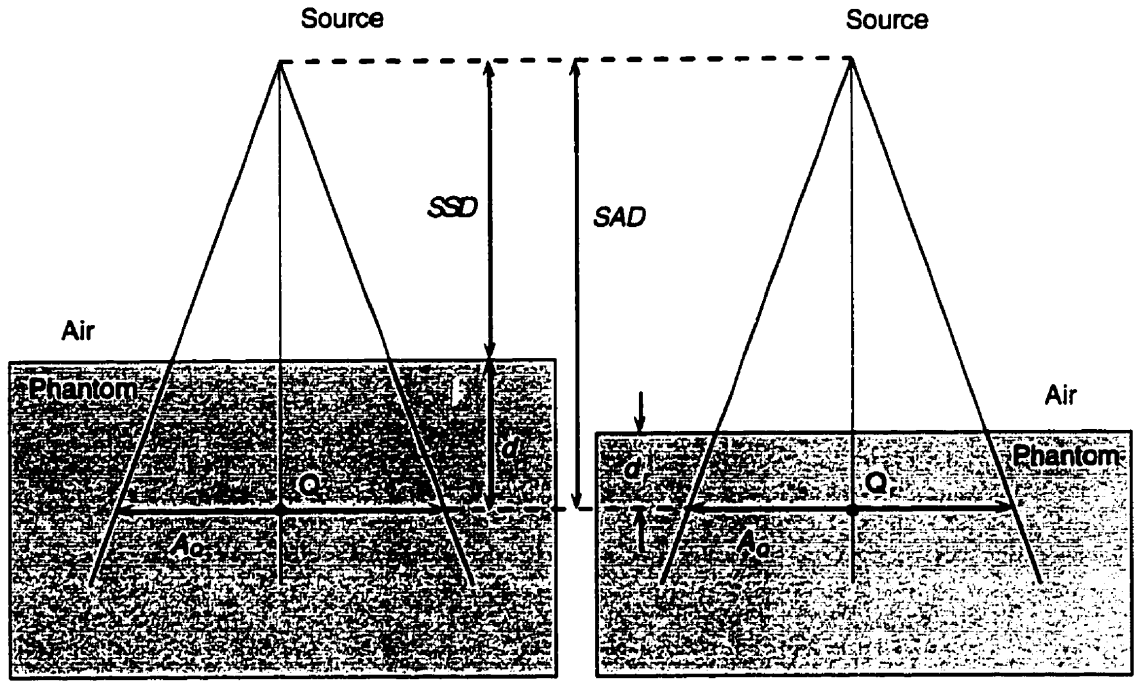

FIGURE 2-6 *Schematic representation of the geometrical parameters involved in the definition of tissue-phantom ratio (TPR).*

$$TPR(d,d_r,A_Q,E)=\frac{D_Q}{D_{Q_r}}\ . \qquad (2\text{-}44)$$

Similarly to the tissue-air ratio, the tissue-phantom ratio is also essentially independent of the distance from the source. If the depth of dose maximum d_{max} is chosen as the depth of reference, the resulting tissue-phantom ratios are called tissue-maximum ratios (*TMRs*).

2.4.6 Relative dose factor

The relative dose factor (*RDF*) is defined as the dose (or dose rate) at d_{max} in a phantom for a given field size A , divided by the dose (or dose rate) at d_{max} for a 10x10 cm^2 field (measured at nominal *SSD*):

$$RDF(A,E) = \frac{D_P(A,\mathrm{E})}{D_P(10\mathrm{x}10\ \mathrm{cm}^2,\mathrm{E})}\ . \qquad (2\text{-}45)$$

Since the dose at d_{max} in a phantom is equal to the dose to a small mass of medium in air $D_{P_{\Delta m}}$ multiplied by the peak scatter factor PSF,

$$RDF(A,E) = CF(A,E)\cdot SF(A,E)\ , \qquad (2\text{-}46)$$

where $CF(A,\mathrm{E}) = \dfrac{D_{P_{\Delta m}}(A,\mathrm{E})}{D_{P_{\Delta m}}(10\mathrm{x}10\ cm^2,\mathrm{E})}$ is the collimator scatter factor and (2-47)

$SF(A,\mathrm{E}) = \dfrac{PSF(A,\mathrm{E})}{PSF(10\mathrm{x}10\ cm^2,\mathrm{E})}$ is the phantom scatter factor. (2-48)

The collimator scatter factor (often called the output factor) measures the increase of the beam output with field size due to increased scatter from the collimator of the treatment machine head. The phantom scatter factor, on the other hand, takes into account the increase with field size of the scatter radiation originating in the phantom only. Together, these two quantities measure the increase of the dose at d_{max} in phantom due to an increase in field size.

2.4.7 Scatter-air ratio and scatter-phantom ratio

The dose at any point in a medium (or in a phantom) can be separated into primary and scattered components. In some situations, it might be useful to separate these components by calculating the dose due to scattered radiation only. This can be done by using the scatter-air ratio (SAR), which is defined as the dose due to scattered radiation at a given point in phantom, divided by the dose to a small mass of medium in air at the same point relative to the radiation source. The SAR is given by:

$$SAR(d,A_Q) = TAR(d,A_Q) - TAR(d,0). \qquad (2\text{-}49)$$

Since a zero area field contains no scattered radiation, *TAR(d,0)* represents the primary component of a beam. Thus, the contribution of the scattered radiation to the total dose is obtained by subtracting the tissue-air ratio of a zero area field from the tissue-air ratio of the field A_Q under consideration.

For high energy photons, the scatter-phantom ratio (*SPR*) is used:[4]

$$SPR(d,A_Q) = TPR(d,A_Q) \cdot \frac{SF(A_Q)}{SF(0)} - TPR(d,0) \qquad (2\text{-}50)$$

In the above equation, the *TPRs* can be substituted by *TMRs* to give the scatter-maximum ratio (*SMR*).

2.5 Summary

In this chapter, the fundamental concepts inherent to radiation dosimetry were presented. Thus, basic radiotherapy quantities such as absorbed dose, exposure and kerma were defined. A brief overview of the various processes through which photons and electrons interact with matter in order to produce absorbed dose was also given. Finally, the basic dosimetric functions (*PDD, OAR, TMR,...*) used in calculating dose distributions were defined.

2.6 References

[1] F.H. Attix, **Introduction to Radiological Physics and Radiation Dosimetry**, John Wiley & Sons, New York (1986).

[2] H.E. Johns and J.R. Cunningham, **The Physics of Radiology**, 4th Ed., Thomas Publisher, Springfield IL. (1983).

[3] International Comission on Radiation Units and Measurements, **Radiation quantities and units**, ICRU Report No. 33 (1980).

[4] F.M. Khan, **The Physics of Radiation Therapy**, 2nd Ed., Williams & Wilkins, Baltimore MD. (1984).

[5] International Comission on Radiation Units and Measurements, **Determination of absorbed dose in a patient irradiated by beams of x or gamma rays in radiotherapy procedures**, ICRU Report No. 24 (1976).

Chapter 3

Experimental apparatus and techniques

3.1 Linear accelerator

Stereotactic radiosurgery at McGill University is performed using 10 MV photons from a Clinac-18 linear accelerator (Varian Associates, Palo Alto, Ca). This linac is isocentrically mounted with a source-axis distance (SAD) of 100 cm. It has the capabilities of producing either electron beams (of discrete energies between 6 MeV and 18 MeV) or 10 MV photon beams (continuous spectrum of energies between 0 and 10 MeV). A brief overview of the principles of the linac operation is given in this section. A more detailed description can easily be found in the literature.[1,2,3]

A schematic representation of the major components comprising typical medical linear accelerators is shown in FIGURE 3-1. Free electrons are produced at the electron gun by thermionic emission from a hot tungsten

filament. These free electrons are electrostatically accelerated toward the accelerating waveguide, into which they are injected with an initial kinetic energy between 25 and 100 keV. Inside the waveguide, the electrons are accelerated by high frequency electromagnetic waves (S-band at 2856 MHz) that were produced in the RF driver and further amplified by the klystron. A power supply provides DC voltage to the modulator, which simultaneously delivers high voltage pulses to both the klystron and the electron gun. Thus, microwave pulses from the klystron are injected in the accelerating waveguide as are the electron pulses from the electron gun. In order for the electrons to be captured by the electromagnetic wave, the phase velocity of the wave must be reduced to correspond to the velocity of the injected electrons. This is done by loading the waveguide with discs (or diaphragms) of varying aperture and spacing, hence the name *disc-loaded waveguide*.

The electron beam exits the accelerating waveguide in the form of a pencil beam approximately 3 mm in diameter[4] and enters the beam transport system. The beam transport system, located in the head of the linac, contains the necessary components required to transform the pencil beam of high

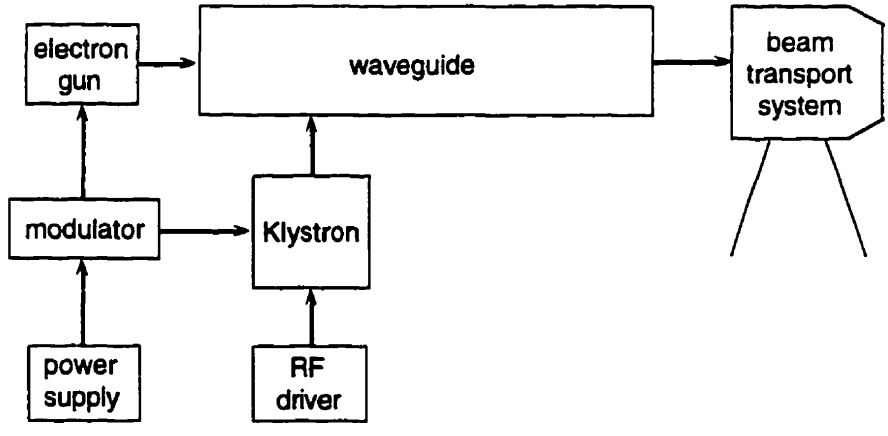

FIGURE 3-1 *Schematic representation of the major components of typical medical linear accelerators.*

energy electrons into a clinically usable beam of high energy photons or electrons: the bending magnets, the X-ray target, the flattening filter and the scattering foils, the ionization chambers, and the collimation system. A detailed diagram of the Clinac-18 treatment head, operating in the photon mode, is given in FIGURE 3-2 (taken from Zankowski [5]).

After leaving the waveguide, the electron beam is first bent through 270° by achromatic bending magnets which produce a magnetic field in a plane perpendicular to the electron beam trajectory. In the photon mode, the electron beam then strikes a 1 cm thick copper target, thus transforming some of the kinetic energy of the electrons into X-ray photons through the process of bremsstrahlung. The resulting photon beam has a continuous spectrum of energies ranging between 0 MeV and a maximum energy, which is equal to the incident electron kinetic energy. A 10 MV photon beam is referred to as the photon beam that is produced by 10 MeV electrons.

The bending magnets and the X-ray target are located inside the vacuum sealed part of the beam transport system. Before exiting this evacuated region (via a thin beryllium window), primary tungsten collimators are used to define the maximum diagonal dimension of the radiation field. Because of the high kinetic energy of the electrons impinging upon the copper target, the X-ray beam leaving the target is highly non-uniform; it is strongly peaked in the forward direction. In order to produce a uniform radiation field, a tungsten flattening filter is placed in the path of the photon beam. This flattening filter is designed in such a way that the intensity of the beam is uniform over the largest possible field (defined by the primary collimator) at a depth of 10 cm in a water equivalent phantom, at the nominal SSD of 100 cm.

In order to measure the integrated dose, the flattened photon beam is incident on a dual transmission ionization chamber. These chambers measure the dose in monitor units (MUs), which are made to correspond to centiGrays

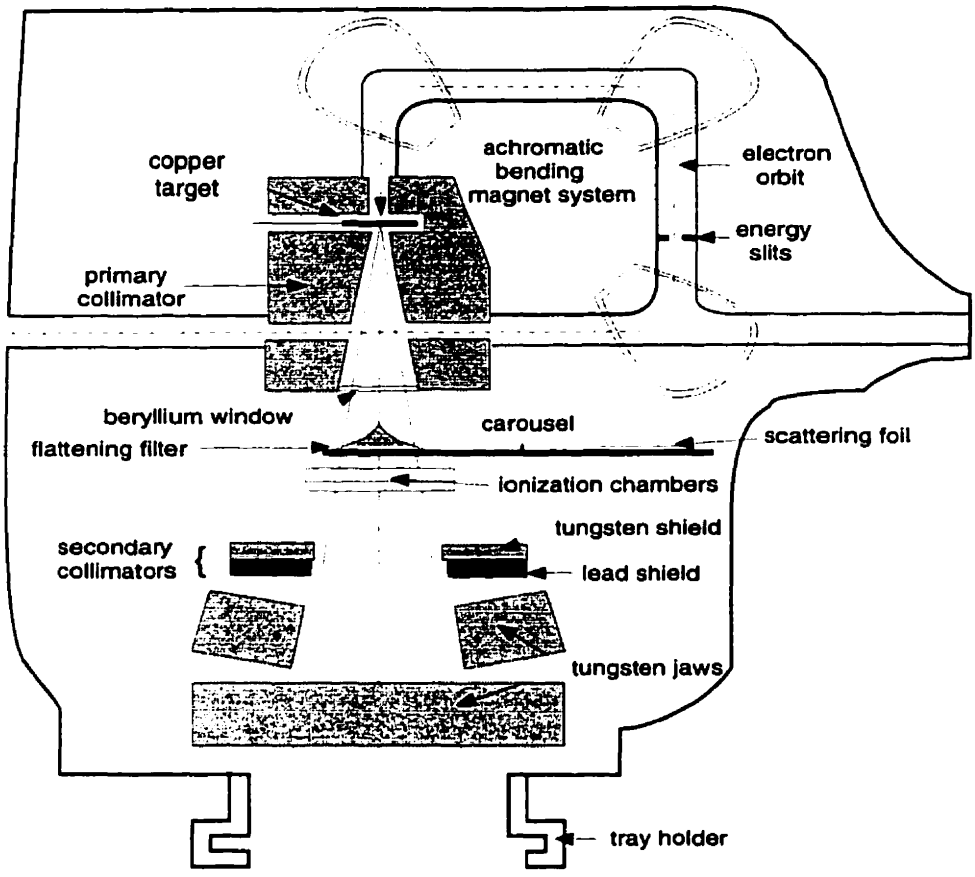

FIGURE 3-2 *Schematic representation of the Clinac-18 treatment head operating in the photon mode. Taken from Zankowski.*[5]

(cGys) at the depth of dose maximum inside a water equivalent phantom located at nominal SSD, when irradiated with a 10x10 cm^2 photon or electron beam. Once the integrated dose measured by the primary chamber reaches a predetermined level (in MUs), the radiation beam is automatically terminated. In order to ensure patient safety, the two chambers are independent of each other; if the primary chamber fails, the secondary chamber will stop the

irradiation when it has reached its preset number of MUs, which usually exceeds the preset value on the primary chamber by several MUs.

After passing through the ion chambers, the beam is further collimated by a pair of fixed secondary collimators (the upper shield being composed of tungsten and the lower shield of lead), which define the largest square photon beam clinically usable. Finally, two pairs of movable tungsten jaws are used to obtain the desired square or rectangular treatment field. In order to reduce the beam penumbra, these jaws are mounted so that their edge is always along the beam fanline defining the size of the radiation field.

As mentioned above, the Clinac-18 can also operate in the electron mode. If this is the case, the copper target is removed from the path of the electron beam, and the flattening filter is replaced by a scattering foil, which transforms the 3 mm diameter electron pencil beam into a large uniform electron beam, thus making it clinically usable.

3.2 Dosimetry techniques

3.2.1 Ion chambers

Because of its ease of use, its high reproducibility and its high reliability, the ion chamber is the most commonly used type of dosimeter. As an absolute dosimeter, the ion chamber is used to measure the output of treatment machines, as well as to provide a calibration for other types of relative dosimeters, such as film and thermoluminescent dosimeters (TLDs).

An ion chamber consists of a gas filled cavity, placed between two electrodes: a collecting electrode and a polarizing electrode. A potential difference is applied between these two electrodes, producing an electric field inside the cavity. When radiation passes through the gas, secondary electrons

are set in motion, thus ionizing the gas within the cavity. Due to the presence of the electric field, positive and negative ions produced in the chamber gas will separate and migrate toward their respective electrode. An electrometer is then used to measure the total charge collected, or the current produced, at the collecting (measuring) electrode. The potential difference between the two electrodes must be low enough to avoid charge amplification, while also being large enough to minimize the recombination of positive and negative ions. A voltage of 300 V is typically used for this purpose.

There are many forms of ion chambers (standard free air, parallel plate, etc.), but the most widely used clinically, and the one used in the present work, is the thimble ionization chamber. Typically, the thimble chamber consists of a cylindrical arrangement of two electrodes, as shown in FIGURE 3-3. The central collecting electrode is basically a rod of low atomic number material, such as aluminum or graphite. The polarizing electrode usually consists of a thin conducting layer of graphite coated on the inner surface of the thimble wall. A potential difference is applied between these two electrodes, which are separated by a material that provides electrical insulation. While the gas within the chamber is usually air at ambient temperature and pressure, the material making the thimble wall depends on the quantity to be measured. If one wants

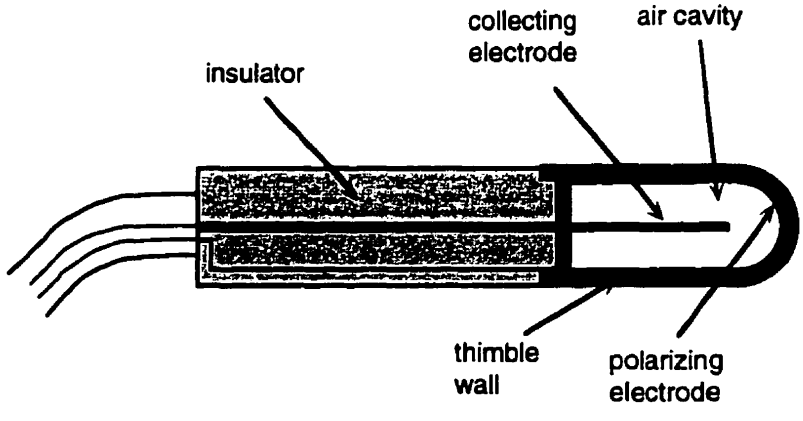

FIGURE 3-3 *Schematic representation of a thimble ionization chamber.*

to measure the exposure in air, the thimble wall should be made of an air-like material. If, however, one wants to measure the absorbed dose in tissue, the wall should be made of a water-like or tissue-like material.[6] In order to prevent electrons originating outside the wall from entering the cavity (and to ensure electronic equilibrium inside the gas cavity), the thickness of the thimble wall should be made equal to or greater than the maximum range of secondary electrons in the wall material. Typical wall materials include graphite, bakelite, and other plastic materials.[7] The chamber is connected to an electrometer, which can be used in either the integral mode or the differential mode. In the integral mode, the total charge collected by the collecting electrode is measured (thus giving the total dose), while in the differential mode, it is the electrical current that is measured (thus giving the instantaneous dose rate).

The chamber used for our measurements was an RK type thimble chamber (Scanditronix AB, Uppsala, Sweden) with an air cavity volume of 0.12 cm^3, an outer diameter of 7.0 mm, and a length of 25.0 mm. This chamber was uniquely used in conjunction with the RFA 300 radiation field analyzer (Scanditronix AB, Uppsala, Sweden), which will be described in section 3.3.1.

3.2.2 Diode detectors

Because of their small sensitive volume and their high sensitivity, diode detectors are particularly useful in measurements requiring a high spatial resolution (e.g., measurements in the penumbra region of radiation beams) or in regions where the dose rate is very small. A diode is made simply by the joining of a p-type semiconductor with an n-type semiconductor, hence the name *p-n junction* . The most commonly used type of semiconductor is silicon (Si), although germanium (Ge) is also used quite often. Because the absorbing properties of Si (Z=14) and Ge (Z=32) are very different than that of air or water, diode detectors show a large energy dependence. Furthermore, since the energy required to produce an electron-hole pair in the diode is relatively small

(on the order of a few eV), diode detectors also suffer from temperature dependence.

In a semiconductor, electrons may occupy energy levels located within certain allowed energy bands. Electrons in the valence band are bound to atoms in the lattice, while electrons in the conduction band are free to move around the crystal and conduct electrical current. These two bands are separated by the forbidden gap, the size of which varies from material to material. For typical semiconductors, this energy gap is usually less than 2 eV. More precisely, at a temperature of 300 K, this energy gap is 1.12 eV for silicon and 0.67 eV for germanium.[8] Small amounts of impurities may be introduced in the semiconductor in order to make it an electron donor (n-type), in which conduction occurs predominantly by electrons, or an electron acceptor (p-type), in which conduction occurs predominantly by positive holes. If two such crystals are joined together, the positive holes from the p-type side and the electrons from the n-type side will attract each other, eventually canceling each other out near the boundary of the two regions. This creates a region, the depletion layer, which contains no mobile charge carriers. This also leaves an excess of positive charge on the n-type side of the depletion layer and an excess of negative charge on the p-type side, thus creating an electric field within the depletion layer.

The depletion layer serves as the sensitive volume of the diode detector, with the n-type and p-type regions outside the depletion layer acting like the electrodes of the detector (not unlike the polarizing and collecting electrodes of an ion chamber). When radiation passes through the depletion layer, electron-hole pairs are formed when valence electrons are raised to the conduction band. The mean energy required to form an ion pair in Si is 3.6 eV (compared to 33.97 eV in air).[9] As a result of the built-in potential and electric field, the electron is drawn toward the n-type region while the positive hole is drawn toward the p-type region. The current produced or the charge collected is then

measured through an appropriate external circuit. Because no external voltage was applied across the detector, the detector is said to have been used in the photo-voltaic mode.

The diode detector used for our measurements was a p-type silicon semiconductor detector (Scanditronix AB, Uppsala, Sweden), whose sensitive volume has a diameter of 2.5 mm and a thickness of 60 μm, for a volume of 0.30 mm^3. The outer dimensions of the detector are an 8 mm diameter and a 25 mm length, with the sensitive volume lying 0.45 mm below the surface of the detector. This detector was also used in conjunction with the RFA 300 radiation field analyzer.

3.2.3 Film dosimetry

Despite being one of the oldest types of dosimeters, film presents certain advantages that make it, still today, one of the most widely used. Film is an integrating 2-dimensional dosimeter, which makes it particularly useful for irradiation geometries in which several beams are used, or in non static situations (such as treatment arcs, or dynamic wedges). Furthermore, its very high spatial resolution surpasses that of all other dosimetry techniques. There are, however, drawbacks involved with film dosimetry, such as its energy dependence, its sensitivity to ambient light, and its sensitivity to film processing conditions.

The two main components of radiographic film are: the radiographic emulsion and the film base. Photographic emulsion consists of microscopic silver halide crystals (silver bromide) dispersed in a gelatin matrix. The diameter of these crystals varies from 0.3 μm for slow, insensitive film, to 2 μm for faster, more sensitive film. The emulsion, usually between 10 and 25 μm thick, is coated on one or both sides of the film base, which is usually made of

polyester or cellulose acetate. To prevent abrasion of the surface, a thin layer (0.5 μm) of gelatin is often coated on the surface of the emulsion.[5] When the film is exposed to X rays, electrons in the halide are liberated, forming electron-hole pairs which diffuse through the crystal. The electrons are eventually captured at trapping centers in the crystal, which consist of crystal defects and impurity atoms. The positive holes usually diffuse until they are trapped by interstitial silver atoms, producing Ag^+ ions. The distribution of these positive silver ions within the emulsion is called the *latent image*. During the development phase, the latent image is converted into a visible image when grains that contain more than approximately four silver ions are completely reduced to metallic silver, causing local darkening of the film. Grains with less than four silver ions are eventually removed by the fixing solution, leaving the emulsion locally transparent.[10] Thus, the level of darkening of the film is directly related to the dose absorbed by the film.

The concentration of reduced silver grains in the developed image is determined by measuring the optical density (*OD*) of the film, which is given by:

$$OD = \log \frac{I_o}{I_t}, \qquad (3\text{-}1)$$

where OD is the optical density of the film,
I_o is the intensity of the light incident on the film, and
I_t is the intensity of the transmitted light.

The optical density of the film is then related to the absorbed dose via a density-dose calibration curve. Since the response of film depends on the physical characteristics of the film (grain size, grain concentration, etc.) and on the conditions under which the film is developed (temperature, duration, etc.), this calibration curve must be measured for every batch of film used and each set of development conditions.

In our experiments, Kodak X-Omat-V films (Kodak Inc, Rochester, N.Y., USA) were used. The optical densities of the films were measured using a laser He-Ne densitometer (Dupont LINX model #FD-2000), which uses a red light of wavelength 632.8 nm and a 100 μm aperture. The 12-bit (4096) grayscale images from the laser densitometer were mapped to 8-bit (256) grayscale images by NIH Image 1.59 (developed at the U.S. National Institutes of Health and available on the Internet at http://rsb.info.nih.gov/nih-image/), which was used to analyze the 2-D dose distributions recorded by the films. Thus, the calibration curve for the films used in this thesis, shown in FIGURE 3-4, is expressed in terms of pixel intensity vs. absorbed dose. This curve was obtained by irradiating pieces of radiographic film at a depth of 5 cm inside solid water (at the nominal SSD of 100 cm) using 10 MV photons from the Clinac-18. The response of the film to absorbed dose can be seen to be essentially linear for doses below 50 cGy.

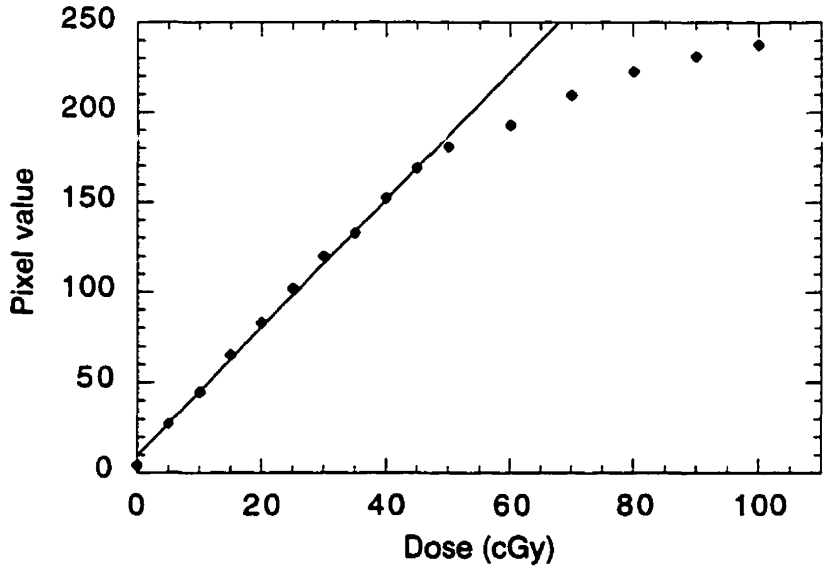

FIGURE 3-4 *Calibration curve for the radiographic films used in our experiments. The films were placed at a depth of 5 cm inside a solid water phantom (SSD=100 cm), and irradiated using 10 MV photons from the Clinac-18.*

3.2.4 Radiochromic film

Radiochromic film is a radiation dosimetry technique that is relatively new to the world of radiotherapy. Since its introduction in 1965, it has been extensively used for very high dose measurements, from 10^3 Gy to 10^6 Gy, such as those encountered in radiation sterilization of medical instruments and in food irradiation.[11] However, with the recent development of high sensitivity radiochromic film, the technique has found more and more applications in the field of radiation therapy.[12,13,14,15]

The emulsion of radiochromic film consists of a highly uniform (i.e., grainless) transparent coating which, through the process of dye polymerization, turns blue when exposed to ionizing radiation. This change in color occurs immediately upon exposure, and stabilizes approximately 24 hours later;[16] no film processing or developing are required. Furthermore, radiochromic film is relatively insensitive to ambient light, although exposure to ultraviolet light should be avoided.

High sensitivity radiochromic film presents several advantages over ordinary radiographic film. Because it need not be developed or processed, and because it can be manipulated at ambient light, it is much easier to use. Moreover, its response to radiation (i.e., its electron mass collisional stopping powers and photon mass-energy absorption coefficients) is very similar to that of water and muscle,[14] making radiochromic film a tissue equivalent dosimeter. Consequently, its response has relatively little energy dependence. Finally, whereas radiographic film starts to saturate at a dose of approximately 200 cGy, high sensitivity radiochromic film has a very large dynamic range and can be used for doses of up to several hundred Gy.[14]

The radiochromic films used in this work were Gafchromic MD-55 films, batch # 940818 (International Specialty Products, Wayne, NJ). The emulsion

layer is 23 μm thick, and is coated on a 100 μm thick polyester base. Just like radiographic film, a dose calibration curve must be performed for each batch of film used. Thus, small pieces of radiochromic film located at a depth of 5 cm inside a solid water phantom (SSD=100 cm) were irradiated to doses ranging from 0 Gy (background) to 100 Gy using 10 MV photons from the Clinac-18. After a waiting period of two days for the films to stabilize, the films were scanned using the laser He-Ne digitizer described in the previous section. The resulting calibration curve, displayed in FIGURE 3-5, shows that the response of the radiochromic film to absorbed dose was essentially linear for doses smaller than 50 Gy.

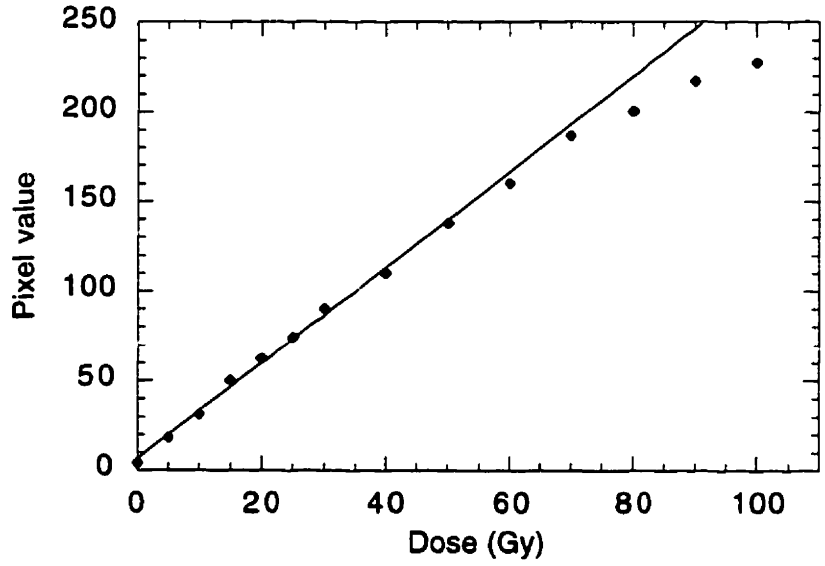

FIGURE 3-5 *Calibration curve for the radiochromic films used in our experiments. The films were placed at a depth of 5 cm inside a solid water phantom (SSD=100 cm), and irradiated using 10 MV photons from the Clinac-18 linear accelerator.*

3.2.5 BANG Gels

BANG gel is a tissue equivalent polymer gel dosimeter that records three dimensional dose distributions produced by ionizing radiation. Its name, BANG, is an acronym that describes the composition of the gel; it stands for bis, acrylamide, nitrogen and gelatin. BANG gel is made available solely through MGS Research Inc, Guilford CT.

The gels are made of acrylic monomers (acrylamide and N,N'-methylene-bisacrylamide) uniformly dispersed in an aqueous gel. Radiation produces localized polymerization and cross-linking of these monomers, causing an increase in the NMR relaxation rate of neighboring water protons.[17] Because the polymer molecules do not diffuse within the gel, these radiation induced changes are stable and do not change over time.[18] The spatial dose distributions recorded by the gels can be obtained by measuring the transverse relaxation rate (R_2) of the water protons, using MR imaging. The dose response of the gel (R_2 vs. dose) is linear until at least 5 Gy, and is independent of radiation quality, energy, and dose rate.[19] Even though batch variations of less than 2% are expected in the dose response curves,[17] a calibration curve for each gel batch should be measured prior to performing a quantitative analysis.

The gels used in this thesis were from lot # 021997. In order to measure the calibration curve, 12 small vials filled with gel were provided. These vials were placed at a depth of 8 cm inside a water phantom, and irradiated to doses of 0 (background), 1, 2, 3, 4, and 5 Gy using 10 MV photons from the Clinac-18. For each of the 6 calibration doses, two vials were irradiated. The gels were then imaged using a 64 Mhz, 1.5T GE Signa 5X MR imager (General Electric Medical Systems, Milwaukee, WI). Instead of an R_2 vs. dose calibration curve, a pixel intensity vs. dose calibration curve was done. Thus, the gels were imaged using a single spin echo pulse sequence, with a repetition time (TR) of 6000 ms and an echo time (TE) of 400 ms. All of the MRI images were analyzed using

NIH Image 1.59. The pixel intensity vs. absorbed dose calibration curve for the BANG gels used in this thesis is displayed in FIGURE 3-6. The experimental points were joined using a second degree polynomial curve fit.

The main advantage of BANG gels is that they can provide high resolution 3 dimensional dose distributions for complex irradiation geometries in a tissue equivalent material. Its spatial resolution is only limited by the resolution with which the gels can be imaged by the MRI scanner. Furthermore, since the optical properties of the gel change with radiation, the gels can also be used in a qualitative manner. Originally transparent, the gels become more and more opaque upon irradiation, ultimately becoming white when the saturation dose is reached. Care, however, must be taken in the manipulation of the gels. Since oxygen inhibits the free radical polymerization process, the

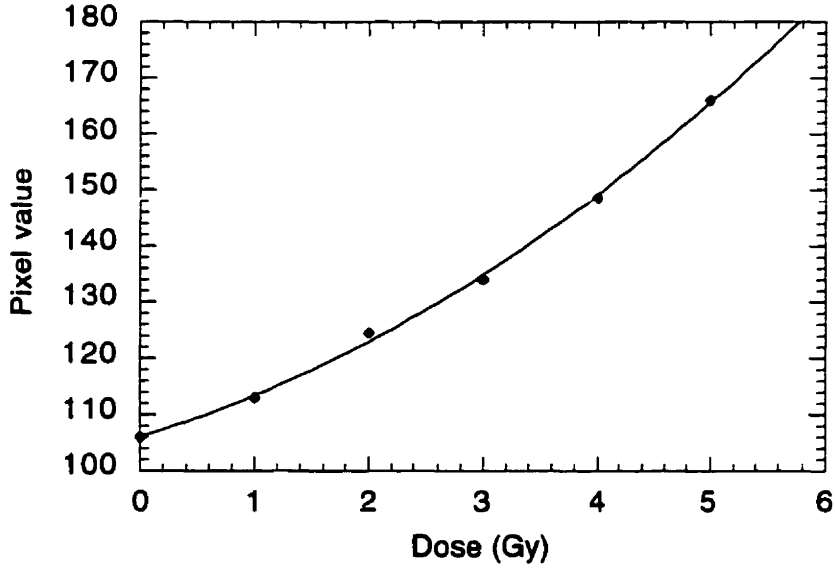

FIGURE 3-6 *Calibration curve for the BANG gels used in this thesis. The gels were placed at a depth of 8 cm inside a water phantom (SSD=100 cm) and irradiated using 10 MV photons from the Clinac-18. The gels were then imaged using a single spin echo pulse sequence with a repetition time (TR) of 6000 ms and an echo time (TE) of 400 ms. Experimental points were joined using a second degree polynomial curve fit.*

gels must be kept in an anoxic environment prior to irradiation. Furthermore, to prevent photopolymerization of the monomers, exposure to ambient light must also be avoided.

3.3 Phantoms

Several different phantoms (and phantom materials) were used in this thesis. For a material to be used as a phantom, it must have approximately the same radiation absorption and scattering properties as the medium in which the dose is to be delivered. If the medium in question is human tissue, then the phantom used for these measurements must approximate tissue, hence the name *tissue-equivalent phantom.* For photon energies such as those encountered in radiotherapy, the dose to tissue is mainly delivered through Compton interactions, which primarily depends on the number of electrons per unit volume (electron density ρ_e). The electron density ρ_e (in electrons/cm^3) of a material is simply the product of its mass density ρ_m (in g/cm^3) and its number of electrons per unit mass N_e (in electrons/g):

$$\rho_e\left(\frac{e^-}{cm^3}\right) = \rho_m\left(\frac{g}{cm^3}\right) \cdot N_e\left(\frac{e^-}{g}\right). \qquad (3\text{-}2)$$

As for the photoelectric effect and pair production, which both contribute to the absorbed dose but to a much lesser degree, they also depend on the atomic number Z of the material. Thus, for a phantom to be considered tissue equivalent, it must be made of a material having approximately the same mass density ρ_m, the same number of electrons per unit mass N_e, and the same effective atomic number Z_{eff} as human tissue. The physical properties of human tissue, along with several materials commonly used as phantoms for radiation dosimetry, are shown in TABLE 3-1.

	Mass density (g/cm^3)	Number of electrons / g ($\times 10^{23}$)	Z_{eff}
Muscle	1.04	3.31	7.64
Water	1.00	3.34	7.51
Polystyrene	1.05	3.24	5.74
Lucite	1.18	3.25	6.56
Solid water	1.00	3.34	7.34

TABLE 3-1 *Physical properties of human tissue (i.e., muscle) along with several materials commonly used as phantoms for radiation dosimetry. Data taken from Khan.*[4]

All of the radiographic film measurements along with the calibration curves for both radiographic and radiochromic film were carried out inside a solid water phantom (manufactured by RMI, Middleton, Wisconsin, USA). Solid water comes in 30x30 cm^2 square sheets, of thicknesses varying from 2 mm to 8 cm.

3.3.1 Radiation field analyzer water phantom

The radiation field analyzer (RFA-300, Scanditronix AB, Uppsala Sweden) water phantom consists of a Lucite water tank of inner volume 580 x 614 x 580 mm^3. Along with the water phantom comes a precision computer controlled servo mechanism which allows for complete 3-dimensional detector positioning, the detectors consisting of either diode detectors or thimble ionization chambers (as discussed previously). This allows for linear scans (the total scanning volume of the system is 495 x 495 x 495 mm^3) which enables the user to measure beam profiles, percentage depth doses and even 2-dimensional isodose distributions. In order to minimize the effects of fluctuations in the dose rate of the treatment unit (i.e., the Clinac-18 linear accelerator), the RFA-300 system is also equipped with dual electrometers, along with field and reference detectors. Thus, the signal measured by the radiation field detector can be divided by the signal measured by the reference

detector, keeping the ratio constant even when the machine output fluctuates. The positioning accuracy of the RFA-300 system is ± 0.5 mm with a positioning reproducibility of ± 0.1 mm.[20]

3.3.2 Stereotactic head phantom

Treatment planning verification was achieved using a stereotactic head phantom, built in-house. The phantom is made of a Lucite shell, in the form of a human head, with a cylindrical opening into which can be inserted one of two inserts: the *localization insert*, which contains an artificial target simulating a tumor, and the *verification insert*, which can contain radiochromic film in any of the three imaging planes (axial, coronal and sagittal). A picture of the head phantom, along with the various components comprising the localization insert and the verification insert, is shown in FIGURE 3-7.

The model used to create the head phantom was the Alderson Rando Anthropomorpic Phantom (Alderson Research Laboratories Inc., Stamford, CT, USA). A positive plaster mould of the head of the anthropomorphic phantom was first done in the departmental mould room. Through the process of vacuum forming, a rigid Lucite sheet of approximately 2 mm thickness was then formed to fit the contours of the plaster mould. Thus, the thickness of the phantom shell varies between 2 and 3 mm. A hollow Lucite cylinder of inner diameter 7.3 cm (and of 5 mm wall thickness) was then rigidly fixed inside the head phantom. The volume between the phantom shell and the cylindrical opening was sealed off at the base (neck) of the phantom so that it could subsequently be filled with water, thus making the phantom water-equivalent.

The localization insert consists of a hollow Lucite cylinder (outer diameter of 7.3 cm) having a wall thickness of 4 mm, at the top of which a target

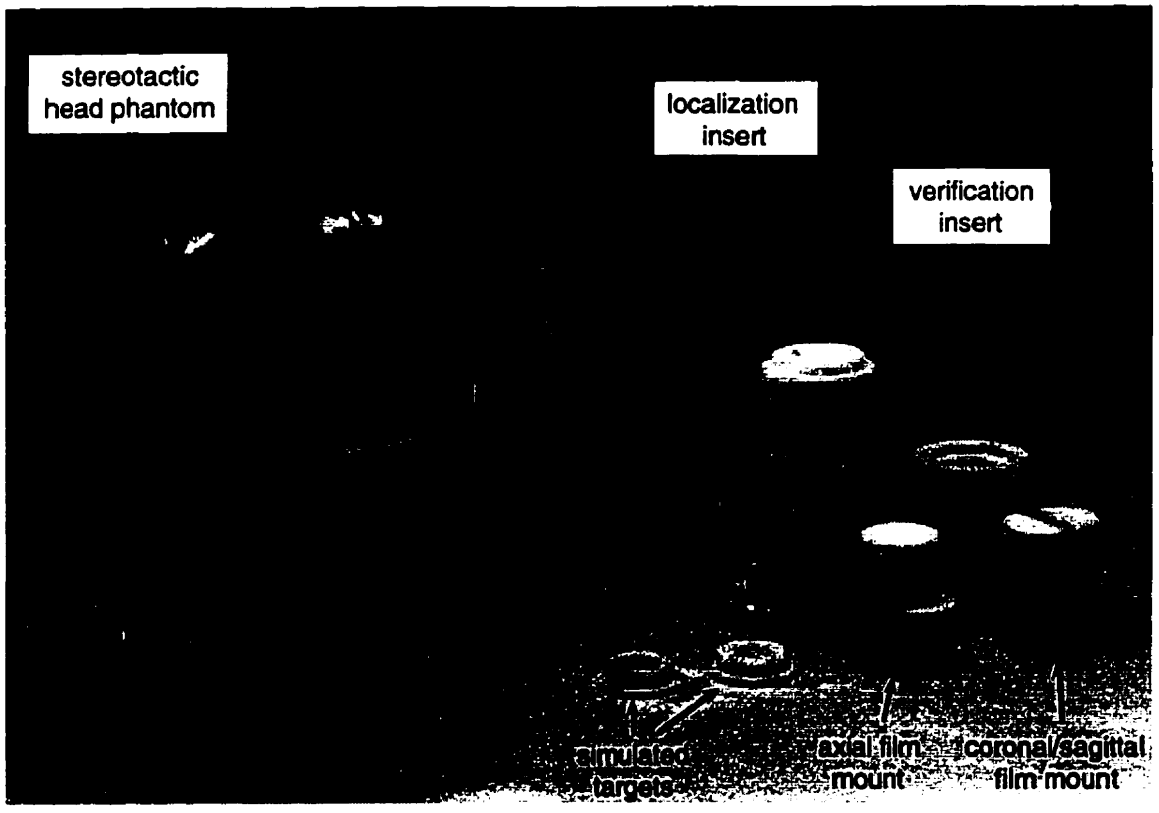

FIGURE 3-7 *Stereotactic head phantom with the various components of the localization insert and the verification insert.*

simulating a tumor can be fixed. While two different targets can be used with this insert (a spherical target and an irregularly shaped target), only the irregular target was used for the experiments described in this thesis. This irregular target (whose shape resembles that of a pear) is made of Lucite, has a length of 3 cm and a maximum width of approximately 2.4 cm. Once the target firmly in place, the localization insert is filled with water and inserted in the head phantom. The head phantom containing the simulated tumor is then ready to be imaged using CT or MRI.

The verification insert is made of three polystyrene pieces (two of which are clearly visible in FIGURE 3-7) that are assembled in such a way as to form a cylinder, the upper part of which is hollow and can contain one of two film

mounts: the axial film mount or the coronal/sagittal film mount. The axial film mount is made of two small polystyrene cylinders, each having a diameter of 4.8 cm and a height of 4 cm, which can contain a circular piece of radiochromic film with a maximum diameter of 4.8 cm. The coronal/sagittal film mount is made of two half cylinders between which can be sandwiched a rectangular piece of radiochromic film of maximum dimensions 4.8 cm by 8 cm. When assembled with their respective pieces of film, both film mounts make up a cylinder having a 4.8 cm diameter and a height of 8 cm. When the verification insert is inserted in the head phantom, the center of the film (for all three imaging planes) is located at the geometric center of the target.

3.4 Stereotactic frames

The stereotactic frame is an essential component of the radiosurgical process. Rigidly attached to the patient's skull (or to the stereotactic head phantom), it provides a fixed external coordinate system in which the 3-dimensional position of the target can be accurately determined. The stereotactic frame is also used for accurate positioning of the patient on the treatment machine and for patient immobilization during the delivery of the treatment. The frame used in this thesis was built in the machine shop of the Medical Physics department of the Montreal General Hospital. It uses a positive value coordinate system, with the origin (0,0,0) located at one of its corners, and the center of the frame volume having coordinates (10 cm,10 cm,10 cm). Its base is constructed of aluminum and plastic while its posts are made of carbon fiber. This is meant to provide maximum strength, while simultaneously minimizing CT and MR image artifacts and patient discomfort (due to the light weight of the frame).

For accurate target localization using computed tomography (CT) or magnetic resonance imaging (MRI), the stereotactic frame is fitted with a localizing attachment, which contains a set of reference (or fiducial) markers

whose position with respect to the frame is accurately known. In order for them to be clearly identified on the images, the reference markers of the localizing attachment are made of substances showing a strong signal from the imaging modality used. Thus, thin aluminum rods are used for CT, while a copper sulfate ($CuSO_4$) solution, contained in thin plastic tubes, is used for MRI. The stereotactic frame and the CT localizing attachment used in this thesis are shown in FIGURE 3-8.

The fiducial markers of the localizing attachment are arranged in several (3 for CT and 5 for MRI) "N"-shaped configurations, so that cross-sectional images of the brain will display sets of 3 collinear fiducial points. On any image, the outer fiducial markers set up a 2-dimensional coordinate system which can

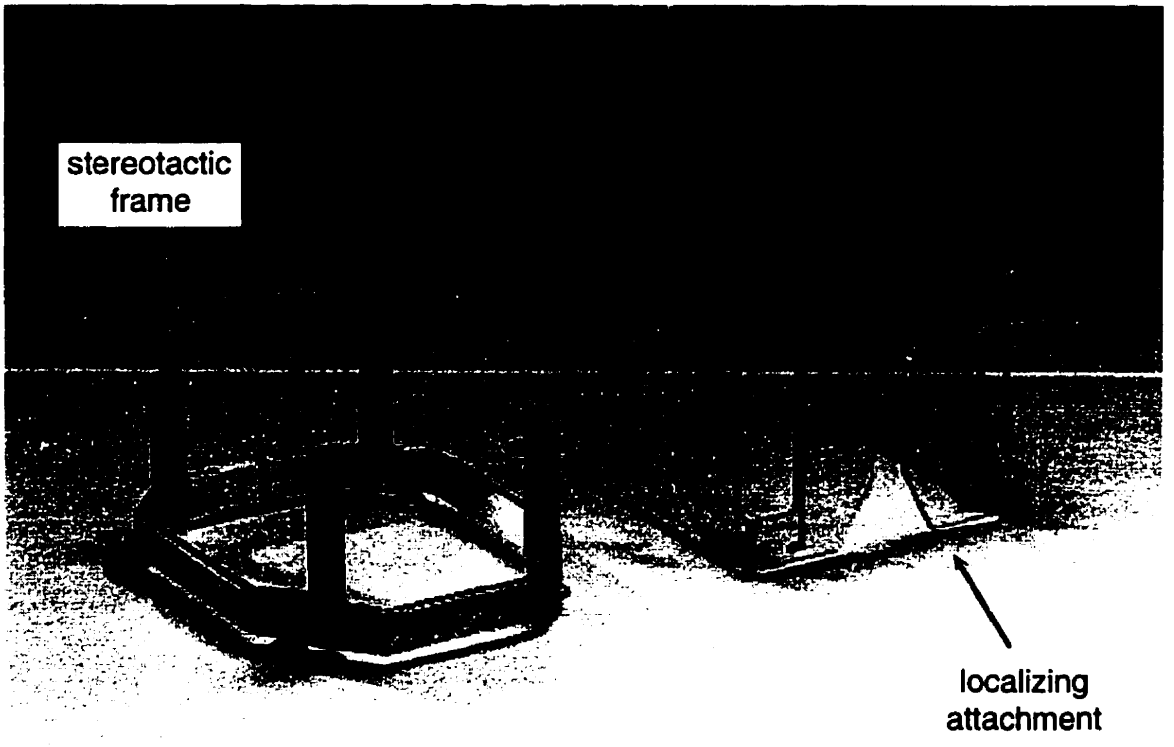

FIGURE 3-8 *Stereotactic frame and CT localizing attachment.*

describe any point within that image. As for the middle reference points, their position relative to the two outer markers determines the location of the imaging slice with respect to the stereotactic frame. Thus, the CT and MRI localizing attachments allow for the accurate determination of the 3-dimensional coordinates of any point within the stereotactic frame volume.

3.5 Custom-made radiosurgical collimators

Circular collimation of the Clinac-18 10 MV photons for the purpose of radiosurgery is achieved with a special collimation system that attaches to the accessory tray holder of the linac. The bottom of the tray holder is located at a distance of 65.1 cm from the source of radiation (i.e., 34.9 cm above the isocenter of the unit). This collimation system can hold one collimator insert which, in the case of dynamic stereotactic radiosurgery, consists of a 10 cm thick lead insert with a circular opening that is tapered to match the divergence of the radiation beam. To cover a wide range of target sizes, several of these inserts were constructed, each with a different sized opening in order to produce, at the isocenter, circular fields of diameters ranging between 0.50 cm to 4.00 cm, in steps of 0.25 cm.

For stereotactic radiosurgery with static conformal fields, the same secondary collimator assembly is used, except that the circular inserts are replaced with custom-made inserts. Our method of manufacturing these custom-made collimator inserts is similar to the one described by Bourland and McCollough.[21] The bulk of the inserts is made of CadFree 95 (manufactured by Aim Products Inc), which is a low melting-point alloy (melting point = 95 °C) made of bismuth (52%), lead (32%) and tin (16%). This low melting-point alloy is poured into an aluminum carrier sleeve into which a styrofoam cutout representing the shape of the field was previously centered. For every beam, a magnified beam's eye view (BEV) of the field is printed and is used as a template for the cutting of the styrofoam piece around which the alloy will be

poured (FIGURE 3-9). The block of styrofoam is located at the same distance from the simulated source as the custom-made collimators will be from the radiation source. The BEV template is placed on the table and centered on the cross-hair, the line joining the simulated source and the center of the cross-hair representing the central axis of the radiation beam. A mechanical pointer, to which a hot wire is attached, is used to trace out the BEV template. As the pointer traces out the template, the hot wire cuts through the styrofoam block, thus producing a positive styrofoam mould of the collimator aperture. Properly scaled BEV templates of the field are then used to center the styrofoam

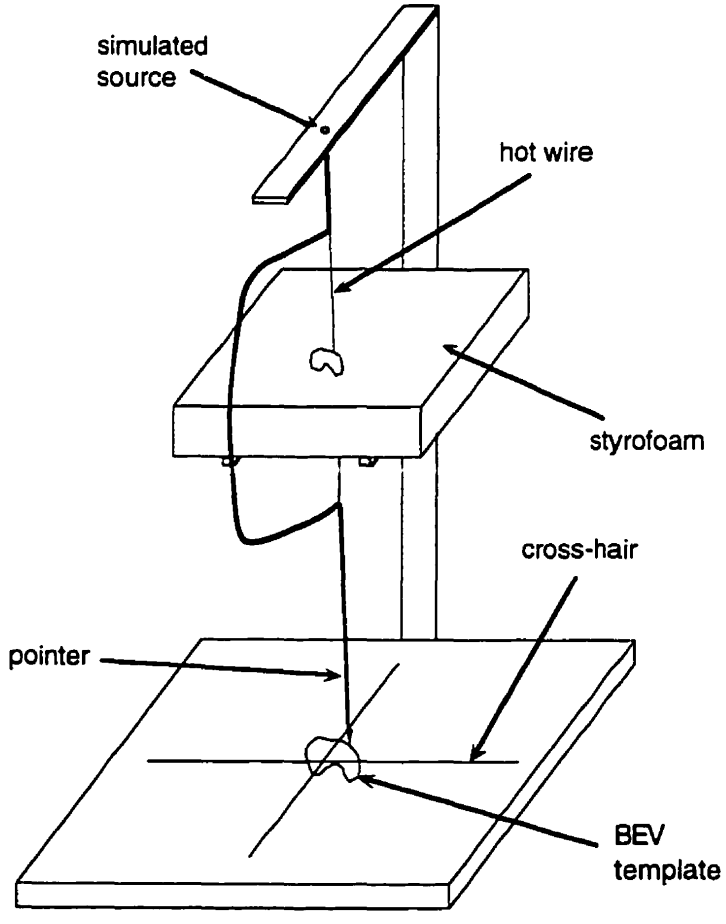

FIGURE 3-9 *Schematic representation of the geometry used to produce the styrofoam cutouts.*

cutout inside the aluminum sleeve. Once centered, they are clamped together and the alloy is poured inside the sleeve (FIGURE 3-10). The resulting collimator insert, which is approximately 10 cm thick, has a block transmission value of approximately 1.5% for the 10 MV photons from the Clinac-18. Because they are easily separated, both the aluminum sleeve and the alloy can be recovered for reuse after the radiosurgical procedure is done.

Ideally, the shape of each field would conform to the projection (i.e., BEV) of the target, plus a 2 mm margin to account for beam penumbra. However, due to the uncertainties involved with the fabrication of the custom collimators (cutting of styrofoam pieces, alignment of styrofoam cutouts inside the aluminum sleeve, etc.), this margin usually varies between 1 and 3 mm. The shape of the irregular fields are therefore accurate to within ± 1 mm.

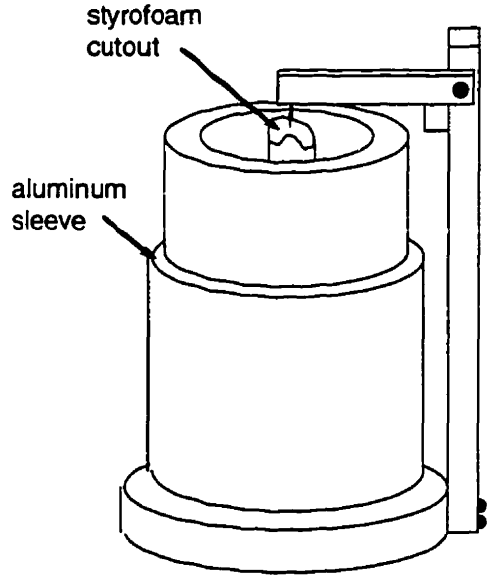

FIGURE 3-10 *Using properly scaled BEV templates of the field, the styrofoam cutout is centered inside the aluminum sleeve. Once centered, the styrofoam cutout and the aluminum sleeve are clamped together, and the melted alloy is poured inside the aluminum sleeve.*

3.6 Summary

In this chapter, the experimental apparatus and techniques used for this thesis were described. A brief overview of medical linear accelerators was first given, with an emphasis on the Clinac-18 linear accelerator, which is used for radiosurgery here at McGill University. A description of the various dosimetry techniques used to measure the dose was then presented, along with the calibration curves for radiographic film, radiochromic film, and BANG gels. The different phantoms in which the dose was measured were also described, as were the stereotactic frame and the localizing attachments used in conjunction with the stereotactic head phantom. Finally, our method for manufacturing the custom-made radiosurgical collimators was presented.

3.7 References

[1] E. Persico, E Ferrari and S.E. Segre, **Principles of particle accelerator**, Chap. 8, W.A. Benjamin Inc., New York, 1968.

[2] C.J. Karzmark and R.J. Morton, **A primer on theory and operation of linear accelerators in radiation physics**, Bureau of Radiological Health, FDA 82-8181, Dec. 1981.

[3] C.J. Karzmark, **Advances in linear accelerator design for radio-therapy**, Med. Phys. **11**: 105-128 (1984).

[4] F.M. Khan, **The Physics of Radiation Therapy**, 2nd Ed., Williams & Wilkins, Baltimore MD, 1984.

[5] C. Zankowski, **Monte Carlo analysis of the 10 MV X-ray beam from a Clinac-18 linear accelerator**, Msc. Thesis, McGill University, Montreal (1994).

[6] F.H. Attix, W.C. Roesch and E. Tochilin, **Radiation Dosimetry Volume II**, 2nd Ed., Academic Press, New York, 1966.

[7] M.E.J. Young, **Radiological Physics**, 3rd Ed., London H.K. Lewis & Co. Ltd., London, 1983.

[8] N.W. Ashcroft, **Solid State Physics**, International Ed., Holt, Rinehart & Winston, 1979.

[9] F.H. Attix, **Introduction to Radiological Physics and Radiation Dosimetry**, John Wiley & Sons, New York, 1986

[10] M.M. Ter-Pogossian, **The physical basis of diagnostic radiology**, Harper & Row, New York, 1967.

[11] P.J. Muench, A.S. Meigooni, R. Nath and W.L. McLaughlin, **Photon energy dependence of the sensitivity of radiochromic film and comparison with silver halide film and LiF TLDs used for brachytherapy dosimetry**, Med. Phys. **18**: 769-775 (1991).

[12] J.A. Sayeg and R.C. Gregory, **A new method for characterizing beta-ray ophtalmic applicator sources**, Med. Phys. **18**: 453-461 (1991).

[13] R. Ramani, A.W. Lightstone, D.L.D. Mason and P.F. O'Brien, **The use of radiochromic film in treatment verification of dynamic stereotactic radiosurgery**, Med. Phys. **21**: 389-392 (1994).

[14] W.L. McLaughlin, C.G. Soares, J.A. Sayeg, E.C. McCullough, R.W. Kline, A. Wu and A.H. Maitz, **The use of radiochromic detector for the determination of stereotactic radiosurgery dose characteristics**, Med. Phys. **21**: 379-388 (1994).

[15] S. Chiu-Tsao, A. de la Zerda, J. Lin and J.H. Kim, **High-sensitivity GafChromic film dosimetry for ^{125}I seed**, Med. Phys. **21**: 651-657 (1994).

[16] W.L. McLaughlin, C. Yun-Dong, C.G. Soares, A. Miller, G. Van Dyk and D.F. Lewis, **Sensitometry of the response of a new radiochromic film dosimeter to gamma and electron beams**, Nucl. Instrum. Methods Phys. Res. A **302**: 165-176 (1991).

[17] M.J. Maryanski, R.J. Schultz, G.S. Ibbott, J. Xie, D. Horton and J.C. Gore, **Magnetic resonance imaging of radiation dose distributions using a polymer-gel dosimeter**, Phys. Med. Biol. **39**: 1437-1455 (1994).

[18] M.J. Maryanski, J.C Gore, R.P. Kennan and R.J. Schultz, **NMR relaxation enhancement in gels polymerized and cross-linked by ionizing radiation: a new approach to 3D dosimetry by MRI**, Magn. Res. Imag. **11**: 253-258 (1993).

[19] M.J. Maryanski, G.S. Ibbott, P. Eastman, R.J. Schultz and J.C. Gore, **Radiation therapy dosimetry using magnetic resonance imaging of polymer gels**, Med. Phys. **23**: 699-705 (1996).

[20] RFA 300 radiation field analyzer, operation manual (Scanditronix AB, Uppsala, Sweden, 1992).

[21] J.D. Bourland and K.P. McCollough, **Static field conformal stereotactic radiosurgery**, Int. J. Radiat. Oncol. Biol. Phys. **28**: 471-47 (1993).

Chapter 4

Treatment planning for small irregular fields

4.1 Introduction

In this thesis, two different treatment planning systems were used to calculate radiosurgical dose distributions; the McGill Planning System (MPS), developed in-house, and the commercial *CADPLAN* Treatment Planning System version 2.7 (from here-on referred to as *CADPLAN*). Both systems are based on the Milan and Bentley algorithm,[1] expanded from the original two-dimensional approach to three dimensions. The MPS was used to devise radiosurgical treatment plans using the dynamic radiosurgery technique, while *CADPLAN* was used for treatment plans using static conformal fields.

The McGill Planning System (MPS) is a locally developed three dimensional treatment planning system which is used clinically at McGill University for the planning of stereotactic radiosurgery procedures. It is a Macintosh based system (thus making use of the Macintosh user interface) which has evolved from the dose calculation system developed by Pike *et al* .[2] The McGill Planning System was verified experimentally and has been previously described in detail.[3]

CADPLAN is a CT-based, three dimensional treatment planning system offered commercially by Varian Associates (Palo Alto, California). The accuracy of *CADPLAN* has recently been verified for a wide range of beam geometries covering most standard clinical situations.[4] The use of static conformal fields as a means of performing radiosurgery, however, is a rather complex technique and represents a challenge to most treatment planning systems, mainly because of the small sizes of the irregular fields involved. Thus, prior to using *CADPLAN* for the treatment planning of radiosurgical procedures using fixed shaped beams, its accuracy had to be verified.

4.2 CADPLAN's external photon beam modeling

The information concerning the calculation algorithms used by *CADPLAN* were obtained from the *CADPLAN* external beam modeling reference manual.[5] *CADPLAN's* external photon beam modeling uses two models; the beam reconstruction model and the patient model. For a given beam geometry, *CADPLAN* first uses the beam reconstruction model to calculate the dose distribution in a water equivalent phantom, assuming normal incidence and flat surface. This dose distribution is then appropriately modified by the patient model to take into account tissue inhomogeneities and skin curvature. Thus the dose D at any given point Q is given by (FIGURE 4-1):

$$D_Q = PDD(d', A, SSD) \cdot OAR(d', x, y) \cdot C_o \cdot C_i \,, \qquad (4\text{-}1)$$

where $PDD(d',A,SSD)$ is the central axis percentage depth dose for source-skin distance SSD, depth in phantom d', and field size A,

$OAR(d',x,y)$ is the off-axis ratio for a point located at depth d' in phantom and off-axis positions x and y,

C_o is the skin obliquity correction factor, and

C_i is the tissue inhomogeneity correction factor.

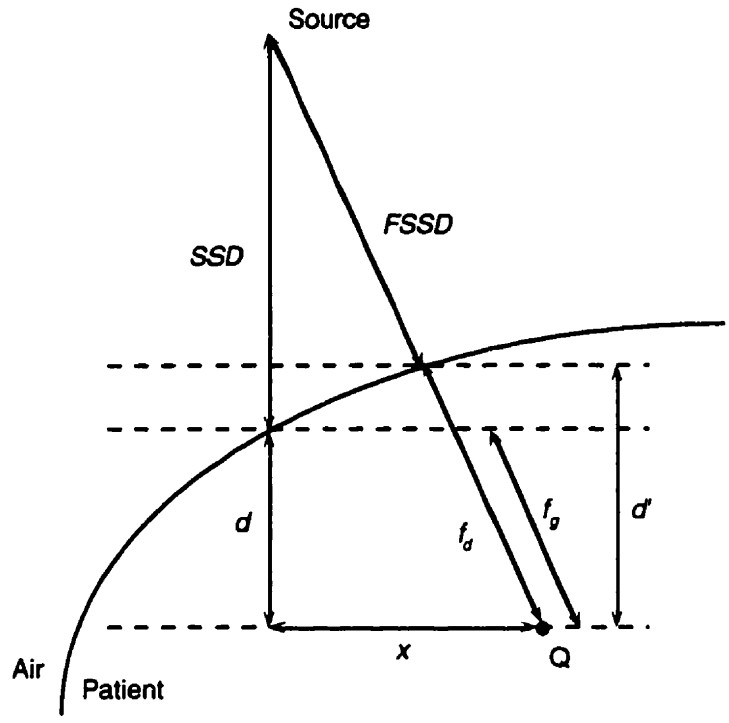

FIGURE 4-1 *Geometrical definitions of the variables used in CADPLAN's calculation algorithms.*

The values for the *PDDs* and the *OARs* in eq. 4-1 are calculated using the beam reconstruction model, while the skin obliquity correction factor C_o and the tissue inhomogeneity correction factor C_i are calculated using the patient model.

4.2.1 Beam reconstruction model

For a given beam geometry, the beam reconstruction model calculates the dose distribution in a water equivalent phantom assuming normal beam incidence and a flat phantom surface. Thus, in this model, the dose D at any point Q is simply given by the product of a depth dose value and an off-axis ratio:

$$D_Q = PDD(d,A,SSD) \cdot OAR(d,x,y) \ , \qquad (4\text{-}2)$$

where *PDD(d,A,SSD)* is the central axis percentage depth dose for depth *d*, source-skin distance *SSD* and field size *A*, and

OAR(d,x,y) is the off-axis ratio of a point located at depth *d*, with off-axis positions *x* and *y*.

Depending on the irradiation geometry, the beam reconstruction model used will either be the *regular photon beam model* or the *pencil beam model*. The *regular photon beam model* is used exclusively to calculate dose distributions for rectangular fields, while the *pencil beam model* calculates dose distributions for irregularly shaped fields.

A. Regular photon beam model

As previously mentioned, the regular photon beam model is used in cases involving rectangular (symmetrical or asymmetrical) fields of size $F_x \cdot F_y$. In this model, the measured beam data required by *CADPLAN* are the central axis *PDDs* along with the beam profiles through central axis at five configuration depths, for regular square fields. This data is to be measured at the configuration source-phantom distance of *SPD*. In order to distinguish them from calculated quantities, all measured quantities will be denoted by the subscript "m".

a) Calculation of *PDDs*

If the source-skin distance *SSD* is equal to the source-phantom distance of configuration *SPD*, then the value of the *PDD* in eq. 4-2 is simply equal to the measured value of the *PDD* for the equivalent square field of area A_{eq}:

$$PDD(d,F_x \cdot F_y,SSD) = PDD_m(d,A_{eq},SPD) \ , \qquad (4\text{-}3)$$

where $\sqrt{A_{eq}}$ is calculated from F_x and F_y using Sterling's approximation, and

PDD_m is the measured central axis percentage depth dose for the square field of size A_{eq} . If, however, the source-skin distance *SSD* differs from the configuration *SPD* (as is the case for isocentric set-ups), then the depth doses must be modified appropriately. This is accomplished by the following correction factor, which consists of the Mayneord factor and a *TAR* or *TPR* ratio:

$$CF_{SSD}(\mathrm{d}) = \frac{T(d,A_2)}{T(d,A_1)} \cdot \left(\frac{SSD+d_{\max}}{SSD+d}\right)^2 \cdot \left(\frac{SPD+d}{SPD+d_{\max}}\right)^2, \qquad (4\text{-}4)$$

where $$A_1 = \left(\frac{\mathrm{SPD}+\mathrm{d}}{\mathrm{SPD}}\right) \cdot \mathrm{A_{eq}} \qquad A_2 = \left(\frac{\mathrm{SSD}+\mathrm{d}}{SSD}\right) \cdot A_{eq}, \qquad (4\text{-}5)$$

$T(d,A_i)$ is the *TAR* or *TPR* value, calculated at depth d for field size A_i from the measured *PDD* data, and

d_{max} is the depth of dose maximum.

Finally, since *CADPLAN* normalizes the dose to 100% at d_{max} for a source-skin distance equal to *SPD*, an additional normalization factor CF_{inv} is introduced:

$$CF_{inv} = \left(\frac{SPD+d_{\max}}{SSD+d_{\max}}\right)^2. \qquad (4\text{-}6)$$

The resulting percentage depth dose is therefore given by:

$$PDD(d,F_x,F_y,SSD) = PDD_m(d,A_{eq},SPD) \cdot CF_{SSD}(d) \cdot CF_{inv}, \qquad (4\text{-}7)$$

where PDD_m is the measured central axis percentage depth dose for depth d, equivalent field size A_{eq} , and source-phantom distance *SPD* ; CF_{SSD} is the correction factor that accounts for a change in *SSD* (given by eq. 4-4); and CF_{inv} is the inverse square law normalization factor (given by eq. 4-6).

b) Calculation of *OARs*

The off-axis ratio in eq. 4-2 is obtained by multiplying the boundary profile with the envelope profile according to:

$$OAR(d,x,y) = P_b(d,x,F_x) \cdot P_b(d,y,F_y) \cdot P_e(d,r)\,, \qquad (4\text{-}8)$$

where $P_b(d,x,F_x)$ is the value of the boundary profile for a point located at a depth of d and a distance x from the beam central axis, with a field size in the x direction of F_x,

$P_e(d,r)$ is the value of the envelope profile at depth d and radial distance r from the central axis, and

$r = (x^2+y^2)^{1/2}$.

Both the envelope and the boundary profiles are calculated from the measured beam profiles at the five configuration depths. The envelope profile $P_e(d,x)$, which represents the profile of an infinite, uncollimated beam, is essentially an average of the measured beam profiles:

$$P_e(d,x) = \frac{1}{(N-n+1)} \sum_{i=n}^{N} P_m(d,x,F_{xi}^2)\,, \qquad (4\text{-}9)$$

where P_m are the measured beam profiles, N is the total number of beam profiles measured, and n is a starting index which ensures that, for each x position where the envelope profile is to be calculated, the fields that are too small to enclose this point are excluded from the calculation. The boundary profile $P_b(d,x,F_x)$, which describes the beam profile at the boundary of the collimating jaws, is simply equal to the measured beam profile divided by the envelope profile:

$$P_b(d,x,F_x) = \frac{P_m(d,x,F_x^2)}{P_e(d,x)}\,. \qquad (4\text{-}10)$$

B. Photon pencil beam model

The photon pencil beam model is used to calculate dose distributions for beam geometries involving irregularly shaped fields, denoted by A_{irr}. In this

model, pencil beam kernels are convolved with a field function *F(x,y)* to yield the proper *PDDs* and *OARs*. In addition to the central axis *PDDs* and beam profiles through central axis at five different configuration depths, *CADPLAN's* photon pencil beam model also requires the measured *PSFs* for regular square fields.

The calculation of the *PDDs* is based on the convolution of the field function *F(x,y)* with the scatter kernel $K_s(d,x,y)$, which is computed from the measured *PDDs* and *PSFs*. The calculation of the *OARs* is based on the convolution of *F(x,y)* with the boundary kernel $K_b(d,x,y)$, which is computed from the measured beam profiles.

The field function *F(x,y)* is defined by dividing the irregular field into a matrix of square elements, and assigning a value to each of the elements. This value, which reflects the intensity of the beam inside the square element, is equal to 1 if the element lies in the open part of the beam; 0 if it is under the collimating jaws; the block transmission value if it is under the block; and the ratio of its open surface to its total surface if it is located at the boundary of the field. Depending on the desired resolution, the dimension of the square elements may be 0.25 cm, 0.5 cm or 1 cm. Reducing the size of the grid increases the accuracy of the calculation, but also increases the time required to perform the calculation.

a) Calculation of *PDDs*

In the photon pencil beam model, the *PDDs* are given by:

$$PDD(d,A_{irr},SSD) = PDD_m(d,A_e,SPD)\cdot CF_{SSD}(d)\cdot CF_{inv}\cdot CF_{irr}(d)\,, \quad (4\text{-}11)$$

where CF_{SSD} and CF_{inv} have been defined above as the factor that accounts for a change in *SSD* (eq. 4-4) and the inverse square law normalization factor (eq. 4-6), respectively, and CF_{irr} is the factor that corrects for the irregular shape of the field.

To obtain the irregular field correction factor CF_{irr}, the field function $F(x,y)$ is first convolved with the scatter kernel $K_s(d,x,y)$ at all five configuration depths, resulting in dose distributions in five planes perpendicular to the beam central axis. These dose distributions are for an infinite source-skin distance and are normalized to d_{max} for a 10x10 cm^2 field:

$$D(d_i,x,y,A_{irr},\infty) = K_s(d_i,x,y)*F(x,y)\ . \qquad (4\text{-}12)$$

To relate the dose at an infinite source-skin distance to the dose at a source-surface distance of *SPD*, an inverse square factor is used:

$$D(d_i,x,y,A_{irr},SPD) = D(d_i,x,y,A_{irr},\infty)\cdot\left(\frac{SPD+d_{\max}}{SPD+d_i}\right)^2 . \qquad (4\text{-}13)$$

A regular square field of size A_{eq} equivalent to the irregular field A_{irr} is then determined by matching their depth doses at median configuration depth d_3, which, in the case of the irregular field, is given by:[5]

$$\begin{aligned} PDD(d_3,A_{irr},SPD) &= D(d_3,x_m,y_m,A_{irr},SPD) \\ &= D(d_3,x_m,y_m,A_{irr},\infty)\cdot\left(\frac{SPD+d_{\max}}{SPD+d_3}\right)^2 , \end{aligned} \qquad (4\text{-}14)$$

where (x_m,y_m) is the point, in the plane at depth d_3, where the dose is at its maximum value.

A first correction factor $C(d)$, calculated by linear interpolation between the values of $PDD(d_i,A_{irr},SPD)\ /\ PDD_m(d_i,A_{eq},SPD)$ for the five configuration depths, is applied to the measured central axis percentage depth doses of the equivalent square field A_{eq}. A second correction factor normalizes the percentage depth doses of the irregular field A_{irr} to the dose at d_{max} of the unblocked rectangular field, so that the resulting irregular field correction factor CF_{irr} is given by:

$$CF_{irr}(d) = C(d) \cdot \frac{PSF(A_{eq})}{PSF(A_{col})}, \qquad (4\text{-}15)$$

where A_{col} is the size of the unblocked field, determined by the position of the collimating jaws.

b) Calculation of *OARs*

For the *OAR* calculation, the boundary kernel $K_b(d,x,y)$ is convolved with the field function $F(x,y)$ to give a 2-D boundary profile:

$$P_b(d,x,y,A_{irr}) = K_b(d,x,y) * F(x,y) . \qquad (4\text{-}16)$$

This 2-D boundary profile is then multiplied with the envelope profile to give the proper *OAR* :

$$OAR(d,x,y) = P_e(d,r) \cdot P_b(d,x,y,A_{irr}) . \qquad (4\text{-}17)$$

4.2.2 Patient model

In the patient model, we are mainly concerned with the skin obliquity correction factor C_o . Because stereotactic radiosurgery is a brain irradiation technique, tissue inhomogeneities within the irradiated volume (which are rather small) will have a negligible effect on the dose calculations. Therefore, during all of the dose calculations made by *CADPLAN,* the inhomogeneity correction factor was not used.

The correction for skin obliquity, which is performed using the inverse square law and the *TAR* or *TPR* ratio, is done along a diverging fanline between the calculation point Q and the radiation source (FIGURE 4-1):

$$C_o = \left(\frac{SSD + f_d}{SSD + f_g} \right)^2 \cdot \left[\frac{T(f_d, A_2)}{T(f_d, A_1)} \right], \qquad (4\text{-}18)$$

where $A_1 = \left(\frac{SSD + f_d}{SSD}\right) \cdot A$ and $A_2 = \left(\frac{FSSD + f_d}{FSSD}\right) \cdot A$,

SSD is the central axis source-surface distance,

$FSSD$ is the source-surface distance along the diverging fanline,

f_d is the distance, along the fanline, between point Q and the surface of the patient, and

f_g is the distance, along the fanline, between point Q and a line perpendicular to the beam central axis where the surface of the patient and the central axis intersect.

4.3 *Accuracy of CADPLAN for small irregular fields*

In order to verify the accuracy of *CADPLAN,* custom-made collimators defining three small irregular fields were built according to the method described in section 3.5. The outlines of the three beams, taken at a source-axis distance of 100 cm, are displayed in FIGURE 4-2. These three fields were used to irradiate either a solid water phantom (in the case of radiographic film measurements) or the RFA water phantom (in the case of diode measurements). An isocentric set-up was used (SAD = 100 cm), with the isocenter located at a depth of 8 cm below the surface of the phantom. Dose profiles in planes perpendicular to the beam central axis and depth doses in planes parallel to the beam central axis were then measured. The location of these dose measurements with respect to the central axis of the radiation beam can be seen in FIGURE 4-2. The shaded lines represent dose profiles measured at three different depths in the phantom: 2.5 cm, 5 cm and 10 cm. The crosses (+) represent depth doses that were measured parallel to the beam central axis, from a depth of 2.5 cm to a depth of 15 cm. The results of these dose measurements were then compared with the dose distributions obtained from *CADPLAN* using the 2.5 mm calculation grid, which is the smallest one available.

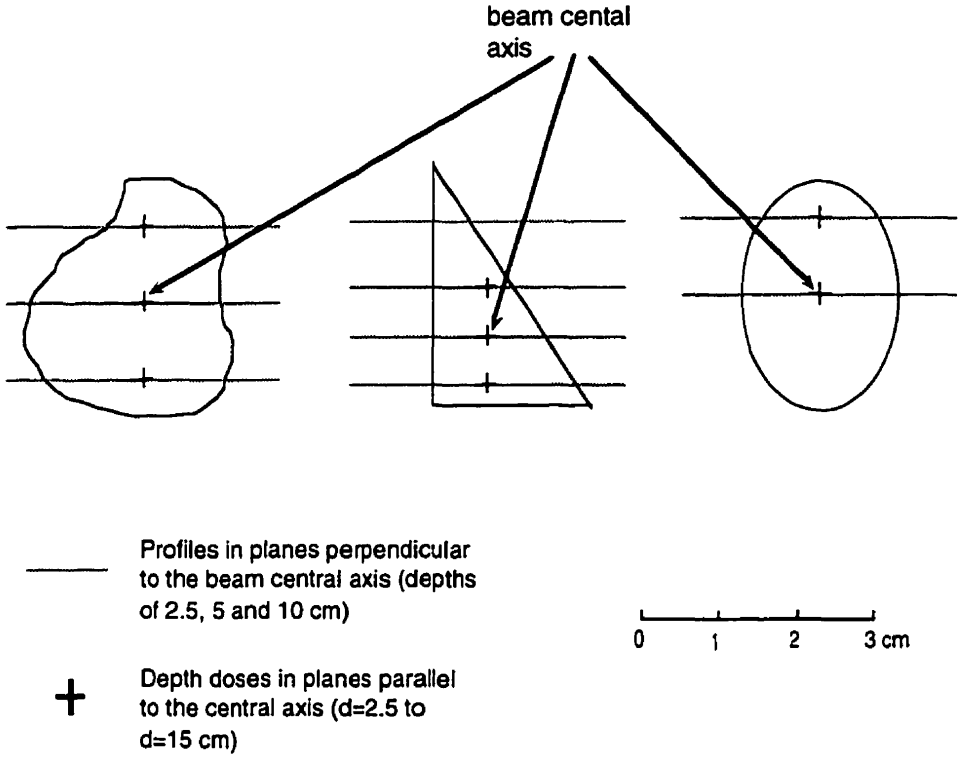

FIGURE 4-2 *Shape of the irregular fields used to verify the accuracy of CADPLAN. These beam outlines were taken at a source-axis distance SAD of 100 cm. The shaded lines represent dose profiles measured in planes perpendicular to the beam central axis while the crosses represent depth doses measured parallel to the beam central axis. The dose measurements were taken inside a water or solid water phantom, which was isocentrically positioned (SAD = 100 cm) so that the isocenter was at a depth of 8 cm inside the phantom.*

FIGURE 4-3 provides a comparison between relative doses calculated by *CADPLAN* and relative doses measured experimentally. All dose values were normalized to 100% at a depth of 2.5 cm on the beam central axis. While shown for one field only (FIGURE 4-3 (A)), these results are representative of the results obtained with all three irregularly shaped fields. By examining the profiles through the central axis in FIGURE 4-3 (C), it can be seen that, at an offset position of 0 (i.e., on the beam central axis), the relative dose values calculated by *CADPLAN* are in good agreement with those measured experimentally. This agreement, however, starts to break down as the distance from the central axis increases; the dose profiles calculated by *CADPLAN* start dropping off too early, resulting in an underestimation of the dose at the edges

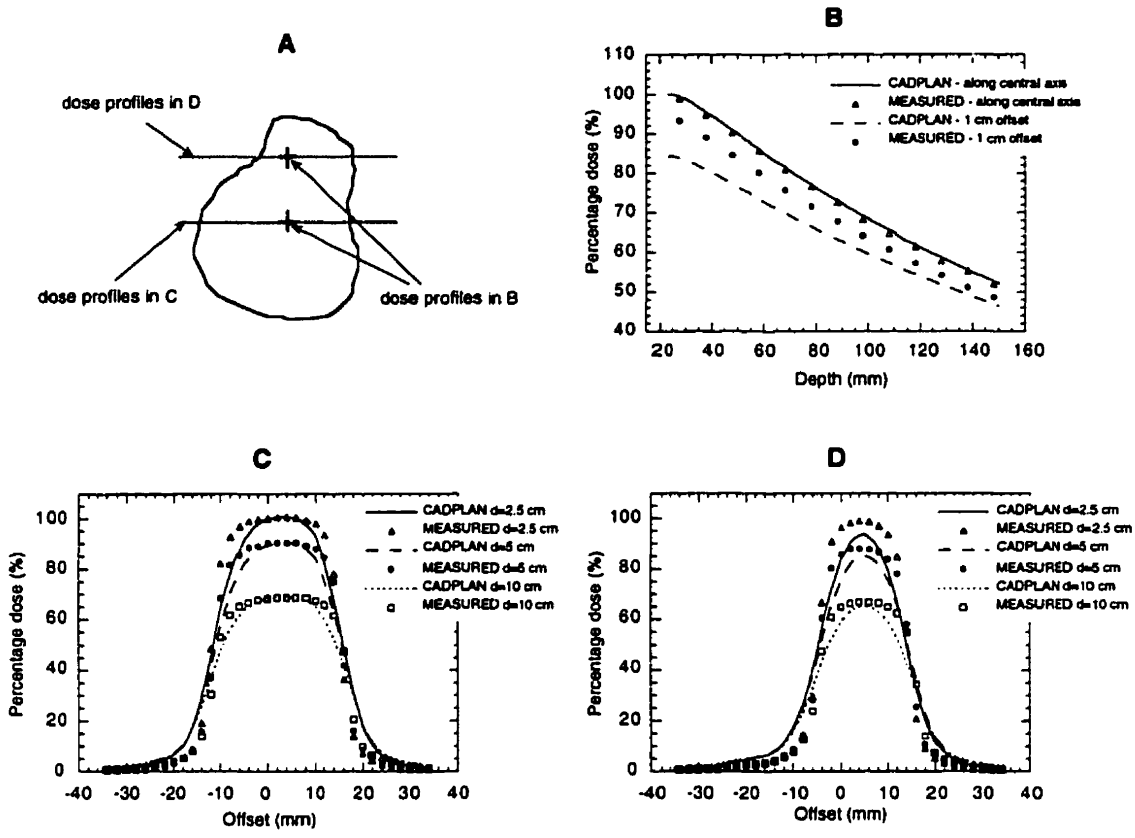

FIGURE 4-3 *Qualitative comparison between relative doses calculated by CADPLAN and relative doses measured experimentally. Part* ***A*** *indicates where the dose profiles were taken. Depth doses taken parallel to the beam central axis are shown in* ***B****, while dose profiles in planes perpendicular to the beam central axis are shown in* ***C*** *(profiles through central axis) and* ***D*** *(profiles 1 cm from central axis).*

of the radiation beam. This can also be seen in FIGURE 4-3 (B), in which a comparison of depth doses taken parallel to the beam central axis is shown. At an offset position of 0 (i.e., along the beam central axis), the agreement between the measured and calculated dose values is excellent. At an offset of 1 cm, however, the relative doses calculated by *CADPLAN* are consistently lower than those measured experimentally, with an absolute error between dose values of approximately 10% at a depth of 2.5 cm. This error generally decreases with increasing depth, reaching a value of approximately 2% at a depth of 15 cm. Dose profiles taken 1 cm off-axis in planes perpendicular to the

beam central axis are shown in FIGURE 4-3 (D). These profiles simply confirm what was pointed out from the two previous graphs: the measured dose received by points closer to the edge of the radiation field is larger than the dose predicted by *CADPLAN* .

4.4 Alternate beam configuration

Even though only a qualitative comparison between measured and calculated dose values was done, it is quite clear that *CADPLAN's* external photon beam modeling does not produce accurate results when used for small irregular fields. As was seen in section 4.21, the dose at any given point in the phantom is given by the product of a depth dose value and an off-axis ratio (eq. 4-2). The excellent agreement between the measured and calculated dose values for depth doses along the beam central axis indicates that *CADPLAN* correctly calculates the *PDDs.* Thus, the error in relative dose values to points located off central axis is due to an error in the calculation of the *OARs.* In the case of irregularly shaped fields, the calculation of the *OARs* is based on the convolution of the boundary kernel $K_b(d,x,y)$ with the field function $F(x,y)$, which is obtained by dividing the irregular field into a regular matrix of square elements (of side 2.5 mm), and assigning a value to each of these elements according to their position in the beam (FIGURE 4-4 (A)). The problem with small irregular fields arises at the edges of the radiation beam, which are not properly modeled by the field function. Square elements at the edges of the field are assigned a value equal to the ratio of their open surface to their total surface. Thus, the very sharp beam intensity gradient at the edge of the radiation field (the sudden drop from 1 to the block transmission value) is spread out over a distance equal to the width of a square element by the field function. This does not cause a problem in most clinical situations involving irregularly shaped fields, for which a 2.5 mm calculation grid provides adequate resolution. However, for small fields such as those used in radiosurgery, which are typically

between 2 and 3 cm, the field function spreads out the drop in beam intensity at the edge of the field over a distance which represents approximately 10% of the total field size (i.e., 2.5 mm). Due to this poor resolution, the edges of the radiation beam are not properly modeled by the field function *F(x,y)*, thus resulting in non-negligible errors in the calculated dose as the distance from the central axis increases. In order to obtain more accurate results, the resolution with which the field function *F(x,y)* models the radiation beam must therefore be increased. Since the size of the calculation grid cannot be reduced below 2.5 mm, the only way to achieve a better resolution is by increasing the size of the

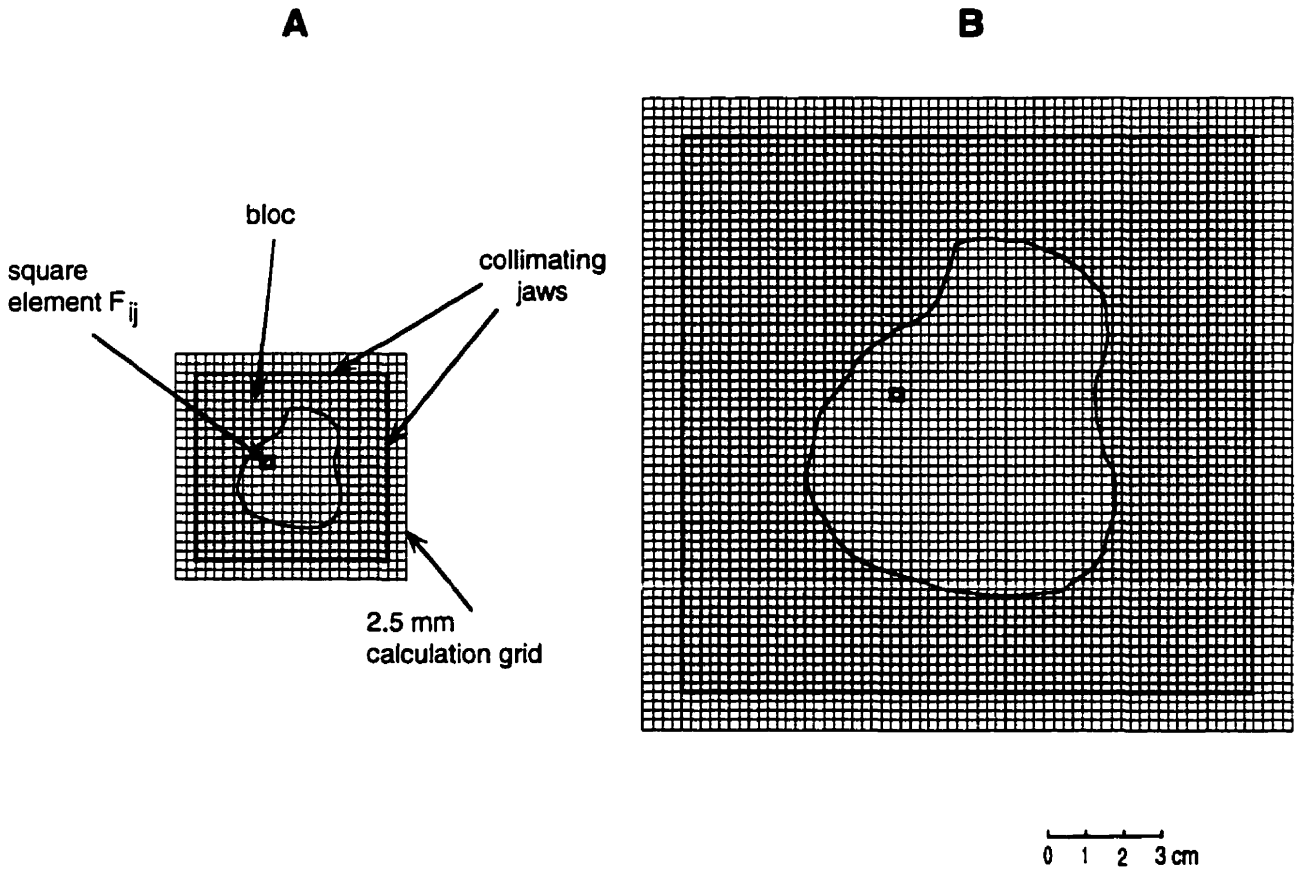

FIGURE 4-4 *Calculation grid used in CADPLAN's photon pencil beam model. (**A**) The irregular field is divided into a matrix of square elements of side 2.5 mm. The field function F(x,y) is defined by assigning a value to each of the square elements, depending on its position in the beam. The value of element F_i is equal to the ratio of its open surface to its total surface if it lies at the edge of the radiation beam. (**B**) The resolution with which the field function models the radiation beam can be improved by scaling the dimensions of the irregular field by a factor of 3, while keeping the size of the calculation grid constant at 2.5 mm.*

irregular field (along with the size of the patient or the phantom), while keeping the size of the grid constant. Increasing the size of the radiation field by a factor of three, which is equivalent to using a 0.83 mm calculation grid, was believed to provide sufficient resolution (FIGURE 4-4 (B)).

To obtain accurate results, however, the beam data used in *CADPLAN's* calculation algorithm must be reconfigured to take into account both the new phantom size and the new field size. At McGill University, stereotactic radiosurgery is performed using 10 MV photons from a Clinac-18 linear accelerator. Thus, in the beam data for the original 10 MV beam, all of the dimensions were scaled by a factor of three; a new 10 MV beam was therefore configured, using the same data as the original 10 MV beam, but entered for fields three times larger and scaled in depth by a factor of three. For example, the *PDD* at a depth of 8 cm for a 5x5 cm^2 field was entered as the *PDD* at a depth of 24 cm for a 15x15 cm^2 field. The beam profile value at x=4 cm for a 5x5 cm^2 field at the configuration depth of 2.5 cm was entered as the beam profile value at x=12 cm for a 15x15 cm^2 field at the configuration depth of 7.5 cm. This was done for all of the beam data required by *CADPLAN's* photon pencil beam model: central axis *PDDs*, beam profiles, and *PSFs*. The *TPRs*, which are used in the calculation of CF_{SSD} and CF_{obl}, were left unchanged. This, however, does not significantly affect the results of the dose calculations since the ratio of *TPRs*, due to the very small difference in field sizes involved, is very close to unity. In order to preserve the proper ratios in the inverse square law factors, such as those arising in the *SSD* correction factor CF_{SSD} (eq. 4-4), the inverse square normalization factor CF_{inv} (eq. 4-6) and the skin obliquity correction factor C_o (eq. 4-18), the configuration *SPD* (and therefore the *SAD* and the nominal *SSD*) were changed from 100 cm to 300 cm. Once the beam data was reconfigured to take into account this new beam geometry, the scatter kernel K_s and the boundary kernel K_b were recalculated by *CADPLAN*.

In order to use this newly configured 10 MV photon beam, the dimensions of the phantom (or the patient) must be scaled appropriately. Thus, the values of the x pixel size, the y pixel size and the z position contained in the header of the phantom (or patient) CT image files were multiplied by a factor of three. Having reconfigured the beam data used in *CADPLAN's* calculation algorithm and having properly scaled the dimensions of the phantom, the size of the irregular fields can now be multiplied by a factor of three.

4.5 Accuracy of alternate beam configuration

In order to verify the accuracy of *CADPLAN* using this newly configured 10 MV photon beam, a comparison was made between relative dose values calculated by *CADPLAN* and relative dose values measured experimentally, using the three irregular fields shown in FIGURE 4-2. This comparison is the same as the one done in section 4.3 (i.e., same dose profiles and same depth doses), with the exception that the alternate 10 MV photon beam configuration was used in all of the dose calculations performed by *CADPLAN.*

A comparison between relative doses calculated by *CADPLAN* and relative doses measured experimentally is displayed in FIGURE 4-5. Once again, while they are shown for one field only (FIGURE 4-5 (A)), these results are representative of the results obtained with all three irregular fields studied. By examining the dose profiles through the central axis in FIGURE 4-5 (C), it can be seen that the agreement between measured and calculated dose values is excellent for points both on and off central axis; *CADPLAN* no longer underestimates the dose received by points located near the edge of the radiation field. This can also be seen in FIGURE 4-5 (B), in which a comparison of depth doses taken parallel to the beam central axis is shown; the agreement between measured and calculated depth dose values is excellent not only

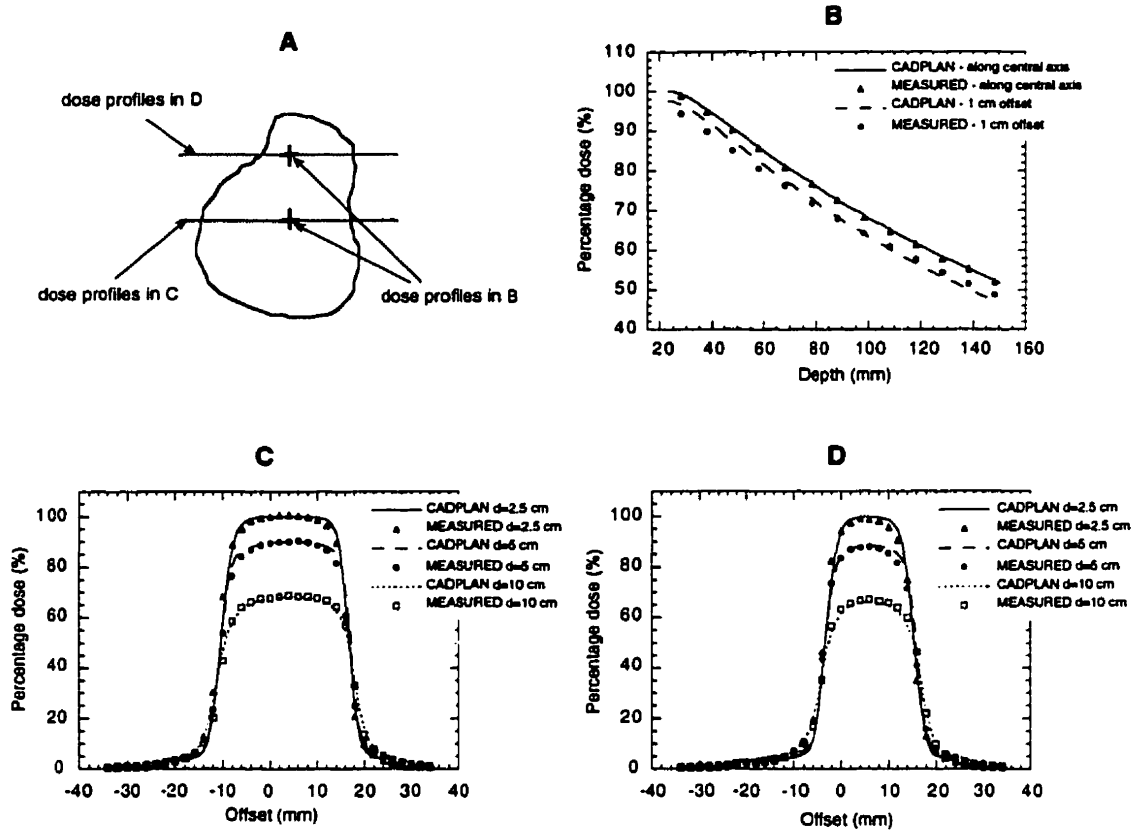

FIGURE 4-5 *Qualitative comparison between relative doses calculated by CADPLAN using the alternate 10 MV photon beam configuration and relative doses measured experimentally. Part* ***A*** *indicates where the dose profiles were taken. Depth doses taken parallel to the beam central axis are shown in* ***B****, while dose profiles in planes perpendicular to the beam central axis are shown in* ***C*** *(profiles through central axis) and* ***D*** *(profiles 1 cm from central axis).*

along the beam central axis (i.e., central axis *PDDs*), but also at an offset position of 1 cm. Finally, the dose profiles taken 1 cm off-axis in planes perpendicular to the beam central axis, displayed in FIGURE 4-5 (D), show a much improved agreement between measured and calculated dose values for points located off the central axis.

While the alternate 10 MV photon beam configuration has significantly improved the agreement between relative doses measured experimentally and relative doses calculated by *CADPLAN*, the question remains as to whether or

not this agreement is good enough to actually perform treatment planning. Thus, a detailed quantitative analysis of the error between the measured data and the calculated data was done. The results of this quantitative analysis were then compared with different acceptability criteria, recommended over the years by various groups,[6,7,8,9] which treatment planning systems should meet in order to be used clinically.

When quantitatively evaluating the performance of a treatment planning system, one usually distinguishes between points in low dose gradient regions with points in high dose gradient regions (such as those in the penumbra region). In low dose gradient regions, the error is expressed in terms of a percentage error between relative dose values, and is calculated using:

$$\%\ Error = \frac{RD_{meas} - RD_{calc}}{RD_{meas}}\ , \qquad (4\text{-}19)$$

where RD_{meas} is the measured relative dose and RD_{calc} is the relative dose calculated by the treatment planning system. In high dose gradient regions, however, it is convenient to express the error in terms of the error in the position of corresponding dose values:

$$Displacement\ Error = X_{meas} - X_{calc}\ , \qquad (4\text{-}20)$$

where X_{meas} is the measured position and X_{calc} is the calculated position of the dose value in question.

In report #42,[8] the ICRU recommends, for points clinically relevant, a dose accuracy of ±2% for low dose gradient regions and a spatial accuracy of ±2 mm for high dose gradient regions. McCullough and Krueger[6] recommend, for points in low dose gradient regions, acceptance criteria of 3% and 4% for ion chamber measurements and TLD measurements, respectively. For points in high dose gradient regions, a 4 mm uncertainty limit is proposed. Dahlin *et al.*[7]

recommend limits of 3% and 2 mm for low dose gradient and high dose gradient regions, respectively. More detailed acceptance criteria for the purpose of treatment planning system verification have been produced by Van Dyk *et al.* [9] They define high dose gradient regions as regions in which the dose varies by more than 30% per cm. For low dose gradient regions, they distinguish between low dose regions (in which the dose is less than 7% of the normalization dose) and high dose regions. They also distinguish between simple geometries, in which a regular field is perpendicularly incident onto a flat homogeneous phantom, with more complex geometries, such as geometries involving irregular fields, tissue inhomogeneities, beam attenuators, etc. Their acceptability criteria are summarized in TABLE 4-1. It should be noted, however, that the percentage errors quoted in TABLE 4-1 are percentages of the central axis normalization dose; they are not relative percentage errors such as the ones that will later be calculated using eq. 4-19.

With these criteria in mind, a detailed numerical analysis of our data was done, using equations 4-19 and 4-20, and using Van Dyk's definition of a high

Geometry	Criterion
i) Simple geometry	
Central ray (excluding build-up region)	2%
Low dose gradient/high dose region	3%
Low dose gradient/low dose region	3%
Large dose gradients	4 mm
ii) Complex geometries	
Low dose gradient/high dose region	4%
Low dose gradient/low dose region	3%
Large dose gradients	4 mm

TABLE 4-1 *Error limits for the purpose of treatment planning system verification, as recommended by Van Dyk et al.[9] Percentage errors are percentages of the central ray normalization dose (i.e., absolute dose errors).*

dose gradient region. For every dose measurement made (dose profiles and depth doses), a relative percentage error between measured and calculated dose values was calculated for points in the high dose/low dose gradient regions (i.e., regions in which the dose is greater than 7% of the normalization dose and varies by less than 30% per cm). In the case of dose profiles (both through central axis and 1 cm off-axis), a displacement error was also calculated for the 80%, 50% and 20% points lying in the penumbra region (high dose gradient region) of the beam profiles. In order to illustrate the error distribution for all of the comparison points from all three irregular fields, the results of this numerical analysis are displayed in error histograms (FIGURE 4-6).

The percentage error histogram for comparison points in the high dose/low dose gradient regions is displayed in FIGURE 4-6 (A). It can be seen that the overall agreement between measured and calculated dose values is excellent, 78% of the comparison points having a percentage error within ±2%, and more than 90% of the points having a percentage error within ±3%. The displacement error histogram for points lying in the high dose gradient regions is shown in FIGURE 4-6 (B). More than 97% of the comparison points were within ±2 mm and all of the comparison points (i.e., 100% of the points) were within ±3 mm of error in distance. These results are well within the various acceptability criteria for the purpose of treatment planning system verification, discussed previously. One can therefore conclude that the dose calculations performed by *CADPLAN* using the alternate 10 MV photon beam configuration are in good agreement with the experimental measurements.

4.6 Summary

In this chapter, we have shown that the dose calculations performed by *CADPLAN* using the alternate 10 MV photon beam configuration are in good

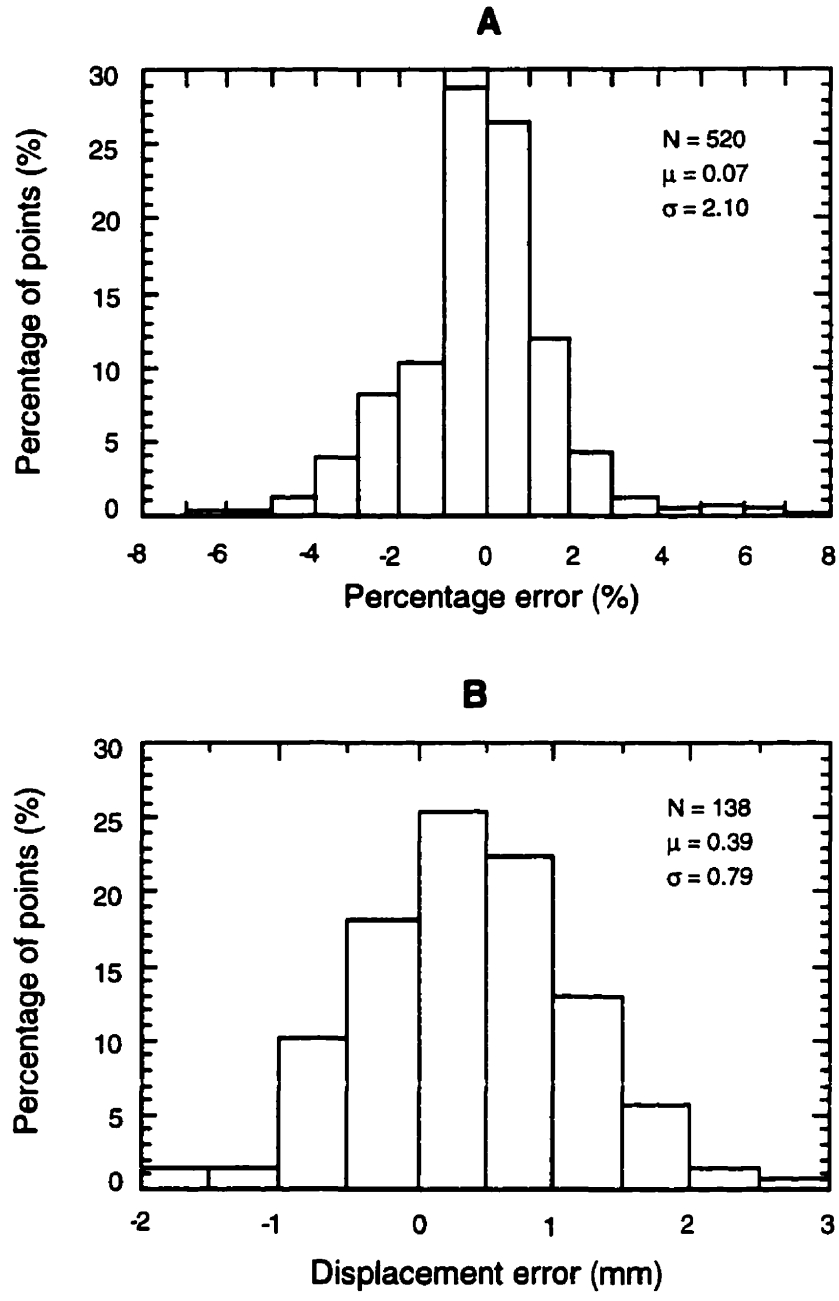

FIGURE 4-6 *Error histograms illustrating the dose error and the displacement error for the comparison points from all three irregular fields. Part* ***A*** *displays the percentage error histogram for points lying in the high dose/ low dose gradient regions. Part* ***B*** *shows the displacement error histogram for the 80%, 50%, and 20% points lying in the penumbra region (high dose gradient region) of the beam profiles. Indicated on each histogram are the total number of comparison points N, the mean error value μ, and the standard deviation σ of the error.*

agreement with the experimental measurements for beam geometries involving a single small irregular field, perpendicularly incident onto a flat, homogeneous, phantom, using an isocentric set-up. This, however, does not necessarily mean that *CADPLAN* can be used for the treatment planning of stereotactic radiosurgery procedures using static conformal fields. The beam geometries involved with this technique are somewhat more complicated: several small irregular fields are used in a non-coplanar way to irradiate a target located in a human head (or a head phantom). Therefore, in chapter 5, as a final verification, a complete radiosurgical procedure using static conformal fields will be performed on the stereotactic head phantom (described in section 3.3.2), and the dose distributions measured experimentally by radiochromic film will be compared with the dose distributions calculated by *CADPLAN*.

4.7 References

[1] J. Milan and R.E. Bentley, **The storage and manipulation of radiation dose data in a small digital computer**, Br. J. Radiol. **47**: 115 (1974).

[2] B. Pike, E.B. Podgorsak, T.M. Peters and C. Pla, **Dose distributions in dynamic radiosurgery**, Med. Phys. **14**: 780-789 (1987).

[3] C. Pla, **A Macintosh-based treatment planning system for brachytherapy and radiosurgery**, in A.R. Hounsell, J.M. Wilkinson, P.C. Williams (eds.): Proceedings of the Xith International Conference on the Use of Computers in Radiotherapy, 20-24 March 1994, Manchester, UK, pp. 138-139.

[4] A. Orfali, **Verification of a 3D external photon beam treatment planning system**, Msc. Thesis, McGill University, Montreal (1996).

[5] Varian Oncology Systems, **CADPLAN 2.7 External Beam Modeling: Reference Manual**, Version 1.0, Varian-Dosetek Oy, Finland (1996).

[6] E.C. McCullough and A.M. Krueger, **Performance evaluation of computerized treatment planning systems for radiotherapy external photon beams**, Int. J. Radiat. Oncol. Biol. Phys. **6**: 1599-1605 (1980).

[7] H. Dahlin, I.L. Lamm, T. Landberg, S. Levernes and N. Ulso, **User requirements on CT based computerized dose planning systems in radiotherapy**, Acta Radiol. Oncol. **22**: 398-415 (1983).

[8] International Comission on Radiation Units and Measurements, **Use of computers in external beam radiotherapy procedures with high-energy photons and electrons**, ICRU Report No. 42 (1983).

[9] J. Van Dyk, R.B. Barnett, J.E. Cygler and P.C. Shragge, **Commissioning and quality assurance of treatment planning computers**, Int. J. Radiat. Oncol. Biol. Phys. **18**: 261-273 (1993).

Chapter 5

Static conformal fields in radiosurgery

5.1 Introduction

In this chapter, we will evaluate the dosimetric advantages of using static conformal fields for radiosurgery of irregular targets by comparing treatment plans using the dynamic radiosurgery technique, with a treatment plan using fixed, non-coplanar, irregularly shaped beams. In order to evaluate the effect of varying the number of static fields irradiating the target, a comparison between treatment plans using a different number of static conformal fields will also be presented. Since these comparisons are based on dose calculations performed by *CADPLAN,* a final verification of *CADPLAN's* accuracy will be carried out by comparing the measured and calculated dose distributions resulting from a complete radiosurgical procedure using static conformal fields. This chapter, however, will begin with a brief description of the protocol we will follow regarding the normalization and evaluation of radiosurgical treatment plans.

5.2 *RTOG Protocol*

In order to compare different radiosurgical treatment plans, a convention must be adopted to ensure that the various plans are dealt with in a consistent manner. For the present work, we have chosen to follow the RTOG (radiation therapy oncology group) 93-05 protocol. This is a protocol for an ongoing study (February 1994 to October 2001) in which McGill University participates intensely, since both the principal investigator and the quality assurance physicist on the protocol are McGill employees. The aim of the study is to determine the effect of using stereotactic radiosurgery prior to conventional radiotherapy and chemotherapy with BCNU for the treatment of supratentorial malignant glioma. Under this protocol, a radiosurgical treatment plan must satisfy certain conditions, which relate to three parameters defined by the RTOG. These three parameters are: the *highest isodose surface completely covering the target,* the *PITV ratio,* and the *MDPD ratio.*

According to the protocol, all treatment plans are to be normalized to (i.e., the 100% dose level assigned to) the prescription dose. Whenever possible, the minimum dose to the target volume is to be chosen as the prescription dose. If this is the case, then the 100% isodose surface completely covers the target volume. If it is not possible (or not desirable) to prescribe to the minimum target dose, a slightly higher dose level may be chosen as the prescription dose, as long as the *highest isodose surface completely covering the target volume* is no less than 90% of the prescription dose. If it is between 80% and 90%, it is considered a minor deviation. If it is below 80%, it is classified as a major deviation.

The second parameter used by the RTOG to evaluate radiosurgical treatment plans is the *PITV ratio* . The *PITV ratio* , which is a measure of the target-dose conformation, is defined as the volume of the prescription isodose surface V_{presc} divided by the target volume V_{target} :

$$PITV\ ratio = \frac{V_{presc}}{V_{target}} . \qquad (5.2)$$

For the treatment plan to be considered per protocol, the *PITV ratio* must be between 1 and 2. If it is between 0.9 and 1, or between 2.0 and 2.5, it is considered a minor deviation. A *PITV ratio* less than 0.9 or greater than 2.5 is categorized as a major deviation.

The third parameter, the *MDPD ratio*, is a measure of the dose homogeneity within the target volume, and is defined as the maximum dose in the target volume D_{max} divided by the prescription dose D_{presc} :

$$MDPD\ ratio = \frac{D_{max}}{D_{presc}} . \qquad (5.1)$$

Under the protocol, the *MDPD ratio* must be less than, or equal to, 2. If it is between 2 and 2.5, it is considered a minor deviation, while a ratio greater than 2.5 is classified as a major deviation. The conditions relating to these three parameters are summarized in TABLE 5-1.

	Highest isodose surface completely covering the target	*PITV ratio*	*MDPD ratio*
Per protocol	≥ 90%	between 1 and 2	≤ 2
Minor deviation	between 80% and 90%	between 0.9 and 1 or between 2 and 2.5	between 2 and 2.5
Major deviation	< 80%	< 0.9 or > 2.5	> 2.5

TABLE 5-1 *Criteria for the three parameters used by the RTOG protocol #93-05 to evaluate radiosurgical treatment plans.*

It is believed that with these three parameters, along with the corresponding isodose distributions and dose-volume histograms (DVHs), the various radiosurgical treatment plans considered in this thesis can be adequately compared, not only qualitatively, but also with some quantitative measure.

5.3 Verification of 3-D dose distribution

In the previous chapter, it was shown that *CADPLAN* could be used to calculate dose distributions produced by small irregular fields for relatively simple irradiation geometries (SAD setup, single beam, normal incidence and flat phantom surface), provided the alternate 10 MV photon beam configuration is used. The irradiation geometry involved with a complete radiosurgical procedure using fixed shaped beams, however, is far more complex; several small irregular fields are used in a non-coplanar manner to irradiate a target located in a human head (or a head phantom). Thus, prior to using *CADPLAN* for treatment planning of radiosurgical procedures based on static conformal fields, its accuracy must be verified once again.

As a final verification of *CADPLAN's* accuracy, a radiosurgical procedure using 7 static, non-coplanar, irregular fields was performed on the stereotactic head phantom described in section 3.3.2. The localization insert containing the irregularly shaped target was inserted into the head phantom, to which a stereotactic frame was affixed. Using the CT localizing attachment, the head phantom was imaged by the CT-simulator (Picker PQ-2000, Picker International, Highland Heights, OH, USA). The CT images were acquired from a scan having a slice thickness of 2.0 mm, a slice separation of 2.0 mm, and a pixel size of 0.547 mm (512 x 512 pixels for a 280 x 280 mm^2 field of view). The CT images were then transferred to the *CADPLAN* External Beam Treatment Planning System, where the contouring of both the head and the target was performed. The total volume of the irregularly shaped target, as contoured on

the CT images, was 9.4 cm^3. In order to use the alternate 10 MV photon beam configuration, the dimensions of the stereotactic head phantom were increased by a factor of three; this was done by multiplying by three the values of the x pixel size, the y pixel size, and the z position contained in the header of the phantom CT image files.

A radiosurgical treatment plan using 7 static conformal fields was made. In order to subsequently compare with the dynamic radiosurgery technique, the static fields were evenly spaced along the trajectory created by the dynamic motion (the familiar baseball seam). The shape of each field conformed to the projection of the target (the beam's-eye view of the target), plus a margin which varied between 1 and 3 mm, this variation being a result of the uncertainties involved with the manufacturing of the custom collimators (section 3.5). The shape of each field along with its gantry and couch angle positions are shown in FIGURE 5-1. These beam outlines were obtained by irradiating radiographic film, isocentrically positioned (SAD=100 cm) at a depth of 8 cm inside a solid water phantom, using the 7 irregularly shaped beams.

Two types of dosimeters were used to record the dose produced by the static conformal fields radiosurgical procedure. A qualitative analysis of the three dimensional dose distribution was first carried out with BANG gels, after which a more detailed quantitative analysis of the dose was done using radiochromic film.

5.3.1 BANG gel

The BANG gel came in a plastic cylindrical flask having a diameter of 6 cm and a length of 17 cm. The gel was inserted in the head phantom, which was then stereotactically positioned on the treatment couch of the Clinac-18 linear accelerator, where the static conformal fields radiosurgical procedure was performed. In order to avoid saturation of the gel, a dose of 4 Gy was delivered to the prescription isodose line, which was chosen as the minimum

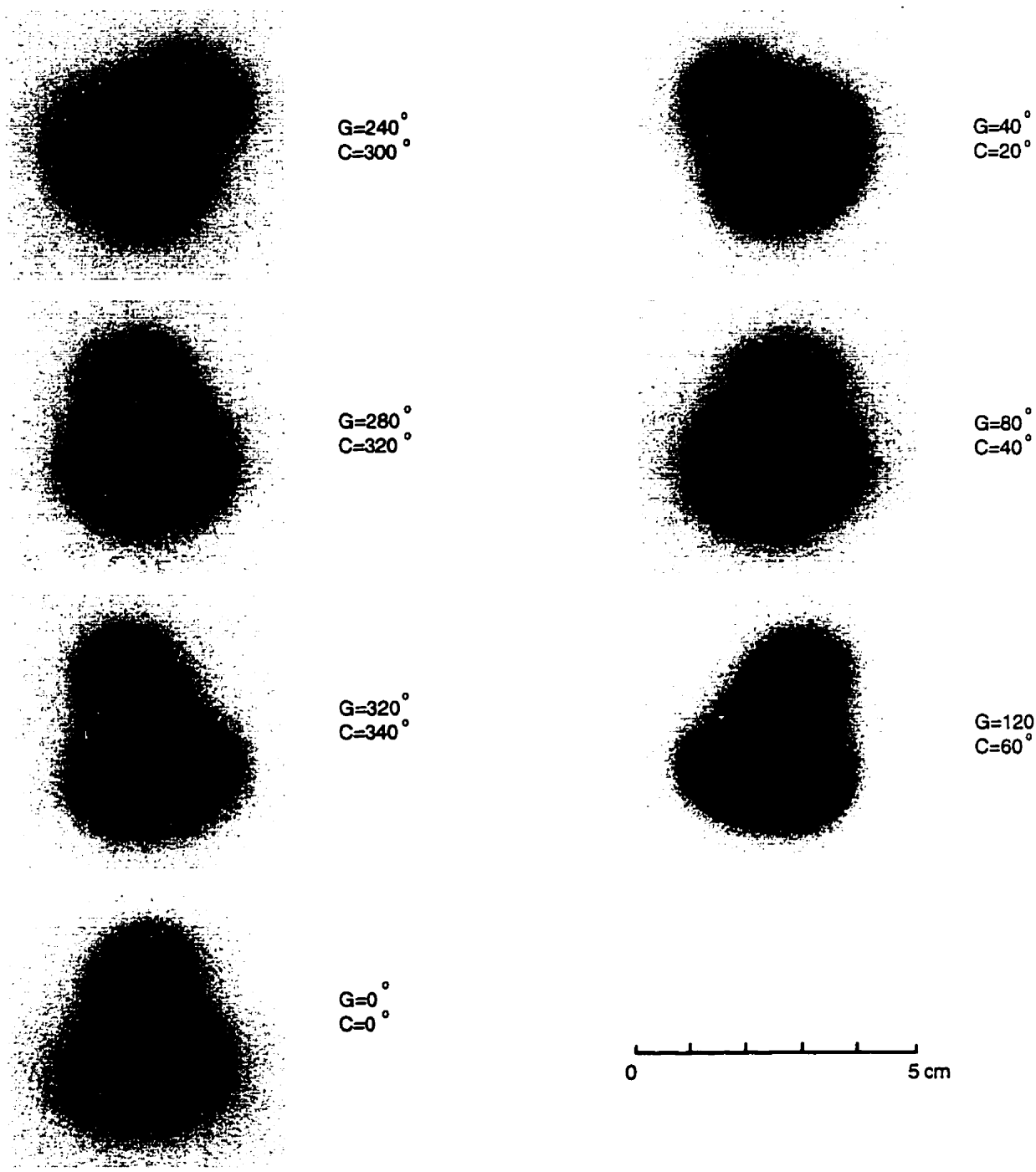

FIGURE 5-1 *Geometric shape along with the gantry angles (denoted by G) and couch angles (denoted by C) of each of the 7 fields of the static conformal fields plan. These beam outlines were obtained by irradiating radiographic film, with the 10 MV photon beam, located at a depth of 8 cm in a solid water phantom, using an isocentric set-up (SAD=100 cm).*

target dose. Thus, the maximum dose within the target volume (which *CADPLAN* predicted to be equal to 121% of the prescription dose) was kept below 5 Gy. In order to prevent photopolymerization of the monomers, the radiosurgical procedure was performed in dark room conditions, thereby minimizing exposure to ambient light. After a waiting period of 2 days, the gels were imaged using a 64 Mhz, 1.5T GE Signa 5X MR imager (General Electric Medical Systems, Milwaukee, WI). A single spin echo pulse sequence was used, with a repetition time (TR) of 6000 ms and an echo time (TE) of 400 ms. The MRI images were acquired from a scan having a slice thickness of 3.0 mm, a slice separation of 3.0 mm, and a pixel size of 1.094 mm (256 x 256 pixels for a 280 x 280 mm^2 field of view). These MRI images were then analyzed using NIH Image 1.59.

FIGURE 5-2 shows a photograph of the BANG gel in the plastic cylindrical flask following irradiation with the 7 static conformal fields. Upon exposure to ionizing radiation, BANG gels become more and more opaque. Thus, the darker region in the upper half of the flask represents the 3-dimensional dose distribution recorded by the gel. While the edges of this opaque region are rather diffuse, one can distinguish a somewhat elongated dose distribution, whose shape resembles that of a pear.

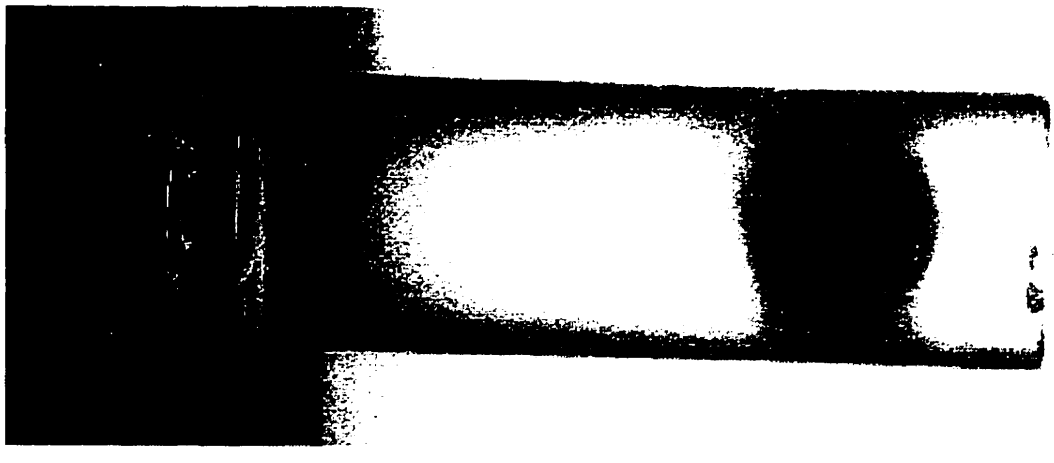

FIGURE 5-2 *Cylindrical flask containing the irradiated BANG gel. The darker region in the upper half of the flask represents the 3-dimensional dose distribution recorded by the gel.*

FIGURE 5-3 (A) shows a montage of 12 consecutive MR axial images for which the maximum dose D_{max} is greater than the prescription dose of 4 Gy. Dose levels greater than 100% of the prescription dose were binned together

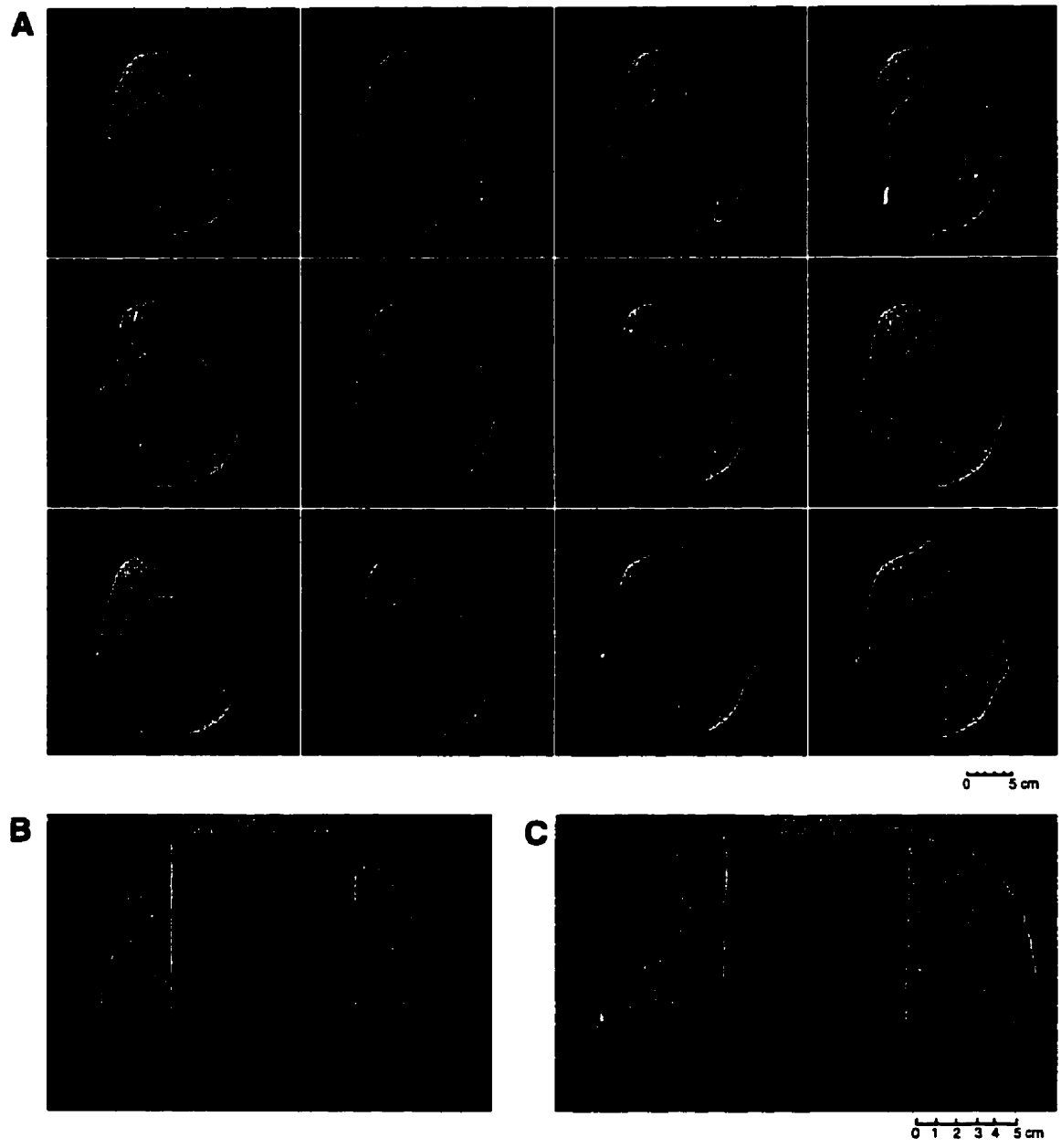

FIGURE 5-3 *Part **A** shows a montage of 12 consecutive MR axial images for which the maximum dose D_{max} is greater than the prescription dose of 4 Gy. Coronal and sagittal reconstructions of the MR images through the center of the target are shown in parts **B** and **C**, respectively. Dose levels greater than 100% of the prescription dose were binned together and are represented by the dark gray regions at the center of the images.*

and are represented by the dark gray regions (of varying size) at the center of the images. Unfortunately, a more detailed quantitative analysis of these MR images was not possible because of the presence of intensity artifacts near the base of the phantom (as we get closer to the stereotactic frame). These intensity artifacts are clearly visible in FIGURES 5-3 (B) and (C), which respectively show a coronal and a sagittal reconstruction of the MR images through the center of the target. For qualitative purposes, dose levels greater than the prescription dose were, once again, binned together and are represented by the dark gray regions at the center of the images (just like for the axial images). While care should be taken in interpreting these results (due to the image artifacts), it is interesting to note the irregular shape of the 3-dimensional dose distribution, which suggests that a certain degree of target-dose conformation has been achieved from the 7 static conformal fields.

These MR images, along with the photograph of the gel, are meant to be used in a qualitative way only; they provide us with the general shape of the 3-dimensional dose distribution produced by the static conformal fields radiosurgical procedure. A more detailed quantitative analysis of the dose distributions, along with a verification of the dose calculations performed by *CADPLAN,* was done using radiochromic film.

5.3.2 Radiochromic film

In order to measure the dose with radiochromic film, the stereotactic head phantom was fitted with the verification insert, which contained one of the film mounts along with a piece of radiochromic film. The phantom was positioned on the treatment couch of the Clinac-18 linear accelerator, where the radiosurgical procedure was performed a total of three times; once for each of the three imaging planes (axial, coronal and sagittal). The minimum target dose, which was once again chosen as the prescription dose, received 40 Gy. After the procedure, the radiochromic films were scanned by the He-Ne laser

digitizer and the resulting images were imported into NIH Image 1.59, thereby mapping the 2-dimensional dose distributions recorded by the films to 256-level grayscale images. The different gray levels (i.e., different dose levels) of the grayscale images were then grouped into different bins, thus creating binned images over which the isodose lines calculated by *CADPLAN* could be overlaid.

The results of the comparison between the dose distributions measured experimentally and the ones calculated by *CADPLAN* are shown in FIGURES 5-4 (A), (B), and (C) for the axial, coronal, and sagittal planes, respectively. As mentioned above, the different gray levels represent the measured data, while the solid black lines represent the dose distributions calculated by *CADPLAN* . Displayed are the 120%, 100%, 90%, 80%, and 50% isodose lines for the axial plane, while, in addition to these isodose levels, the 30% line is also shown for both the coronal and sagittal planes. The lower isodose lines (10% and 20%) are not shown because the small size of the head phantom's film mounts did not allow for large enough pieces of radiochromic film. Nevertheless, the results are still conclusive, since it is the high level dose regions, rather than the low level dose regions, that are mostly of interest in radiosurgery.

With the exception of the 120% line, all of the isodose lines shown (from 100% down to 30%) represent data points lying in high dose gradient regions, which were defined by Van Dyk *et al.* [1] as regions in which the dose varies by more than 30% per cm. Thus, for these points, the error is to be expressed in terms of the difference in the positions of corresponding isodose lines. The proposed uncertainty limit for this error in position is 2 mm by the ICRU[2] and Dahlin *et al.* ,[3] and 4 mm by McCullough and Krueger[4] and Van Dyk *et al.* [1] As can be seen from FIGURE 5-4, the displacement errors between the measured and calculated positions of the 100%, 90%, 80%, 50%, and 30% isodose lines for all three planes are well within the uncertainty limits mentioned above; with the exception of the 30% line in the coronal plane (FIGURE 5-4 (B)), this

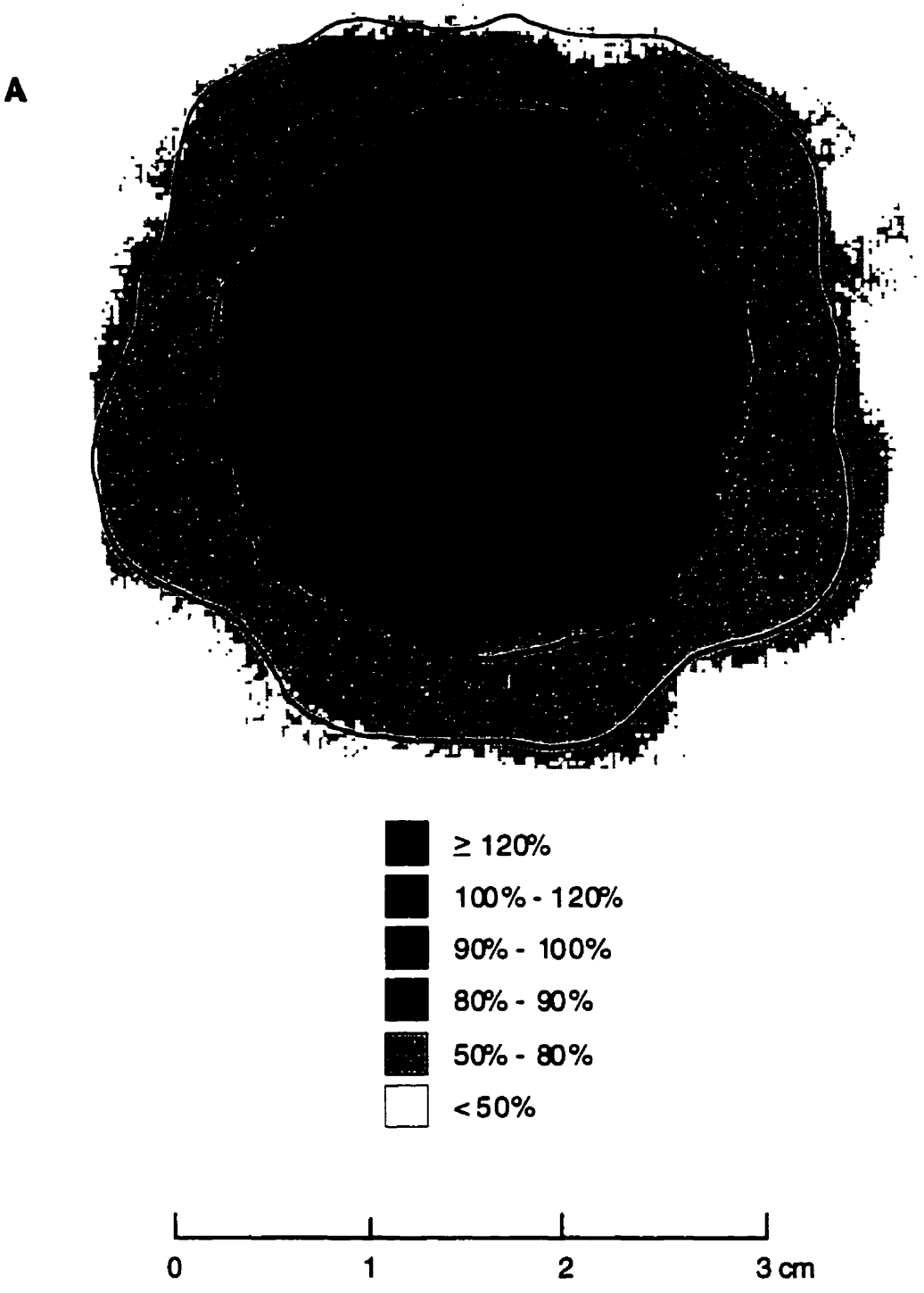

FIGURE 5-4 *Comparison between the dose distributions measured experimentally using radiochromic film and the ones calculated by CADPLAN for the axial (**A**), coronal (**B**), and sagittal (**C**) planes. The different gray levels represent the measured data while the solid black lines are the isodose lines calculated by CADPLAN. Shown here are the 120%, 100%, 90%, 80%, and 50% lines. The 30% line was added for the coronal (**B**) and sagittal (**C**) planes.*

B

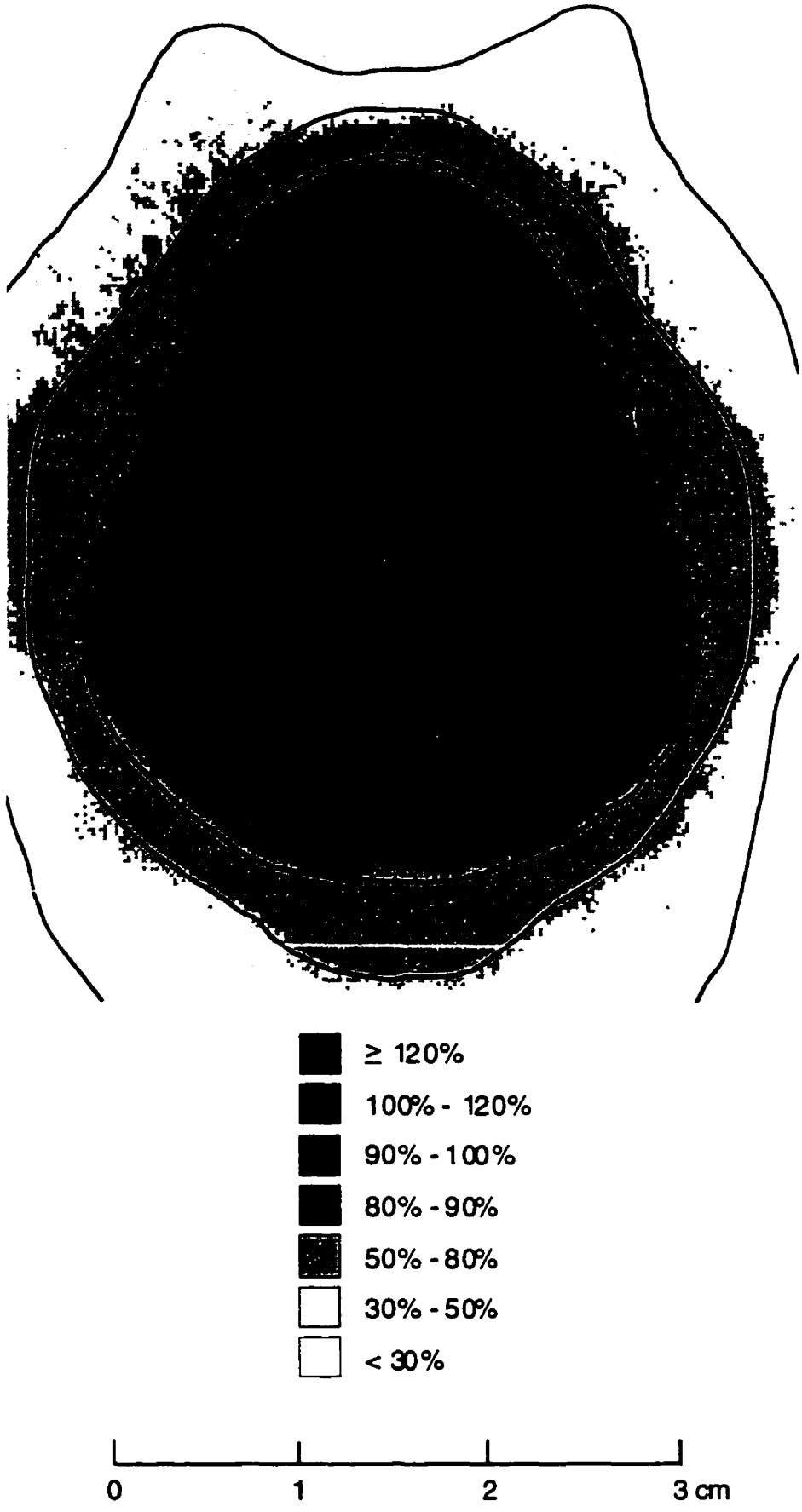

c

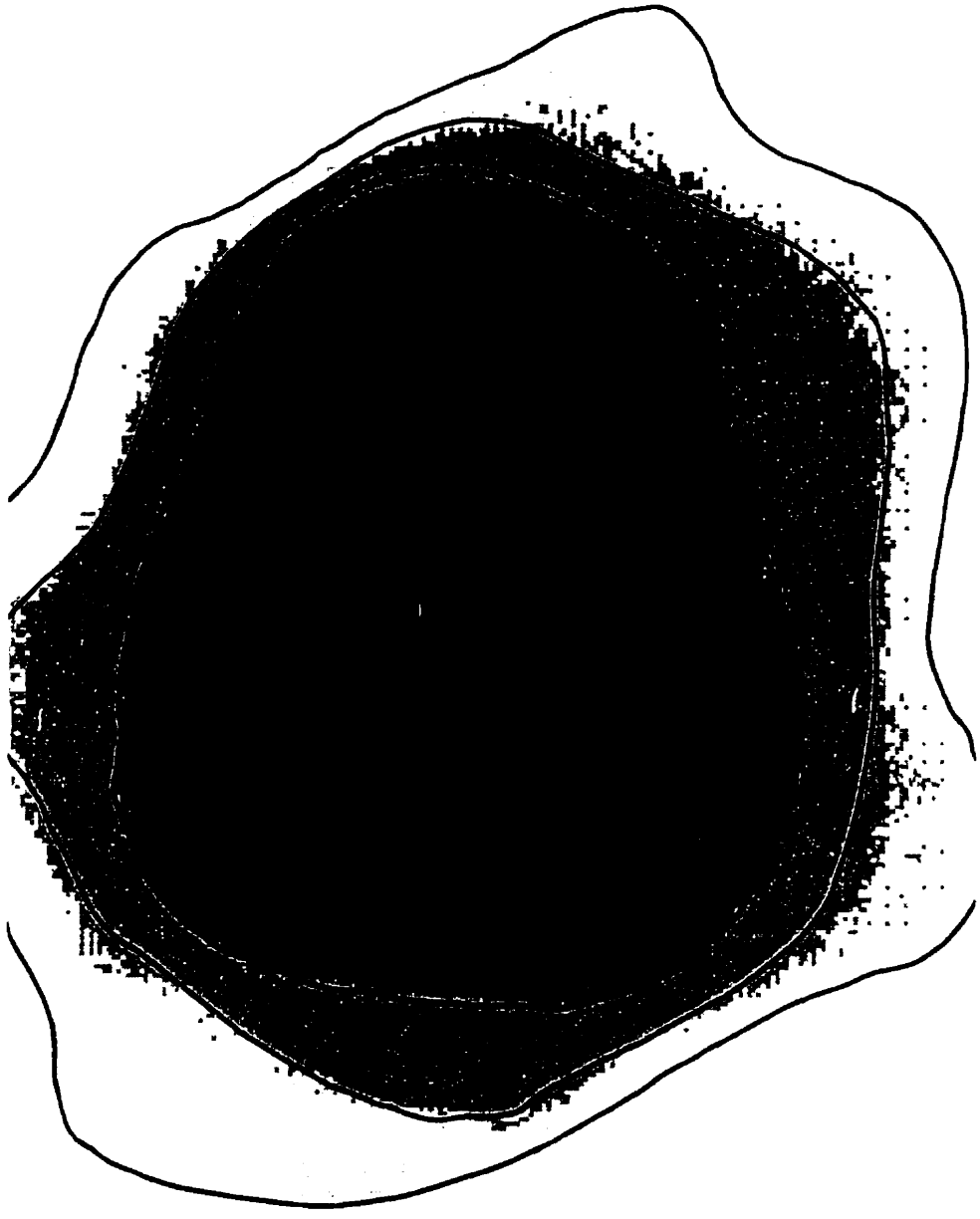

≥ 120%
100% - 120%
90% - 100%
80% - 90%
50% - 80%
30% - 50%
< 30%

0 1 2 3 cm

displacement error is generally less than 2 mm. As for the low dose gradient region (in which the 120% isodose line lies), the error is expressed in terms of a relative percentage error between corresponding dose values. Perhaps the simplest way to evaluate the agreement between measured and calculated dose values for the low dose gradient region is to compare the value of D_{max} in both cases. The maximum dose D_{max} calculated by *CADPLAN* is 120%, 121%, and 121% for the axial, coronal, and sagittal planes, respectively. For the same planes, the maximum dose measured experimentally by the radiochromic film was 122%, 125%, and 124%. Thus, the relative percentage error between the measured and calculated values of D_{max} for all three planes is no more than 3.2%. This maximum error is well within the 4% limit proposed by both McCullough and Krueger[4] and Van Dyk *et al.*,[1] and is comparable to the 3% limit recommended by Dahlin *et al.* [3]

Thus, the dose distributions calculated by the *CADPLAN* External Beam Treatment Planning System, modified to deal with irregularly shaped radiosurgical beams, are in good agreement with the dose distributions measured experimentally using radiochromic film. Having showed that we can rely on *CADPLAN's* dose calculations for radiosurgical procedures involving fixed shaped beams, we are now in a position to evaluate the dosimetric advantages of using such a technique for the radiosurgery of irregular targets.

5.4 Static conformal fields technique vs. dynamic technique

In order to evaluate the advantages of the static conformal fields technique, a comparison was made between the static fields plan developed in the previous section and treatment plans using the dynamic radiosurgery technique with 1 and 2 isocenters. The same set of CT images (i.e., the CT images of the stereotactic head phantom containing the pear shaped target) was used for the static fields plan as well as for the dynamic plans. The two

dynamic plans, however, were developed using the McGill Planning System (MPS). The 1-isocenter plan uses a 4 cm diameter circular field to irradiate the target, while the 2-isocenter plan uses two circular fields, one with a diameter of 2.75 cm, and the other 1.5 cm. In both cases, an optimization effort was made to obtain the treatment plan that delivered the most uniform dose to the target volume, while simultaneously minimizing the amount of healthy tissue irradiated to high doses. In order to be consistent when comparing the different treatment plans, all plans were normalized to the minimum target dose (as suggested by the RTOG protocol #93-05).

Isodose distributions calculated at the center of the target in the transverse, coronal, and sagittal planes are shown in FIGURES 5-5, 5-6, and 5-7, for the 1-isocenter dynamic plan, the 2-isocenter dynamic plan, and the static fields plan, respectively. Shown are the 100% (i.e., minimum target dose), 90%, 80%, 50%, 30% and 10% isodose surfaces, along with the maximum dose (denoted by the white asterisk) for each of the slices. A study of these isodose distributions allows for a qualitative comparison between the different treatment plans. It can be seen, from FIGURE 5-5, that the 1-isocenter dynamic plan delivers a fairly homogeneous dose to the target volume, the maximum dose being equal to 110% of the prescription dose. Because of the spherical shape of the isodose surfaces, however, the 1-isocenter dynamic plan treats a rather large amount of healthy tissue to high doses. This is in contrast with the 2-isocenter dynamic plan, shown in FIGURE 5-6, which irradiates very little healthy tissue to high doses; the conformation between the isodose surfaces and the target volume is excellent. The drawback of this plan, however, is the very large dose inhomogeneities within the target volume, the maximum dose to the target being twice the prescription dose (D_{max}= 200%). The isodose distributions resulting from the static conformal fields plan are displayed in FIGURE 5-7. The static fields plan seems to combine the advantages of both dynamic plans (shown in FIGURES 5-5 and 5-6); a good conformation of the

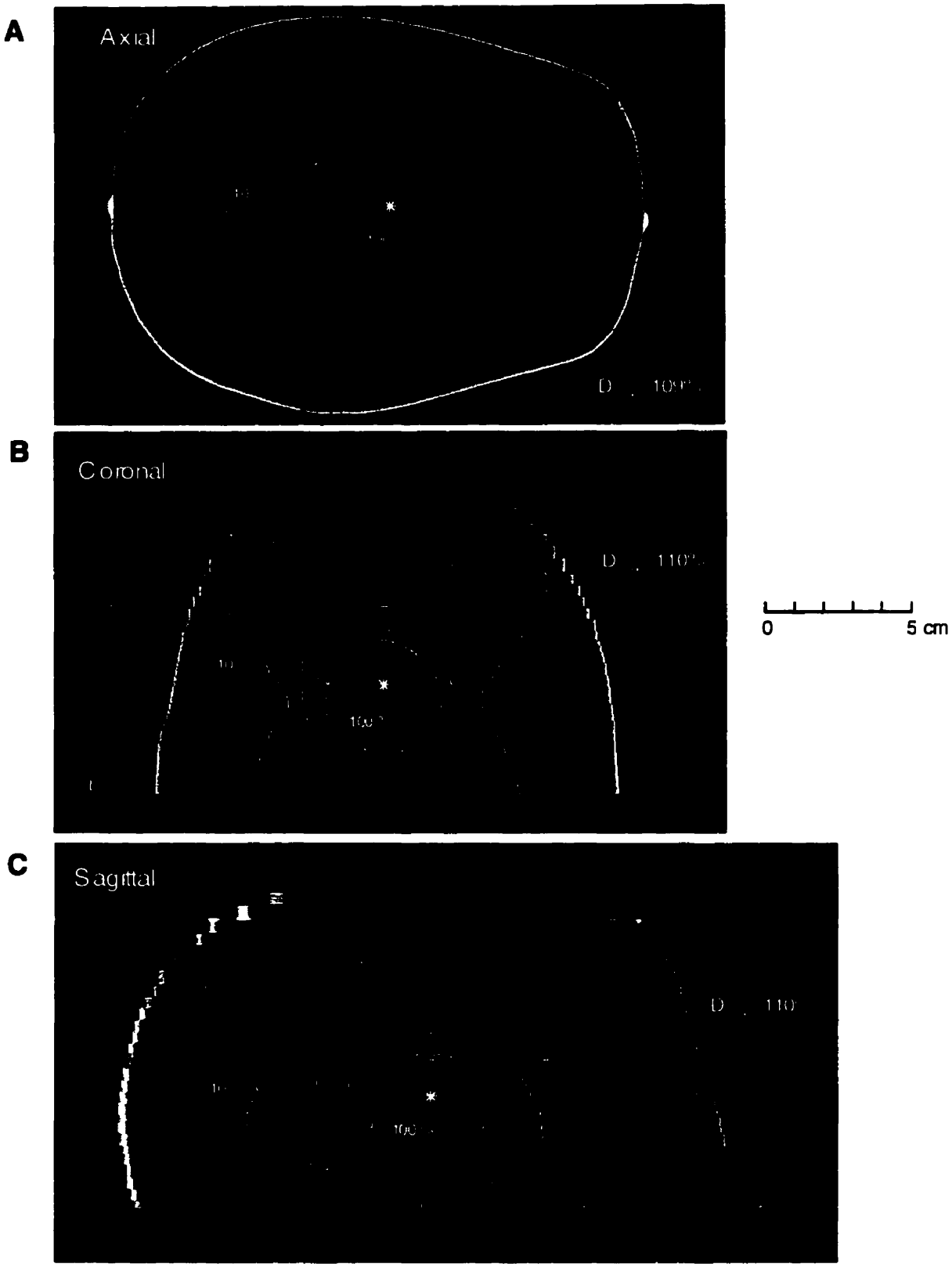

FIGURE 5-5 *Isodose distributions calculated at the center of the target in the axial (**A**), coronal (**B**), and sagittal (**C**) plane for the 1-isocenter dynamic plan. Shown are the 100%, 90%, 80%, 50%, 30%, and 10% lines.*

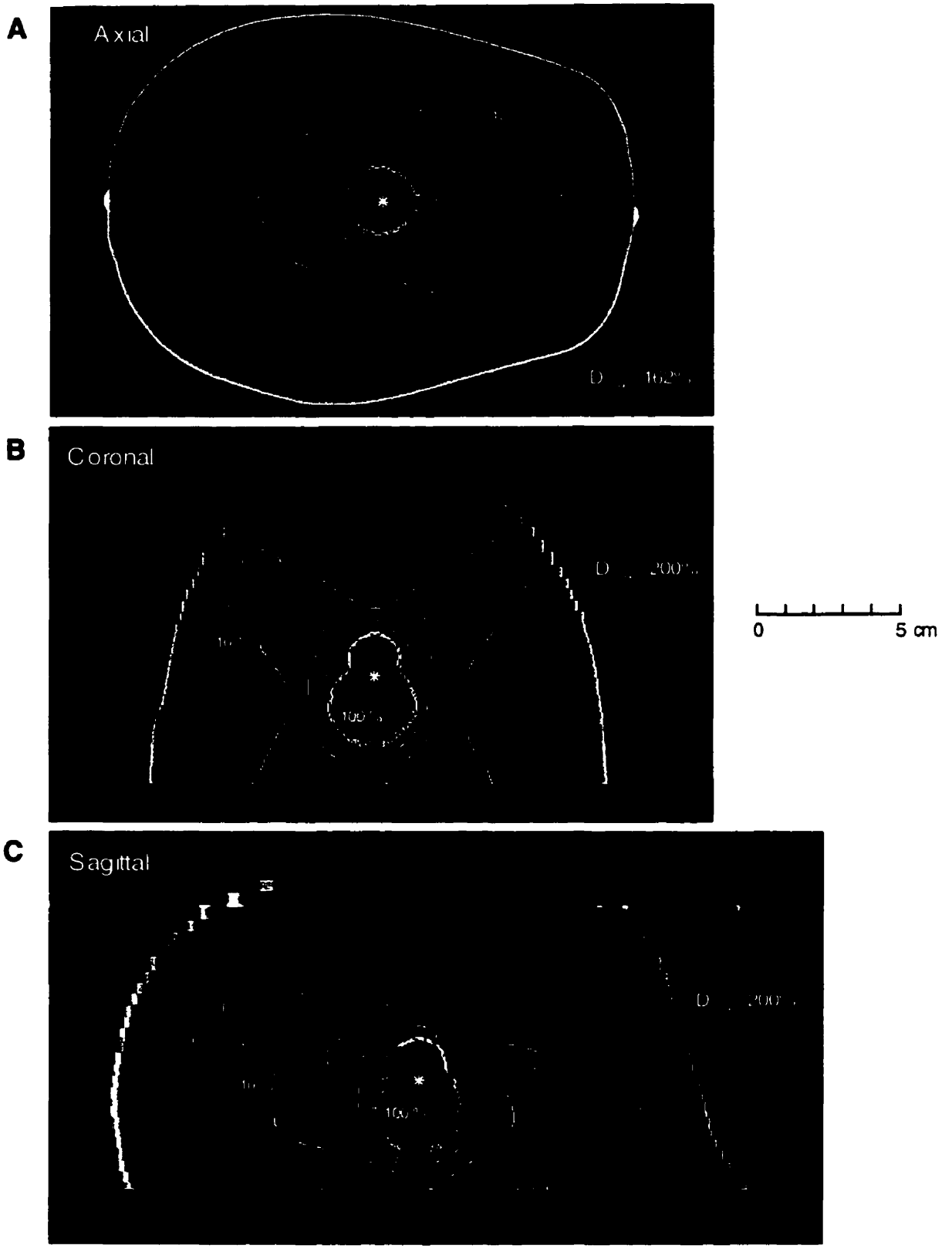

FIGURE 5-6 *Isodose distributions calculated at the center of the target in the axial (**A**), coronal (**B**), and sagittal (**C**) plane for the 2-isocenter dynamic plan. Shown are the 100%, 90%, 80%, 50%, 30%, and 10% lines.*

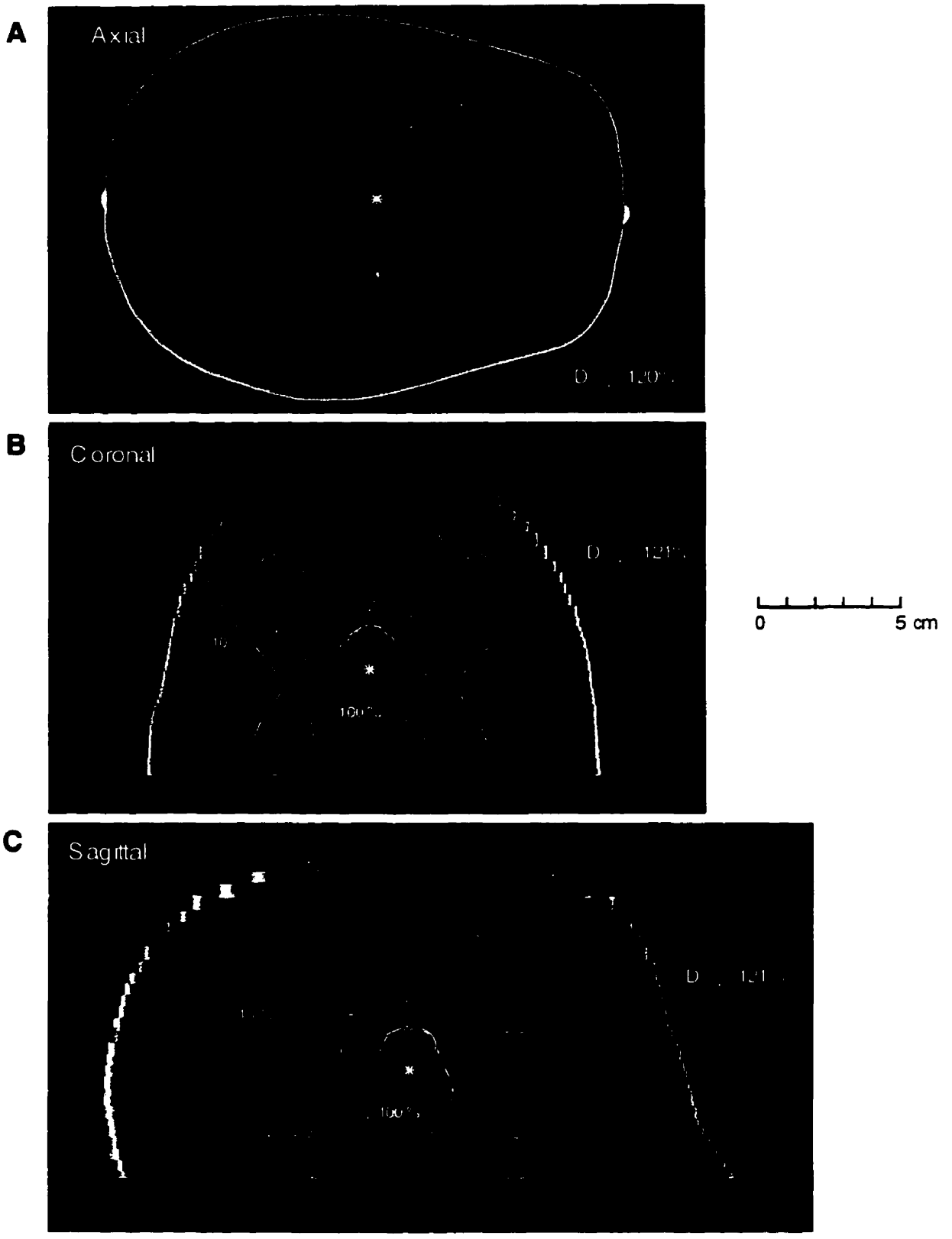

FIGURE 5-7 *Isodose distributions calculated at the center of the target in the axial (**A**), coronal (**B**), and sagittal (**C**) plane for the static fields plan. Shown are the 100%, 90%, 80%, 50%, 30%, and 10% lines.*

dose to the target volume is achieved, while, concurrently, a fairly homogeneous dose is delivered to the target volume, the maximum dose being 121% of the prescription dose.

The values of the RTOG parameters for these plans, shown in TABLE 5-2, confirm the qualitative findings arrived at by studying FIGURES 5-5, 5-6 and 5-7. As previously mentioned, the highest isodose surface completely covering the target is 100% for each plan (since all treatment plans were normalized to the minimum target dose). According to the criteria stated in TABLE 5-1, both the 2-isocenter dynamic plan and the static fields plan would be considered per protocol by the RTOG. The 1-isocenter dynamic plan, however, would not be per protocol because of its *PITV ratio* of 2.34. Since the prescription isodose surface (100% dose level) completely covers the target volume in all three plans, differences in the *PITV ratios* are uniquely due to differences in the amounts of healthy tissue irradiated to the 100% dose level. Thus, the 1-isocenter dynamic plan treats 1.34 TV (where 1 TV = 9.4 cm^3 represents the volume of the target) of healthy tissue to the prescription dose while, the 2-isocenter dynamic plan and the static fields plan treat 0.38 TV and 0.41 TV, respectively.

Plan	*Highest isosurface completely covering the target*	*PITV ratio*	*MDPD ratio*
Dynamic 1 isocenter	100%	2.34	1.10
Dynamic 2 isocenters	100%	1.39	2.00
7 static fields	100%	1.41	1.21

TABLE 5-2 *Values of the RTOG parameters for the dynamic 1-isocenter plan, the dynamic 2-isocenter plan, and the 7 static fields plan.*

Regarding the *MDPD ratio,* which is a measure of the target-dose homogeneity, it is the 2-isocenter dynamic plan that stands out with its *MDPD ratio* of 2.00, compared to 1.10 and 1.21 for the 1-isocenter dynamic plan and the static fields plan, respectively. This is indicative of the fact that very large target dose inhomogeneities are involved with the 2-isocenter plan. Thus, the static conformal fields plan provides target-dose conformation comparable to the 2-isocenter dynamic plan, while delivering a much more uniform dose to the target volume.

For a more detailed quantitative comparison, we must examine the target and healthy tissue cumulative dose-volume histograms (DVHs), shown in FIGURE 5-8 for the different treatment plans. The target DVHs, displayed in FIGURE 5-8 (A), simply confirm what was previously indicated by the *MDPD ratio* ; the dose within the target volume is much more uniform for the 1-isocenter dynamic plan (D_{max}=110%) and for the static fields plan (D_{max}=121%), than for the 2-isocenter dynamic plan (D_{max}=200%).

The healthy tissue DVHs (the target volume being excluded) are displayed in FIGURE 5-8 (B). For every dose level shown (up to approximately the 110% dose level), a considerably larger volume of normal tissue is irradiated by the 1-isocenter dynamic plan than by the two other plans. This is, of course, what is expected from treating an irregular target with spherical isodose surfaces. As for the 2-isocenter dynamic plan and the static fields plan, the amount of healthy tissue treated to various dose levels in both cases is similar. This is illustrated in TABLE 5-3, in which volumes of normal tissue receiving different percentages of the prescription dose are shown, for the three plans studied. The 1-isocenter dynamic plan clearly treats the greatest volume of healthy tissue to intermediate (e.g., 50% of the prescription dose) and high (e.g., 80% of the prescription dose) doses; approximately 2 and 3 times more volume than that treated by the other two plans, respectively. The difference in

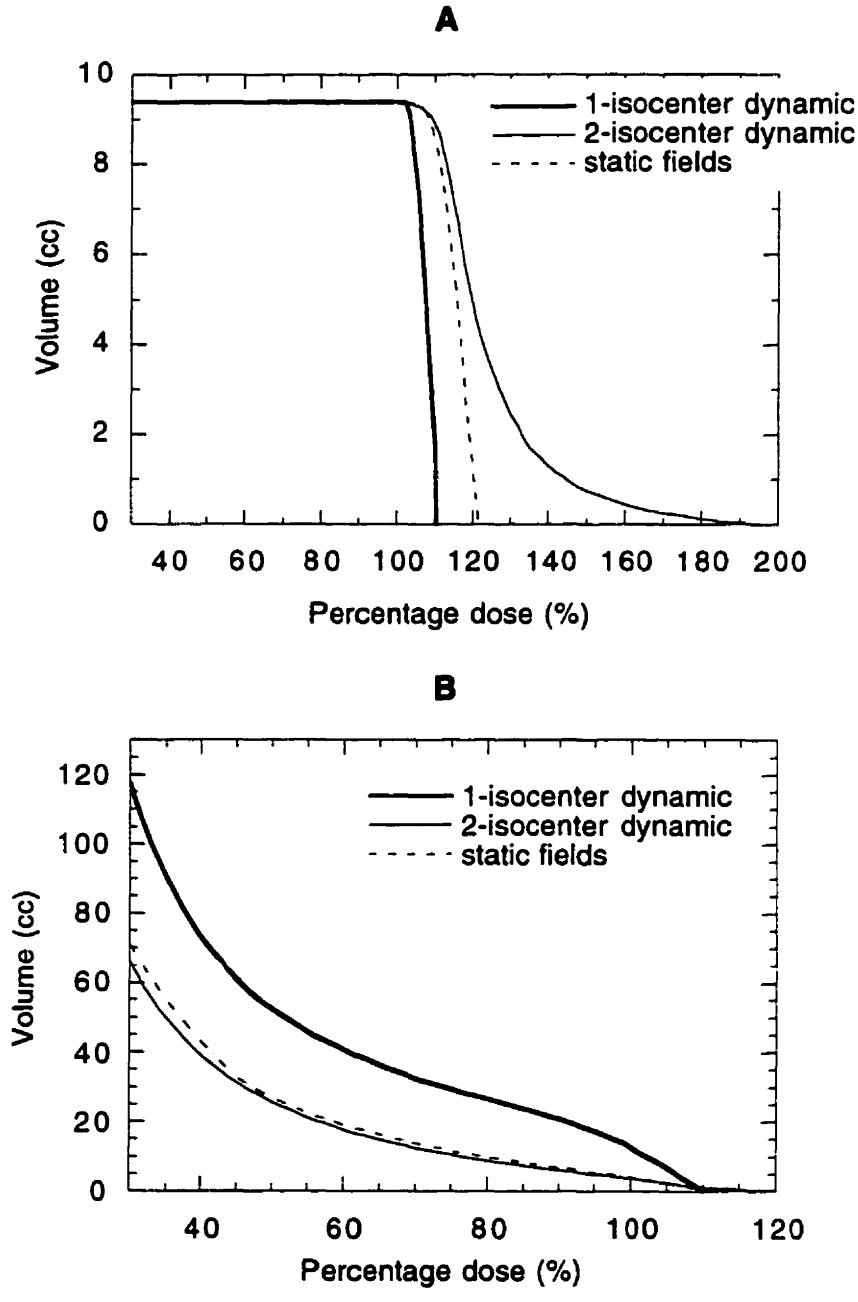

FIGURE 5-8 *Cumulative dose-volume histograms (DVHs) for the dynamic 1-isocenter plan, the dynamic 2-isocenter plan, and the 7 static fields plan. The target volume DVHs are shown in* ***A****, while the healthy tissue DVHs are shown in* ***B****. All doses have been normalized to the minimum target dose.*

Plan	100%	90%	80%	50%
Dynamic 1 isocenter	12.6	20.9	26.5	52.4
Dynamic 2 isocenters	3.7	6.2	8.9	25.5
7 static fields	3.9	6.7	9.7	26.9

TABLE 5-3 *Volumes of healthy tissue (in cm^3) irradiated to different levels of the prescription dose for the three treatment plans studied: the dynamic 1-isocenter plan, the dynamic 2-isocenter plan, and static conformal fields plan.*

volume between the 2-isocenter dynamic plan and the static fields plan, however, is less than 10% for every dose level shown.

Thus, the dosimetric advantages of using static conformal fields for the radiosurgery of irregular targets are quite clear. Because of the much improved target-dose conformation, the use of fixed shaped beams, as opposed to the 1-isocenter dynamic technique, reduces the amount of healthy tissue treated to intermediate and high doses by a factor ranging between 2 and 3. A similar conformation between the dose and the target volume can be achieved by irradiating the target with 2 isocenters using the dynamic technique. The inhomogeneity in target dose relative to the prescription dose involved with this technique, however, is 100%, compared to only 21% for the static conformal fields technique. The use of static conformal fields, therefore, represents an attractive alternative to the dynamic technique for radiosurgical cases involving irregularly shaped targets.

5.5 Comparison between various static fields plans

In order to evaluate the effect of varying the number of fields irradiating the target, a comparison was made between treatment plans using a different

number of fixed, non-coplanar, shaped beams. Once again, the stereotactic head phantom containing the irregularly shaped target served as a basis for this comparison. Thus, treatment plans using 3, 5, 7, 9 and 11 static conformal fields evenly distributed along the dynamic path were developed using *CADPLAN* (with the alternate 10 MV photon beam configuration). The gantry and couch angle positions of each field are shown in TABLE 5-4, for all 5 treatment plans. For every plan, the shape of each field conformed to the projection (beam's-eye view) of the target, plus a 2 mm margin (due to penumbra). Once again, to be consistent when comparing them, all treatment plans were normalized to the minimum target dose.

Cumulative DVHs of the target volume for each of the treatment plans are shown in FIGURE 5-9 (A). The maximum dose inside the target volume is 128%

Plan	Gantry angle	Couch angle	Plan	Gantry angle	Couch angle
3 fields	240	300	9 fields	240	300
	0	0		270	315
	120	60		300	330
				330	345
5 fields	220	290		0	0
	290	325		30	15
	0	0		60	30
	70	35		90	45
	140	70		120	60
7 fields	240	300	11 fields	230	295
	280	320		250	305
	320	340		270	315
	0	0		300	330
	40	20		330	345
	80	40		0	0
	120	60		30	15
				60	30
				90	45
				110	55
				130	65

TABLE 5-4 *Gantry and couch angles for each of the treatment fields of the 3, 5, 7, 9 and 11 static conformal fields plans.*

for the 3-field plan, 125% for the 5-field plan, 122% for the 7-field plan, 120% for the 9-field plan, and 119% for the 11-field plan. Thus, the minimum dose to the target volume being 100% in every case, the target-dose homogeneity increases as the number of fields increases. The differences in target-dose uniformity between the 3-field plan and the 11-field plan, however, are minimal.

Cumulative DVHs for the surrounding normal tissue are displayed in FIGURE 5-9 (B). The discrete nature of the gantry motion for the static fields plans (as opposed to the continuous gantry motion for the dynamic technique) is reflected in the stepwise nature of the DVHs. Furthermore, as the number of fields increases, the volume of healthy tissue irradiated at medium and high doses decreases, while the volume irradiated to low doses (≤ 10% of prescription dose) increases. This is due to the fact that the volume over which the dose outside the target is spread around, increases with an increasing number of fields. TABLE 5-5 shows a comparison between the volumes of healthy tissue irradiated to various percentages of the prescription dose by the different treatment plans. For every dose level shown, the volume of normal tissue decreases with the number of fields, as expected. Increasing the number of fields from 5 to 7 reduces the amount of healthy tissue receiving intermediate (e.g., 50% of prescription dose) and high (e.g., 80% of prescription dose) doses

Number of static fields	100%	90%	80%	50%
3	8.8	12.2	17.0	120.9
5	6.6	10.0	13.9	49.2
7	5.5	8.9	12.5	33.8
9	5.0	8.2	11.7	30.1
11	4.5	7.9	11.2	28.6

TABLE 5-5 *Volumes of healthy tissue (in cm^3) receiving different percentages of the prescription dose in the 3, 5, 7, 9 and 11-field plans.*

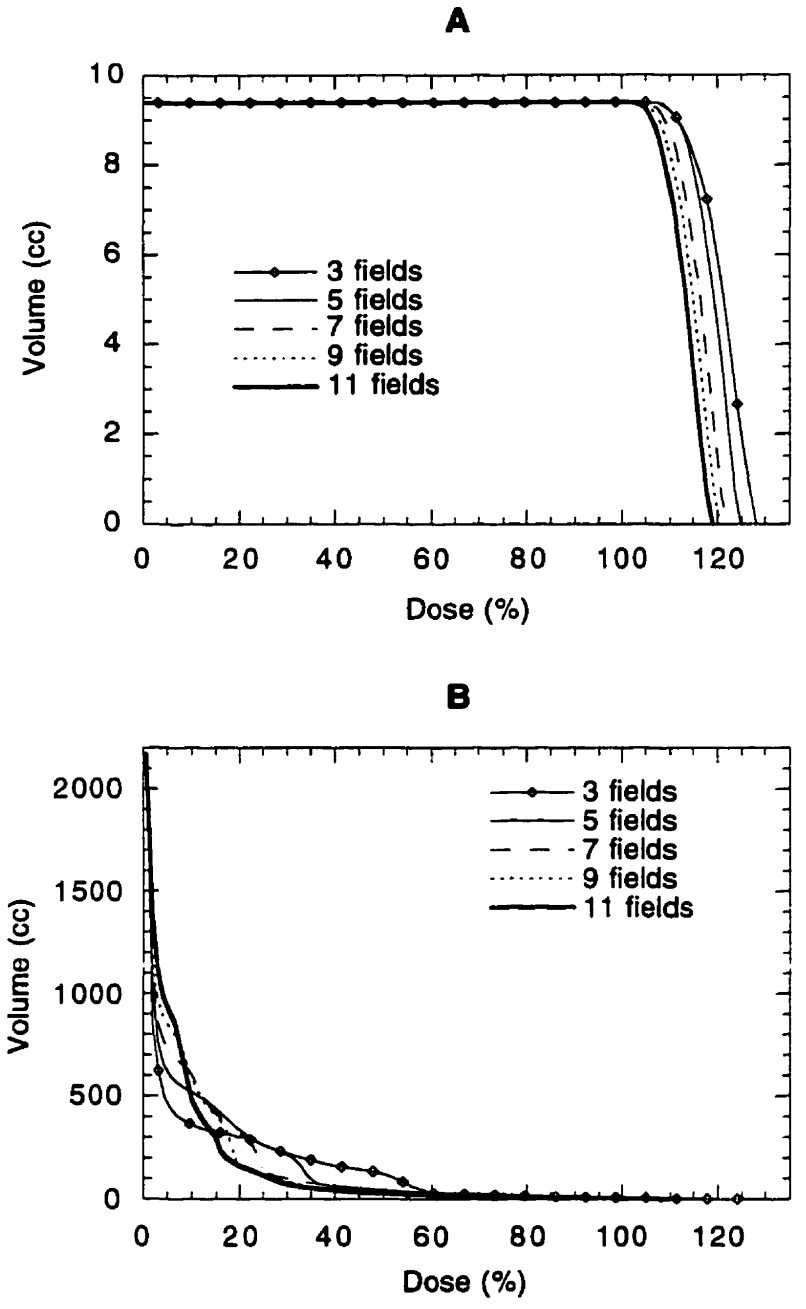

FIGURE 5-9 *Cumulative dose-volume histograms (DVHs) for the 3, 5, 7, 9 and 11 static fields plans. The target volume DVHs are shown in* ***A****, while the healthy tissue DVHs are shown in* ***B****. All doses have been normalized to the minimum target dose.*

by 31% and 10%, respectively. These volumes decrease by another 11% and 6% respectively when the number of fields is increased from 7 to 9, and by 5% and 4% when the number of fields is further increased from 9 to 11.

The values of the RTOG parameters for the five static fields plans are shown in TABLE 5-6. As expected, the *PITV ratio* decreases with the number of fields, reflecting the fact that the amount of healthy tissue treated to the prescription dose (i.e., the 100% dose level) decreases. Thus, a better conformation of the dose to the target volume is achieved by increasing the number of fields. The *MDPD ratio* is also seen to decrease with the number of fields, reflecting the fact that the dose within the target volume becomes more and more uniform.

Number of static fields	*Highest isodose surface completely covering the target*	*PITV ratio*	*MDPD ratio*
3	100%	1.94	1.28
5	100%	1.70	1.25
7	100%	1.59	1.22
9	100%	1.53	1.20
11	100%	1.48	1.19

TABLE 5-6 *Values of the RTOG parameters for the 3, 5, 7, 9, and 11-field plans.*

Thus, increasing the number of fields irradiating the target generally results in both a greater dose homogeneity within the target volume and a greater tissue sparing effect. The amount by which the target dose homogeneity and the degree of tissue sparing increase with the number of fields, however, is not constant; a greater effect is observed when the number of fields is increased from 5 to 7 than from 7 to 9, which itself has a greater effect than an increase from 9 to 11 fields. Counterbalancing these dosimetric

advantages is the fact that increasing the number of fields irradiating the target also results in more lengthy and complicated treatment planning and treatment delivery procedures. This suggests that a compromise should be reached between the degree of tissue sparing and target dose uniformity achieved (which both increase with the number of fields) and the ease with which the radiosurgical procedure can be planned and delivered (which decreases with the number of fields).

While, in clinical situations, additional factors are to be considered when determining the exact number of fields irradiating the target (such as the location of the target, its proximity to sensitive structures, etc.), it is suggested, based on the results obtained in this chapter, that the number of fields used be between 7 and 9. It was previously shown that the amount of healthy tissue irradiated to intermediate and high doses decreases significantly (reductions of 31% and 10%, respectively) when the number of fields is increased from 5 to 7. Therefore, the number of fields irradiating the target should be no less than 7, whenever possible. On the other hand, very little is achieved by irradiating the target with more than 9 fields; an increase to 11 fields only reduces the amount of healthy tissue irradiated to intermediate and high doses by 5% and 4%, respectively. Thus, a number of fields between 7 and 9 represents a reasonable compromise between the degree of target-dose conformation and target-dose homogeneity achieved, and the ease of treatment planning and treatment delivery procedures.

5.6 Summary

A final verification of *CADPLAN's* accuracy showed a good agreement between the measured and the calculated dose distributions resulting from a complete static conformal fields radiosurgical procedure. Showing we could rely on the dose calculations performed by *CADPLAN* was important since all

of the following comparisons involved radiosurgical treatment plans that were obtained using *CADPLAN.*

The use of static conformal fields for radiosurgery of irregular targets was investigated by comparing treatment plans using the dynamic technique with 1 and 2 isocenters, with a treatment plan using 7 fixed, non-coplanar, irregularly shaped beams. The static conformal fields plan achieved a target-dose conformation similar to the 2-isocenter dynamic plan, treating 2 to 3 times less healthy tissue to intermediate and high doses than the 1-isocenter dynamic plan, while delivering a much more homogeneous dose to the target volume.

In order to evaluate the effect of varying the number of static fields irradiating the target, a comparison was also done between treatment plans using a different number of static conformal fields. While the degree of tissue sparing (i.e., target-dose conformation) and target-dose homogeneity were both shown to increase with the number of fields, this increase was found to become smaller and smaller as the number of fields was successively raised from 5 to 7, from 7 to 9 and, ultimately, from 9 to 11. It was therefore argued that a number of fields between 7 and 9 represented a reasonable compromise between the degree of tissue sparing and target-dose uniformity achieved, and the ease with which the radiosurgical procedure is planned and delivered.

5.7 References

[1] J. Van Dyk, R.B. Barnett, J.E. Cygler and P.C. Shragge, **Commissioning and quality assurance of treatment planning computers**, Int. J. Radiat. Oncol. Biol. Phys. **18**: 261-273 (1993).

[2] International Comission on Radiation Units and Measurements, **Use of computers in external beam radiotherapy procedures with high-energy photons and electrons**, ICRU Report No. 42 (1983).

[3] H. Dahlin, I.L. Lamm, T. Landberg, S. Levernes and N. Ulso, **User requirements on CT based computerized dose planning systems in radiotherapy**, Acta Radiol. Oncol. **22**: 398-415 (1983).

[4] E.C. McCullough and A.M. Krueger, **Performance evaluation of computerized treatment planning systems for radiotherapy external photon beams**, Int. J. Radiat. Oncol. Biol. Phys. **6**: 1599-1605 (1980).

Chapter 6

Conclusions

6.1 Thesis Summary

The aim of radiosurgery is to deliver a high dose of radiation inside the target volume, while concurrently minimizing the dose to the surrounding healthy brain tissue. Conventional radiosurgical techniques (multiple arcs, dynamic radiosurgery, conical rotation) yield isodose distributions which have a spherical shape. However, most lesions treated by radiosurgery are not spherical; they are irregularly shaped to some degree. Thus, treating an irregular target with conventional radiosurgical techniques causes a significant amount of healthy tissue to be exposed to high radiation doses; hence the need to conform the shape of the isodose surfaces to the shape of the target.

It has been shown, in this thesis, that the use of static conformal fields for radiosurgery of irregular targets, as opposed to the 1-isocenter dynamic technique, reduces the amount of healthy tissue treated to intermediate (>50% of prescription dose) and high (>80%) doses by a factor ranging between 2 and 3. A similar degree of tissue sparing (i.e., target-dose conformation) can be achieved by irradiating the target used in our study with two isocenters using the dynamic technique. The dose inhomogeneities within the target volume involved with this technique, however, are 100%, compared to only 21% for the static conformal fields technique. While the exact clinical effects of target-dose inhomogeneities are still unclear, they have been associated with radiosurgical complications.[1] Furthermore, treating a lesion with multiple isocenters

significantly increases the complexity and the time required to plan and deliver the treatment.

We have also studied the effect of varying the number of fields irradiating the target by comparing radiosurgical treatment plans using a different number of static conformal fields. Increasing the number of fields generally resulted in both a greater tissue sparing effect and a greater dose uniformity within the target volume. However, the amount by which the degree of tissue sparing increased with the number of fields was not constant; a greater effect was observed when the number of fields was increased from 5 to 7 (31% and 10% decreases in the volumes of healthy tissue irradiated to intermediate and high doses, respectively), than from 7 to 9 (11% and 6% decreases, respectively), which itself had a greater effect than an increase from 9 to 11 fields (5 % and 4% decreases, respectively). As for the target-dose inhomogeneities, they were reduced from 25% for the 5-field plan, to 22% for the 7-field plan, to 20% for the 9-field plan and 19% for the 11-field plan. We therefore conclude that a number of fields between 7 and 9 represents a reasonable compromise between the degree of target-dose conformation and target-dose homogeneity achieved, and the ease with which the radiosurgical procedure is planned and delivered.

In this work, no effort was made to optimize the geometry of the radiation beams; the static conformal fields were placed along the dynamic trajectory so that a direct comparison could be made with the dynamic radiosurgery technique. In clinical situations, however, one should take advantage of the flexibility this technique allows with regards to the position of the beams. Thus, the directions of the different beams may be modified in order to optimize the resulting isodose distributions, or to avoid critical or sensitive structures within the brain.

Another advantage of the static conformal fields technique is that it is a relatively simple procedure to perform. The target is irradiated using a single isocenter, which is set once before the beginning of the treatment. The static

fields are then used, in turn, to irradiate the target. There are no couch and gantry movements during irradiation; all machine movements occur between irradiation times, thereby minimizing the probability of complications arising as a result of gantry or treatment couch motor malfunction (and eliminating the probability of collisions between the gantry and the treatment couch).

Stereotactic radiosurgery using fixed, non-coplanar, irregularly shaped beams is a relatively simple technique, which allows for the shaping of the high level isodose surfaces. Successful shaping of the higher level isodose surfaces significantly reduces the amount of healthy brain tissue irradiated to intermediate and high doses, while simultaneously delivering a fairly homogeneous dose to the target volume. The static conformal fields technique, therefore, represents an attractive alternative to the dynamic technique for radiosurgical cases involving irregular targets.

6.2 Future Work

Before this technique can be implemented clinically, a more practical means of performing treatment planning must be found. In this thesis, the *CADPLAN* External Beam Treatment Planning System, appropriately modified to deal with irregularly shaped radiosurgical beams (i.e., using the alternate 10 MV photon beam configuration), was shown to produce accurate results. However, the fact that the patient CT data and the treatment fields had to be scaled by a factor of three prior to using, made the use of *CADPLAN* cumbersome and impractical. Thus, an easier means of performing treatment planning for small irregular fields must be found. Treatment planning for stereotactic radiosurgery at McGill University is done using the McGill Planning System (MPS), developed in-house. Presently, the MPS does not have the capabilities of planning treatment procedures involving small irregular fields, but may be modified to do so in the future. Thus, if this technique is to be used clinically,

perhaps the most simple solution to the problem of treatment planning is to modify the MPS so that it can deal with small irregular fields.

Another aspect to improve upon, prior to using this technique clinically, is the manufacturing of the custom collimators; the method of producing the irregularly shaped radiosurgical beams must be made more accurate and more reproducible. Presently, the greatest source of uncertainty in producing the custom-made collimator inserts stems from the cutting of the styrofoam by the heated wire. The size and shape of the styrofoam cutouts strongly depends upon the heat of the wire and the speed with which the wire cuts through the styrofoam block. Also, this method of making the styrofoam cutouts tends to smooth out any concavities present in the radiosurgical beam. Thus, the accuracy and the reproducibility with which the irregular fields are produced should be improved. This could be achieved by using a computer-controlled micro-multileaf collimator to define the irregularly shaped radiosurgical beams, rather than custom-made collimator inserts.[2] In addition to solving the accuracy and reproducibility problems, the use of a micro-multileaf collimator would greatly reduce the time required to plan and prepare the treatment.

In the future, computer controlled micro-multileaf collimators would also have the advantage of allowing for further development (and possibly subsequent clinical implementation) of dynamic field shaping,[3] in which the shape of the radiation beam continuously changes during the treatment to match the shape of the target. Several challenges must be overcome before dynamic field shaping can be used clinically (e.g., software control of the movements of the leaves, verification of individual radiosurgical procedures, etc.). Nevertheless, a micro-multileaf collimator would allow for a further study of dynamic field shaping (which is considered the ideal conformal radiosurgical technique), and lead to the next level of conformal radiosurgery, three-dimensional conformal radiosurgery, in which not only the fields are shaped to conform to the target volume, but also the beam intensity is modulated to

optimize the dose delivery to the irregular target and spare the critical tissues within the brain.

6.3 References

[1] L.A. Nedzi, H. Kooy, E. Alexander III, R.S. Gelman and J.S. Loeffler, **Variables associated with the development of complications from radiosurgery of intracranial tumors**, Int. J. Radiat. Oncol. Biol. Phys. **21**: 591-599 (1991).

[2] W. Schlegel, O. Pastyr, T. Bortfeld, G. Becker, L. Schad, G. Gademan and W.J. Lorenz, **Computer systems and mechanical tools for stereotacticaly guided conformation therapy with linear accelerators**, Int. J. Radiat. Oncol. Biol. Phys. **24**:781-787 (1992).

[3] D.D. Leavitt, F.A. Gibbs, M.P. Heilbrun, J.H. Moeller and G.A. Takach Jr., **Dynamic field shaping to optimize stereotactic radiosurgery**, Int. J. Radiat. Oncol. Biol. Phys. **21**: 1247-1255 (1991).

List of figures

List of tables

Bibliography

American Association of Physicists in Medicine, **Stereotactic Radiosurgery**, AAPM report no. 54, 1995 2

Ashcroft N.W., **Solid State Physics**, International Ed., Holt, Rinehart & Winston, 1979 49

Attix F.H., **Introduction to Radiological Physics and Radiation Dosimetry**, John Wiley & Sons, New York (1986) 20, 24, 49

Attix F.H., Roesch W.C. and Tochilin E., **Radiation Dosimetry Volume II**, 2nd Ed., Academic Press, New York, 1966 48

Betti O.O. and Derechinsky V.E., **Hyperselective encephalic irradiation with linear accelerators**, Acta Neurochir. Suppl. **33**: 385-390 (1984) 6

Bourland J.D. and McCollough K.P., **Static field conformal stereotactic radiosurgery: physicsl techniques**, Int. J. Radiat. Oncol. Biol. Phys. **28**: 471-479 (1993) 9, 163

Chiu-Tsao S., de la Zerda A., Lin J. and Kim J.H., **High-sensitivity GafChromic film dosimetry for ^{125}I seed**, Med. Phys. **21**: 651-657 (1994)..... 53

Colombo F., Benedetti A., Pozza F., Avanzo R.C., Marchetti C., Chierego C. and Zanardo A., **External stereotactic irradiation by linear accelerator**, Neurosurg. **16**: 154-160 (1985) 6

Dahlin H., Lamm I.L., Landberg T., Levernes S. and Ulso N., **User requirements on CT based computerized dose planning systems in radiotherapy**, Acta Radiol. Oncol. **22**: 398-415 (1983) 86, 101, 105

Fabrikant J.I., Lyman J.T. and Hosobuchi Y., **Stereotactic heavy-ion Bragg peak radiosurgery for intra-cranial vascular disorders: method for treatment of deep arteriovenous malformations**, Brit. J. Radiol. **57**: 479-490 (1984) 3

Flickinger J.C., Lunsford L.D., Wu A., Maitz A.H. and Kalend A.M., **Treatment planning for Gamma knife radiosurgery with multiple isocenters**, Int. J. Radiat. Oncol. Biol. Phys. **18**: 1495-1501 (1990) 7

Flickinger J.C., Maitz A.M.,.Kalend A., Lunsford L.D. and Wu A., **Treatment volume shaping with selective beam blocking using the Leksell Gamma unit**, Int. J. Radiat. Oncol. Biol. Phys. **19**: 783-789 (1990) 8

Frankel K.A., Levy R.P., Fabrikant J.I. and Philips M.H., **Heavy-charged particle radiosurgery: rationale and method**, Stereotactic Radiosurgery, McGraw-Hill, 1993 3

Hall E.J., **Radiobiology for the radiologist**, 3rd Ed., J.B. Lippincott Company, Philadelphia, 1988 3

Hamilton R.J., Kuchnir F.T., Sweeney P., Rubin S.J., Dujovny M., Pelizzari C.A. and Chen G.T.Y., **Comparison of static conformal field with multiple noncoplanar arc techniques for stereotactic radiosurgery or stereotactic radiotherapy**, Int. J. Radiat. Oncol. Biol. Phys. **33**: 1221-1228 (1995) 10

Hartmann G.H., Schlegel W., Sturm V., Kober B., Pastyr O. and Lopez W.J., **Cerebral radiation surgery using moving field irradiation at a linear accelerator facility**, Int. J. Radiat. Oncol. Biol. Phys. **11**: 1185-1192 (1985)...6

International Comission on Radiation Units and Measurements, **Determination of absorbed dose in a patient irradiated by beams of x or gamma rays in radiotherapy procedures**, ICRU Report No. 24 (1976) 33

International Comission on Radiation Units and Measurements, **Radiation quantities and units**, ICRU Report No. 33 (1980) 28, 29

International Comission on Radiation Units and Measurements, **Use of computers in external beam radiotherapy procedures with high-energy photons and electrons**, ICRU Report No. 42 (1983) 86, 101

Johns H.E. and Cunningham J.R., **The Physics of Radiology**, 4th Ed., Thomas Publisher, Springfield IL. (1983) 21, 27, 34

Karzmark C.J., **Advances in linear accelerator design for radiotherapy**, Med. Phys. **11**: 105-128 (1984) 42

Karzmark C.J.and Morton R.J., **A primer on theory and operation of linear accelerators in radiation physics**, Bureau of Radiological Health, FDA 82-8181, Dec. 1981 42

Khan F.M., **The Physics of Radiation Therapy**, 2nd Ed., Williams & Wilkins, Baltimore MD. (1984) 29, 35, 40, 43, 58

Kjellberg R.N., Sintani A., Frantz A.G. and Kliman B., **Proton beam therapy in acromegaly**, N. Engl. J. Med. **278**: 689-695 (1968) 3

Laing R.W., Bentley R.E., Nahum A.E., Warrington A.P. and Brada M., **Stereotactic radiotherapy of irregular targets: a comparison between static conformal beams and non-coplanar arcs**, Radiother. Oncol **28**: 241-246 (1993) 9

Larsson B., Leksell L., Rexed B., Sourander P., Mair W. and Anderson B., **The high energy proton beam as a neurosurgical tool**, Nature **182**:1222-1223 (1958) 2

Larsson B., Liden K. and Sarby B., **Irradiation of small structures through the intact skull**, Acta Radiol. TPB **13**: 513-534 (1974) 4

Lawrence J.H., Tobias C.A., Born J.L., Wang C. and Linfoot J.A., **Heavy-particle irradiation in neoplastic and neurologic disease**, J. Neurosurg. **19**: 717-722 (1962) 3

Leavitt D.D., Gibbs F.A., Heilbrun M.P., Moeller J.H. and Takach Jr. G.A., **Dynamic field shaping to optimize stereotactic radiosurgery**, Int. J. Radiat. Oncol. Biol. Phys. **21**: 1247-1255 (1991) 9, 124

Leksell L., **Cerebral radiosurgery I Gamma thalamotomy in two cases of intractable pain**, Acta Chir. Scan. **134**: 385-395 (1968) 3

Leksell L., **The stereotaxis method and radiosurgery of the brain**, Acta Chir. Scan. **102**: 316-319 (1951) 2

Lutz W., Winston K.R. and Maleki N., **A system for stereotactic radiosurgery with a linear accelerator**, Int. J. Radiat. Oncol. Biol. Phys. **14**: 373-381 (1988) 6

Luxton G. and Jozsef G.J., **Single isocenter treatment planning for homogeneous dose delivery to nonspherical targets in multiarc linear accelerator radiosurgery**, Int. J. Radiat. Oncol. Biol. Phys. **31**: 635-643 (1995) 8

Lyman J.T. and Howard J., **Dosimetry and instrumentation for helium and heavy ions**, Int. J. Radiat. Oncol. Biol. Phys. **3**: 81-86 (1977) 3

Marks L.B.,.Sherouse G.W., Das S., Bentel G.C., Spencer D.P. and Turner D., **Conformal radiation therapy with fixed shaped coplanar or noncoplanar radiation beam bouquets: a possible alternative to radiosurgery**, Int. J. Radiat. Oncol. Biol. Phys. **33**: 1209-1219 (1995) 10

Maryanski M.J., Gore J.C., Kennan R.P. and Schultz R.J., **NMR relaxation enhancement in gels polymerized and cross-linked by ionizing radiation: a new approach to 3D dosimetry by MRI**, Magn. Res. Imag. **11**: 253-258 (1993) 55

Maryanski M.J., Ibbott G.S., Eastman P., Schultz R.J. and Gore J.C., **Radiation therapy dosimetry using magnetic resonance imaging of polymer gels**, Med. Phys. **23**: 699-705 (1996) 55

Maryanski M.J., Schultz R.J., Ibbott G.S., Xie J., Horton D. and Gore J.C., **Magnetic resonance imaging of radiation dose distributions using a polymer-gel dosimeter**, Phys. Med. Biol. **39**: 1437-1455 (1994) 55

McCullough E.C. and Krueger A.M., **Performance evaluation of computerized treatment planning systems for radiotherapy external photon beams**, Int. J. Radiat. Oncol. Biol. Phys. **6**: 1599-1605 (1980)..... 86, 101, 105

McGinley P.H., Butker E.K., Crocker I.R. and Aiken R., **An adjustable collimator for stereotactic radiosurgery**, Phys. Med. Biol. **37**: 413-419 (1992) 9

McGinley P.H., Butker E.K., Crocker I.R. and Landry J.C., **A patient rotator for stereotactic radiosurgery, Phys**. Med. Biol. **35**: 649-657 (1990) 7

McLaughlin W.L., Soares C.G., Sayeg J.A., McCullough E.C., Kline R.W., Wu A. and A.H. Maitz, **The use of radiochromic detector for the determination**

of stereotactic radiosurgery dose characteristics, Med. Phys. **21**: 379-388 (1994) 53

McLaughlin W.L., Yun-Dong C., Soares C.G., Miller A., Van Dyk G.and Lewis D.F., **Sensitometry of the response of a new radiochromic film dosimeter to gamma and electron beams**, Nucl. Instrum. Methods Phys. Res. A **302**: 165-176 (1991) 53

Milan J. and Bentley R.E., **The storage and manipulation of radiation dose data in a small digital computer**, Br. J. Radiol. **47**: 115 (1974)..... 69

Muench P.J., Meigooni A.S., Nath R. and McLaughlin W.L., **Photon energy dependence of the sensitivity of radiochromic film and comparison with silver halide film and LiF TLDs used for brachytherapy dosimetry**, Med. Phys. **18**: 769-775 (1991) 53

Nedzi L.A., Kooy H., Alexander III E., Gelman R.S. and Loeffler J.S., **Variables associated with the development of complications from radiosurgery of intracranial tumors**, Int. J. Radiat. Oncol. Biol. Phys. **21**: 591-599 (1991) 8, 121

Nedzi L.A., Kooy H.M., Alexander E., Svensson G.K. and Loeffler J.S., **Dynamic field shaping for stereotactic radiosurgery: a modeling study**, Int. J. Radiat. Oncol. Biol. Phys. **25**: 859-869 (1993) 9

Orfali A., **Verification of a 3D external photon beam treatment planning system**, Msc. Thesis, McGill University, Montreal (1996) 70

Persico E., Ferrari E. and Segre S.E., **Principles of particle accelerator**, Chap. 8, W.A. Benjamin Inc., New York, 1968 42

Pike B., Podgorsak E.B., Peters T.M. and Pla C., **Dose distributions in dynamic radiosurgery**, Med. Phys. **14**: 780-789 (1987) 69

Pla C., **A Macintosh-based treatment planning system for brachytherapy and radiosurgery**, in A.R. Hounsell, J.M. Wilkinson, P.C. Williams (eds.): Proceedings of the Xith International Conference on the Use of Computers in Radiotherapy, 20-24 March 1994, Manchester, UK, pp. 138-139 69

Plazas M.C., Lefkopoulos D. and Schlienger M., **The influence of arc weights on the dose distribution for single target radiosurgery**, Med. Phys. **20**: 1485-1490 (1993) 8

Podgorsak E.B., Olivier A., Pla M., Hazel J., de Lotbiniere A. and Pike B., **Physical aspects of dynamic stereotactic radiosurgery**, Appl. Neurophysiol. **50**: 263-268 (1987) 6

Podgorsak E.B., Olivier A., Pla M., Lefebvre P.Y. and Hazel J., **Dynamic stereotactic radiosurgery**, Int. J. Radiat. Oncol. Biol. Phys. **14**: 115-126 (1988) 6

Ramani R., Lightstone A.W., Mason D.L.D. and O'Brien P.F., **The use of radiochromic film in treatment verification of dynamic stereotactic radiosurgery**, Med. Phys. **21**: 389-392 (1994) 53

Ramani R., O'Brien P.F., Davey P., Schwartz M.L., Young C.S., Lightstone A.W. and Mason D.L.D., **Implementation of multiple isocentre treatment for dynamic radiosurgery**, Brit. J. Radiol. **68**: 731-735 (1995) 7

Sayeg J.A. and Gregory R.C., **A new method for characterizing beta-ray ophtalmic applicator sources**, Med. Phys. **18**: 453-461 (1991) 53

Scanditronix AB, **RFA 300 radiation field analyzer**, operation manual (Scanditronix AB, Uppsala, Sweden, 1992) 59

Schlegel W., Pastyr O., Bortfeld T., Becker G., Schad L., Gademann G. and Lorenz W.J. , **Computer systems and mechanical tools for stereotactically guided conformation therapy with linear accelerators**, Int. J. Radiat. Oncol. Biol. Phys. **24**: 781-787 (1992) 9, 124

Serago C., Lewin A., Houdek P., Abitol A., Gonzales-Arias S., Pisciotti V. and Schwade J., **Improved linac dose distributions for radiosurgery with irregularly shaped fields** (Abstr.), Int. J. Radiat. Oncol. Biol. Phys. **19**: 134 (1990) 9

Serago C.F., Lewin A.A., Houdek P.V., Gonzalez-Arias S., Abitbol A.A., Marcial-Vega V.A., Pisciotti V. and Schwade J.G., **Improved linac dose distributions for radiosurgery with elliptically shaped fields**, Int. J. Radiat. Oncol. Biol. Phys. **21**: 1321-1325 (1991) 9

Sixel K.E., Podgorsak E.B. and Souhami L., **Cylindrical dose distributions in pseudodynamic rotation radiosurgery: an experimental study**, Med. Phys. **20**: 163-170 (1993) 9

Ter-Pogossian M.M., **The physical basis of diagnostic radiology**, Harper & Row, New York, 1967 51

Van Dyk J., Barnett R.B., Cygler J.E. and Shragge P.C., **Commissioning and quality assurance of treatment planning computers**, Int. J. Radiat. Oncol. Biol. Phys. **18**: 261-273 (1993) 86, 87, 101, 105

Varian Oncology Systems, **CADPLAN 2.7 External Beam Modeling: Reference Manual**, Version 1.0, Varian-Dosetek Oy, Finland (1996) 70

Walton L., Bomford C.K. and Ramsden D., **The Sheffield stereotactic radiosurgery unit: physical characteristics and principles of operation**, Brit. J. Radiol. **60**: 897-906 (1987) 3

Wu A., Lindner G., Maitz A.H., Kalend A.M., Lunsford L.D., Flickinger J.C. and Bloomer W.D., **Physics of Gamma knife approach on convergent beams in stereotactic radiosurgery**, Int. J. Radiat. Oncol. Biol. Phys. **18**: 941-949 (1990) 3

Young M.E.J., **Radiological Physics**, 3rd Ed., London H.K. Lewis & Co. Ltd., London, 1983 48

Zankowski C., **Monte Carlo analysis of the 10 MV X-ray beam from a Clinac-18 linear accelerator**, Msc. Thesis, McGill University, Montreal (1994)..... 44, 45

IMAGE EVALUATION
TEST TARGET (QA-3)

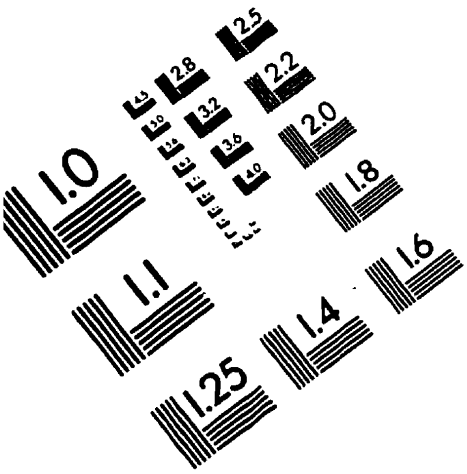

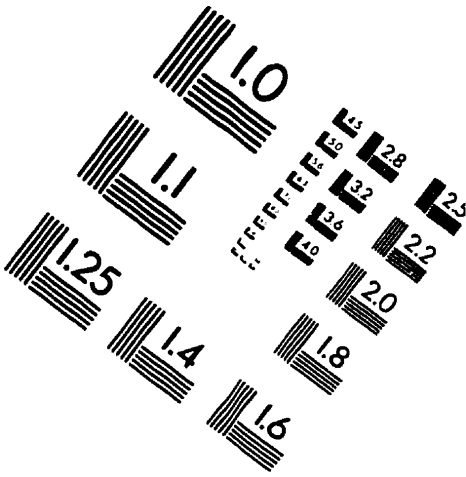

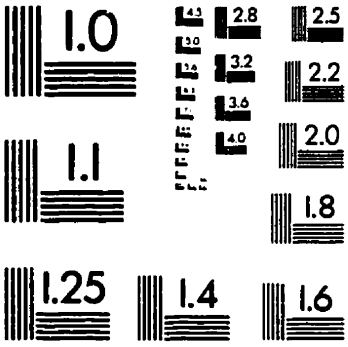

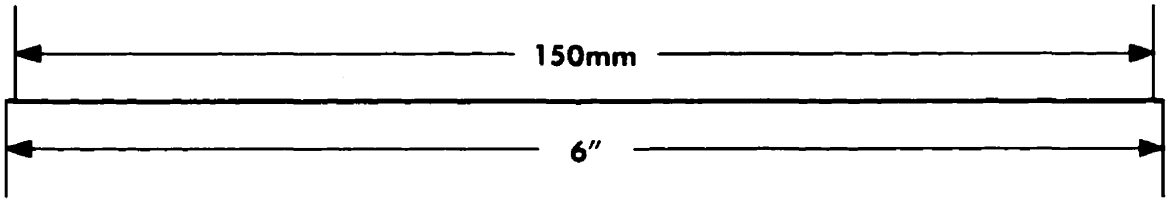

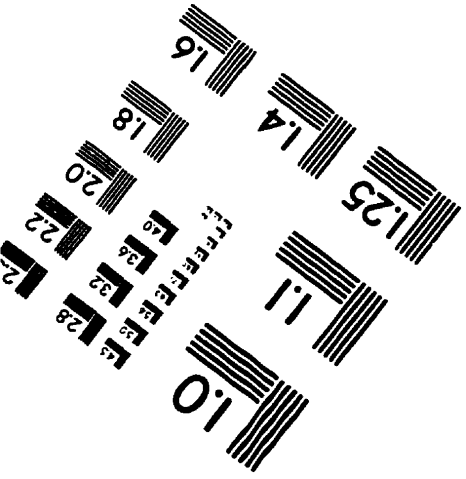

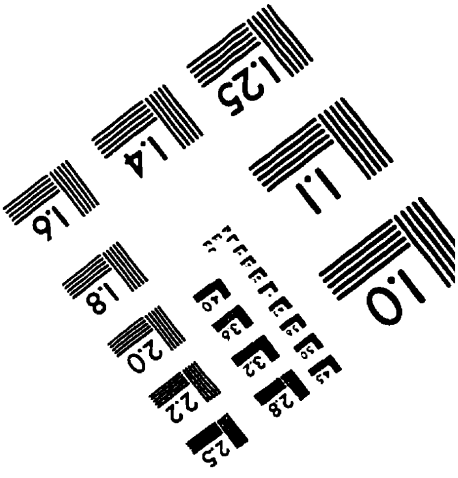

APPLIED IMAGE, Inc
1653 East Main Street
Rochester, NY 14609 USA
Phone: 716/482-0300
Fax: 716/288-5989